ROCK PHYSICS AND 3-D SEISMIC CHARACTERIZATION OF RESERVOIR HETEROGENEITIES TO IMPROVE RECOVERY EFFICIENCY

A DISSERTATION
SUBMITTED TO THE DEPARTMENT OF GEOPHYSICS
AND THE COMMITTEE ON GRADUATE STUDIES
OF STANFORD UNIVERSITY
IN PARTIAL FULFILLMENT OF THE REQUIREMENTS
FOR THE DEGREE OF DOCTOR OF PHILOSOPHY

Mario Augusto Gutiérrez

April 2001

I certify that I have read this dissertation and that in my opinion it is fully adequate, in scope and quality, as a dissertation for the degree of Doctor of Philosophy.

_____

(Principal Advisor)

I certify that I have read this dissertation and that in my opinion it is fully adequate, in scope and quality, as a dissertation for the degree of Doctor of Philosophy.

_____

I certify that I have read this dissertation and that in my opinion it is fully adequate, in scope and quality, as a dissertation for the degree of Doctor of Philosophy.

_____

I certify that I have read this dissertation and that in my opinion it is fully adequate, in scope and quality, as a dissertation for the degree of Doctor of Philosophy.

_____

Approved for the University Committee
on Graduate Studies:

_____

Abstract

Geological heterogeneities prevent efficient drainage and sweep of hydrocarbons, causing low recovery efficiency in many oil and gas fields around the world. The extraction of remaining oil is based on the identification of the reservoir heterogeneities and the volumes of mobile oil in unswept zones that can be economically produced by infill wells, side-tracks, and recompletions. The most efficient way of obtaining a 3-D description of these subsurface heterogeneities, that control the spatial distribution and recovery of mobile oil, is through seismic surveys.

In this thesis, I provide a rock physics and seismic characterization of structural, depositional and diagenetical reservoir heterogeneities, from the pore to the field scale, of Tertiary fluvial sandstones in the mature giant La Cira-Infantas oil field. I introduce various applications of theoretical rock physics and geological interpretation of 3-D seismic data to improve recovery factor in oil and gas fields. The approach is presented in three parts: (1) Description and analysis of structural heterogeneities, (2) study of heterogeneities associated with depositional and diagenetical processes, and (3) analysis of pore-fluid effect on elastic properties.

In the first part, I present a rigorous model of faulting, folding, and slip distribution for the La Cira-Infantas oil field. This field is characterized by a series of structural heterogeneities associated with early and late Tertiary tectonic events. An intensely folded, faulted, and eroded Cretaceous sequence underlies the Tertiary cover below the Middle Eocene unconformity. The west flank of a large antiform, elongated in north-south direction, is highly fractured by thrust faults that generate a series of asymmetric secondary folds. Late Tertiary structural heterogeneities are comprised of La Cira and Infantas anticlines and two groups of associated faults. The first group includes a set of low-angle reverse faults with east- and west-vergence. They usually cut the entire Tertiary sequence and glide on a shaly section directly above the Eocene unconformity. These faults commonly strike from north-south to $N30°E$. Moreover, there are a number of important normal faults, which compartmentalize the La Cira and Infantas anticlines into a set of reservoir blocks. Two different patterns of normal faults were identified in

plan view: longitudinal and oblique. The description of the dip slip along various seismic markers suggests that normal faults in the northern La Cira area, formerly interpreted as continuous fault planes, consist of several overstepping segments.

A simple parallel and small-displacement wrench zone, poorly developed during the Miocene to Pliocene, explains the folding, thrusting, and normal faulting of the Tertiary deposits in the La Cira-Infantas structure. The new model of structural heterogeneities provides a clear delineation of the field production boundaries and compartments, and a structural configuration concordant with the tectonic history of the basin.

The second part describes a rock physics model for relating the elastic reservoir properties to porosity, mineralogy, pore fluid, and differential pressure. Here I found that if subsets of log and core data are used that are constrained by a sequence stratigraphy framework, meaningful rock physics relations can be determined. These relations can be rationalized and explained by effective-medium models. By analyzing well logs and core data, a governing rock physics model was determined. The model implies that velocity and acoustic impedance are reliable reservoir quality discriminators. Specifically, high velocity and impedance correspond to shales while low velocity and acoustic impedance indicate high-quality sands. I applied this concept to map highly heterogeneous reservoir properties in Tertiary fluvial sandstones in the mature giant La Cira Infantas oil field.

Finally, in the third part of this dissertation I present a rock physics model for identifying the quality of rock and pore fluid in a cased hole from dipole sonic data, as well as for monitoring temporal changes in the reservoir from repeated compressional wave data in the well. By analyzing the Vp/Vs ratio from multi-pole velocity logs, it is possible to differentiate between nonhydrocarbon- and hydrocarbon-bearing sands. The Vp/Vs ratio, as calculated from multi-pole sonic logs, is a promising indicator for delineating bypassed oil behind the casing and pay intervals. The same rock physics approach should be valid for identifying hydrocarbons in La Cira-Infantas and other fields with similar geologic setting from surface seismic if pre-stack or offset-stack data are available. The model predictions are also consistent with time-lapse sonic log data where the P-wave velocity shows a drop in the intervals open for production. This effect is most likely associated with free gas coming out of solution. It can also be used for reservoir depletion monitoring.

Acknowledgements

I would like to thank all professors, staff members, and students in the Earth Sciences School who made my stay at Stanford a most exceptional and pleasant experience. I wish to express my sincere appreciation to my advisor Professor Amos Nur, for his inspiring advice, economical support, and encouragement in the research of this dissertation. I also thank Henrique Tono who introduced me to Amos.

I feel honored to have worked and interacted with all members of my thesis committee. I am so grateful to Jack Dvorkin for his advice, friendship, and experience. I would like to thank Steve Graham for his excellent teaching, both in and out the classroom. Many ideas of my dissertation occurred to me from his courses and superb field trips. This work also has benefited greatly from Gary Makvo's outstanding teaching and constructive comments.

Over my four and an one-half years at Stanford, it has been a great privilege to be part of the Stanford Rockphysics Project (SRB) research group. I really wish to thank former and current student and staff of SRB for the motivating research atmosphere and camaraderie. Discussions with Tapan Mukerji, Manika Prassad, Madhumita Sengupta, Dan Moos, and structural geology Professors Atilla Aydin and Dave Pollard were very useful. I would like to thank Margaret Muir for her kindness and support.

My special thanks go to my wife and colleague Elizabeth and my children Mario Andres and Sara Marcela for their unstinting support. This doctorate owes much to Elizabeth's companionship, perseverance, and love over the years. Many thanks also to my parents Mario and Rosa Isabel. I was blessed to grow up in a family of educators. Many thanks to my sisters Marcela and Adriana, and my brothers Javier and Alejandro for their moral support and invaluable assistance.

The Stanford Rockphysics and Borehole Geophysics Project (SRB) and Ecopetrol support this work. Finally, I would like to thank Ecopetrol for providing the data and for supporting me financially during my Master of Science at Stanford.

Contents

List of Figures

Chapter 1

Introduction

1.1 Definition of the Problem

Recovery of oil from reservoirs using 1990's technology has averaged in the USA only 35%. For reservoirs outside the USA, statistics show a much lower percentage of recovery (Tyler and Finley, 1991; Weber, 1999). This is due to poor sweep efficiency in heterogeneous reservoirs. Reservoir heterogeneities are one of the principal causes for very low recovery efficiency in numerous gas and oil fields around the world.

Structural, depositional, and diagenetic heterogeneities compartmentalize reservoirs into flow units of variable lateral and horizontal extent. Reservoir heterogeneities controlling fluid flow vary from large scale faults and genetic unit boundaries to thin shale intercalations, sedimentary structures, and pore scale features (Weber, 1986). Generally, these heterogeneities prevent efficient drainage and sweep of reservoirs and are frequently bound up with the facies architecture inherited from the original depositional system.

1.2 Reservoir Heterogeneities and Recovery Efficiency

Reservoir rocks deposited in different sedimentary environments exhibit dissimilar architectures, which are defined by the facies dimensions, orientations, and vertical and lateral relationships. Facies, or mixed groups of facies, are the essential building blocks of reservoirs, and constitute the fundamental *flow units* (Hearns et al., 1984; Ebanks, 1987, Ebanks, 1993) through which the reservoir drains. Interconnectedness with adjacent facies promotes effective reservoir drainage, whereas interconnectedness can be inhibited due to differences in permeability and results in reservoir compartmentalization

and ultimately in inefficient reservoir drainage or low recovery efficiency (Tyler and Finley, 1991).

Lake (1989) defines *recovery efficiency* E_{Ri} of the component i as

$$E_{Ri} = E_{Di} E_{Vi}, \tag{1.1}$$

where E_{Di} is the displacement efficiency and E_{Vi} is the volumetric sweep efficiency,

$$E_{Di} = \text{Amount of } i \text{ displaced / Amount of } i \text{ contacted, and} \tag{1.2}$$

$$E_{Vi} = \text{Amount of } i \text{ contacted / Amount of } i \text{ in place.} \tag{1.3}$$

E_{Di} is a function of time and fluid viscosities, relative permeabilies, and capillary pressures, and E_{Vi} is a function of time, viscosities, well arrangements, heterogeneity, gravity, and capillary forces. Laudon (1996) summarizes the intrinsic factors as reservoir quality (porosity, permeability, lateral and vertical continuity), drive mechanism and type of fluid recovered (gas, oil, tar), and such external factors as well spacing, production time and rates, and secondary and tertiary recovery techniques.

Among the intrinsic factors that affect the recovery efficiency, are rock properties. These include the porosity, permeability, and lithology of sediment bodies comprising a reservoir, and reflect heterogeneities produced by different stacking arrangements of sediment bodies or reservoir architecture. These properties strongly depend on the facies that comprise a depositional system and their preservation (Gardner et al, 1995).

Although recovery efficiency from oil and gas reservoirs is governed by several factors, reservoir heterogeneities play a very important role in this process. Tyler and Finley (1991) found a clear relationship between reservoir architecture and conventional recovery efficiency. They determined that in a diversity of depositional environments, the fundamental factor that controls recovery efficiency is reservoir genesis, which is based on depositional processes and diagenetic history.

1.3 Remaining Oil in Mature Fields

Fisher (1987) published statistics for the oil produced and left in mature oil fields in the USA, and classified the remaining oil into inmobile oil (46.9%), remaining conventional reserves (5.7%), and unswept zones (16.4%). Actually, the mobile oil can

be a bigger part of the remaining oil. In the late 1980's, Shell Oil Company found that in many fields the unswept oil averages 25% in clastic rocks, and often up to 40% in carbonate, light oil reservoirs (Weber, 1999).

Tyler and Finley (1991) consider mobile oil recovery efficiency as a more sensitive indicator of the influence of reservoir heterogeneity. They define the unrecovered mobile oil (UMO) as the oil that remains in the reservoir after primary and secondary recovery but is movable by primary recovery or water flooding. The essential reason for the intrareservoir entrapment of UMO is that reservoir heterogeneities exert a fundamental restriction on the way in which fluids move through the reservoir rock. As a result, geologic heterogeneities, including faults, genetic unit boundaries and baffles, permeability zonations within genetic boundaries, and microscopic texture and mineralogy, do not allow uncontacted and bypassed hydrocarbons to migrate to the well bore. Therefore, the location and volumetric estimation of bypassed and uncontacted hydrocarbon compartments demand precise geologic characterization and modeling of reservoir heterogeneities.

1.4 La Cira-Infantas Oil Field

The problem of recovery efficiency in heterogeneous reservoirs, particularly in ancient fluvial oil deposits, is of general significance because it has considerable economic importance worldwide. Much of the oil in the giant fields at Prudhoe Bay (Alaska), Statfjord (North Sea), Brent (North Sea), Daqing (China), and La Cira-Infantas (Colombia) is found in fluvial reservoirs (Miall, 1996; Dickey, 1992). This study focuses on the La Cira-Infantas field.

La Cira-Infantas is located in the Middle Magdalena Basin, near the center of Colombia, 250 km north of Bogota. The estimated oil originally in place was 3700 million barrels (MMBO). After 80 years of exploitation and drilling of 1742 wells, the cumulative production has reached only 720 MMBO. The low recovery factor (19%) is related to the high heterogeneity of the reservoirs.

1.5 3-D Seismology and Rock Physics

The main challenge for hydrocarbon geoscientists now and in the future is to considerably improve hydrocarbon recovery efficiency from recently and formerly discovered reservoirs. A fundamental task linked to accomplishing this aim is to assemble detailed 3-D descriptions of reservoir heterogeneities. The extraction of remaining oil is based on the identification of volumes of mobile oil in unswept zones that can be economically produced by infill wells, side-tracks, and recompletions. In these particular circumstances, the most relevant reservoir heterogeneities are faults, boundaries of genetic units, large permeability contrast, and baffles to flow such shale intercalations (Weber, 1986). The most efficient way of obtaining a 3-D description of these subsurface heterogeneities is through seismic surveys.

Conventional geophysical reservoir characterization focuses on obtaining the geological meaning of seismic amplitude and its mathematical attributes. Geostatistics is frequently applied to correlate such non-physical attributes to reservoir physical properties. However, these techniques are often not able to provide precise reservoir property descriptions because they do not take advantage of deterministic physical links between seismic and reservoir properties. 3-D seismic data, in principle, can be converted into a volume of the reservoir's elastic properties such as acoustic and elastic impedance. The challenge remains to relate these elastic properties to porosity, lithology, and hydrocarbon saturation. Rock physics provides this connection.

To date, there has been little work on developing specific techniques for reservoir characterization in fluvial sedimentary settings, based on rock physics analysis and 3-D seismology. Moreover, much of the work done in seismic stratigraphy, predominantly in marine sedimentary environments, has put emphasis on the use of 2-D seismic data.

In order to obtain consistent descriptions of reservoir heterogeneities and relationships among type of deposits, flow units, rock properties, and petrophysical properties, a rock physics and seismic characterization of reservoir heterogeneities is carried out in this thesis. Combining core and well-log rock physics analysis and the geological interpretation of 3-D seismic data, I studied the geological heterogeneities, from the pore to the field scale, of Tertiary fluvial sandstones in the mature giant La Cira-

Infantas oil field. The final goal of this study is to present an integrated approach for seismically mapping reservoir heterogeneities, spatial distributions of petrophysical properties, and flow units.

1.6 Description of Chapters

The rock physics and 3-D seismic characterization of reservoirs heterogeneities to improve recovery efficiency is divided in three phases: (1) description and analysis of structural heterogeneities, (2) study of heterogeneities associated with depositional and diagenetical processes, and (3) analysis of pore-fluid effect on elastic properties. The chapters in this thesis present various applications of theoretical rock-physics and geological interpretation of 3-D seismic data to improve the recovery factor in oil and gas fields.

In Chapter 2, I present a rigorous model of faulting, folding, and slip distribution for the La Cira-Infantas oil field. A very thorough and detailed description and documentation of the structural features, based on the interpretation of a specially acquired three-dimensional seismic data set, support the model.

Chapter 3 explores the relationships between sedimentary geology and rock physics. Here I initially describe a rock physics model for relating the elastic reservoir properties to porosity, mineralogy, pore fluid, and differential pressure, with the stratigraphic framework used as a constraint to select the relevant data subsets. Later, I define a methodology for seismic mapping of the internal architecture of Tertiary fluvial sandstone reservoirs and the spatial distributions of petrophysical properties and their flow units, that combines core and well-log rock physics analysis with the stratigraphic interpretation of 3-D surface seismic.

Finally, Chapter 4 presents a rock physics model and its application for identifying the reservoir quality and pore fluid in a cased hole from dipole sonic data, as well as for monitoring temporal changes in the La Cira-Infantas reservoirs from repeated compressional wave data in the well.

1.7 References

Dickey, P., 1992, La Cira-Infantas Field, Middle Magdalena Basin, in E. A. Beaumont and N. H. Foster, Eds., Structural Traps VII, AAPG Treatise of Petroleum Geology, Atlas for Oil and Gas Field, p. 323-347.

Ebanks, W. J. Jr., 1987, Flow unit concept-integrated approach to reservoir descriptions for engineering projects: AAPG Bulletin, **71,** no. 5, p. 551-552.

Ebanks, W. J. Jr., M. H. Scheihing, and C. D. Atkinson, 1993, Flow units for reservoir characterization, in D. Morton-Thompson and A. M. Woods, Eds., Development Geology Reference Manual, AAPG Methods in Exploration Series, no. 10, p. 282-285.

Fisher, E. W., 1987, Can the U. S. oil and gas resource base support sustained production?: Science, **236,** p. 1631-1636.

Gardner, M. H., B. J. Willis, and I. N. W. Dharmasamadhi, 1995, Outcrop-based reservoir characterization of low accommodation/sediment supply fluvial-deltaic sandbodies, in Reservoir characterization: Integration of geology, geophysics and reservoir engineering, The third JNOC-TRC international symposium, p. 17-54.

Hearns, C. L., W. J. Ebanks, Jr., R. S. Tye, and V. Ranganathan, 1984, Geological factors influencing reservoir performance of the Hartzog Draw field: Journal of Petroleum Technology, **36**, p. 1335-1344.

Lake, L. W., 1989, Enhanced oil recovery: Englewood Cliff, New Jersey, Prentice-Hall Inc., 550 p.

Laudon, R. C., 1996, Principles of petroleum development geology: Upper Saddle River, New Jersey, Prentice-Hall Inc., 267 p.

Miall, A. D., 1996, The geology of fluvial deposits: Sedimentary facies, basin analysis and petroleum geology: Berlin Heidelber New York, Springer-Verlag, 582 p.

Tyler, N. and R. J. Finley, 1991, Architectural controls on the recovery of hydrocarbons from sandstone reservoirs, in A. D. Miall and N. Tyler, Eds., The three-dimensional facies architecture of terrigenous clastic sediments and its implications for hydrocarbon discovery and recovery: SEPM, Concepts in sedimentology and paleontology, **3,** p. 1-5.

Weber J. W., 1986, How heterogeneity affects oil recovery: in L. W. Lake and H. B. Carrol Jr., Eds, Reservoir Characterization, Academic Press Inc., Orlando, Florida, p. 487-544.

Weber J. W., 1999, The prize-what's possible: Petroleum Geoscience, **5,** p. 135-144.

Chapter 2

3-D Seismic Interpretation of Structural Heterogeneities in the Mature Giant Field La Cira-Infantas, Middle Magdalena Valley Basin

2.1 Abstract

The La Cira-Infantas oil field, located in the Middle Magdalena Valley Basin, Colombia, is characterized by a series of structural heterogeneities associated with early and late Tertiary tectonic events. An intensely folded, faulted, and eroded Cretaceous sequence underlies the Tertiary cover below the Middle Eocene unconformity. The west flank of a large antiform, elongated in north-south direction, is highly fractured by thrust faults that generate a series of asymmetric secondary folds.

Late Tertiary structural heterogeneities are comprised of La Cira and Infantas anticlines and two groups of associated faults. The first group includes a set of low-angle reverse faults with east- and west-vergence. They usually cut the entire Tertiary sequence and glide on a shaly section directly above the Eocene unconformity. These faults commonly strike from north-south to $N30°E$. Moreover, there are a number of important normal faults, which compartmentalize the La Cira and Infantas anticlines into a set of reservoir blocks. Two different patterns of normal faults were identified in plan view: longitudinal and oblique.

The structural interpretation of 3-D seismic data, based on a set of closely spaced measurements of the fault slip, allows an accurate mapping and analysis of the slip distribution. The displacement discontinuity, or slip, is a fundamental physical quantity than can be used to study faults whose characterization provides a better understanding of

the faulting mechanics and the important factors that control hydrocarbon distribution within an oil field structure. The description of the dip slip along various seismic markers suggests that normal faults in the northern La Cira area, formerly interpreted as continuous fault planes, consist of several overstepping segments.

Because the fault plane segments are roughly elliptical in shape, the slip changes more rapidly along the dip direction than along the strike. The irregular slip distribution along the main fault surfaces may affect the hydraulic behavior of the faults, creating fluid flow anomalies and the resulting production problems in the La Cira-Infantas oil field. Therefore, integrating the slip analysis into the reservoir studies is vital to effectively characterize flow paths, fault sealing potential, and reservoir compartmentalization.

A simple parallel and small-displacement wrench zone, poorly developed during the Miocene to Pliocene, explains the folding, thrusting, and normal faulting of the Tertiary deposits in the La Cira-Infantas structure. The new model of structural heterogeneities provides a clear delineation of the field production boundaries and compartments, and a structural configuration concordant with the tectonic history of the basin.

2.2 Introduction

2.2.1 Research Motivation

One of the current problems in oil recovery is the restricted knowledge of the reservoir's external geometry and the controls that geological heterogeneities exert on hydrocarbon flow. Generally, geological heterogeneities compartmentalize reservoirs into flow units, preventing efficient drainage and sweep of reservoirs.

Understanding the three-dimensional geometry, spatial organization, genesis, and evolution of structures such as folds and faults is essential to providing a realistic conceptual model for flow studies. However, to date wireline log-based structural models of several mature giant oil fields, including La Cira-Infantas, do not provide a clear delineation of the field production boundaries and compartments. Moreover, particularly in La Cira-Infantas, the characteristics and evolution of its structural style are incompletely understood. Published interpretations show La Cira-Infantas structure,

which is a complex combination of probably coeval folds, thrust faults, and a large number of normal faults, as the farthest west expression of a thrust belt that extends out into the Middle Magdalena Valley Basin from the Eastern Cordillera. These structural elements are not consistent with the characteristics of a typical compressive tectonic regime, as is generally claimed in the literature (Mojica and Franco, 1990; Dickey, 1992; Restrepo-Pace et al., 1999a).

In order to solve these uncertainties, I present in this chapter a rigorous model of faulting for the La Cira-Infantas oil field. A very thorough and detailed description and documentation of the structural features, based on the interpretation of a specially acquired three-dimensional seismic data set, support the model.

2.2.2 Location of the Study Area

The Magdalena Valley Basins are a set of intermontane sags, located along the Magdalena River valley between the Central and Eastern Andean Cordilleras in Colombia. Geographically and geologically, the north-draining Magdalena River valley is divided into three regions: Upper, Middle, and Lower (Figure 2.1).

The La Cira-Infantas oil field is located in the central sag: the Middle Magdalena Valley Basin (MMVB). This basin is an elongated depression with a total area of approximately 30,000 km^2. It is 500 km in length from south to north and 60 km in average width. Historically, the MMVB is one of the most prolific petroleum basins of Colombia. The initial commercial exploitation was set up in the La Cira-Infantas Field in 1918. The current production of MMVB is circa 5% of the total oil in Colombia.

2.2.3 Regional Setting

The mountains and sedimentary basins of Central Colombia are located along the Andes, the principal structural uplift in South America. The Andean range in northern South America has a complex geological history associated with its particular location at the junction of the Caribbean, Central, and South American tectonic regions. The Andean system of Colombia is composed of two geological systems: The Eastern Cordillera and

Central Cordillera with sialic basement, and the western margin of the Central Cordillera, the Western Cordillera, and Serrania del Baudo, with simatic basement (Figure 2.1).

Etayo (1985) proposed the development of an aulacogen basin during the Triassic to Early Cretaceous period. The aulacogen model is workable, because the geologic record shows that the Triassic to early Cretaceous rift never proceeded through the stages of continental separation. Cretaceous passive margin conditions and several interior rift basins were developed in northern South America during the continental separation between Yucatan and Northern South America (Villamil, 1998a).

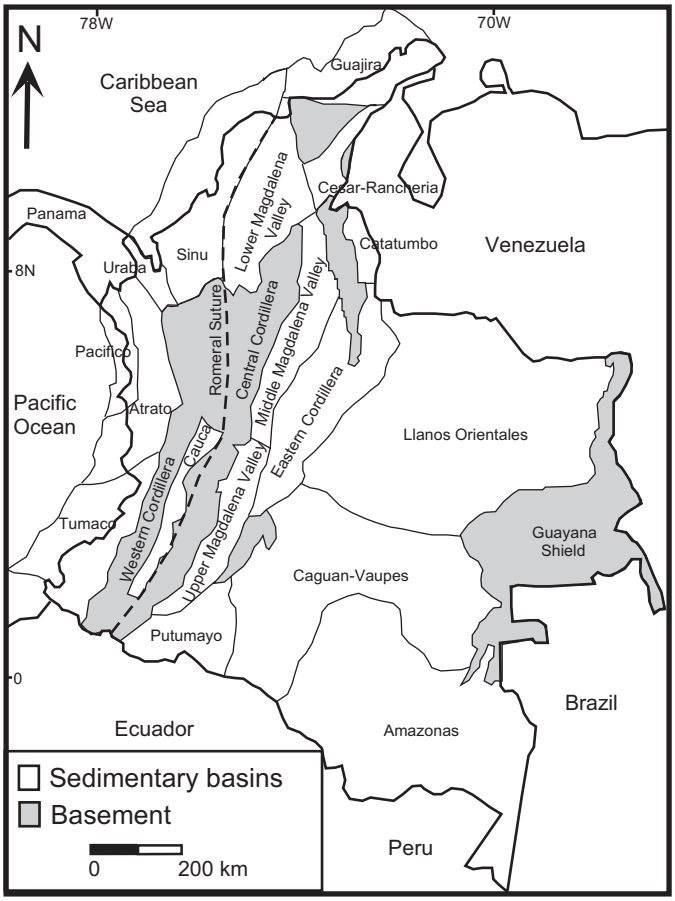

Figure 2.1: Sedimentary basins map of Colombia. After Ecopetrol (2000).

Associated with this separation, the accretion of simatic crustal material took place in the western flank of the Central Cordillera. From this time onward, simatic basement in Colombia developed in belts, which are younger to the west, from the western margin of the Central Cordillera (Etayo, 1985). A second collision and accretion of the Western

Cordillera occurred at the end of the Cretaceous. Mesozoic aulacogen and passive margin basins were inverted during Tertiary Andean orogenesis, generating foreland intermontane basins.

Tectonics and Structural Geology

The Middle Magdalena Valley Basin (MMVB) is an asymmetric sedimentary basin characterized by a complex geological evolution (Figure 2.2). Its geological evolution is comprised of a series of distinct stages of tectonic development: the MMVB evolved as an aulocogen basin in the Triassic to Jurassic, a passive margin basin in the Cretaceous to Paleocene, and a foreland basin with east-vergence during the Eocene to Oligocene. Since the Miocene, it has been an intermontane basin.

The faults and folds in the MMVB show a predominant NNE-SSW orientation, and their origin is associated with the tectonic evolution of the features that bound the basin regionally, namely the Central and Eastern Cordillera. These ranges are mostly characterized by east- or west-vergent thrusting and transpression along the principal strike-slip fault zones of Palestina (Suarez, 1997) and Santa Marta-Bucaramanga (Montgomery, 1992) (Figure 2.2).

Three distinct structural areas characterize the northern MMVB. The western margin consists of high-angle reverse faults, the eastern margin is comprised of a zone of thrusts faults, and the central area shows the least structural complexity in the basin (Figure 2.2; Suarez, 1997; Restrepo-Pace et al, 1999a).

Stratigraphic Summary

The oldest rocks exposed in the Eastern and Central Cordillera are upper Proterozoic polymetamorphosed gneiss, amphibolite, metasedimentary rocks, and Cambrian-Ordovician or Devonian metasedimentary rocks (Etayo et al., 1983). These rocks represent crystalline basement of the Middle Magdalena Valley Basin. Resting on these cratonic margin rocks is a series of Jurassic continental sediments that underlie calcareous and siliciclastic Cretaceous rocks of marine to transitional origin and Tertiary fluvial deposits (Figure 2.3).

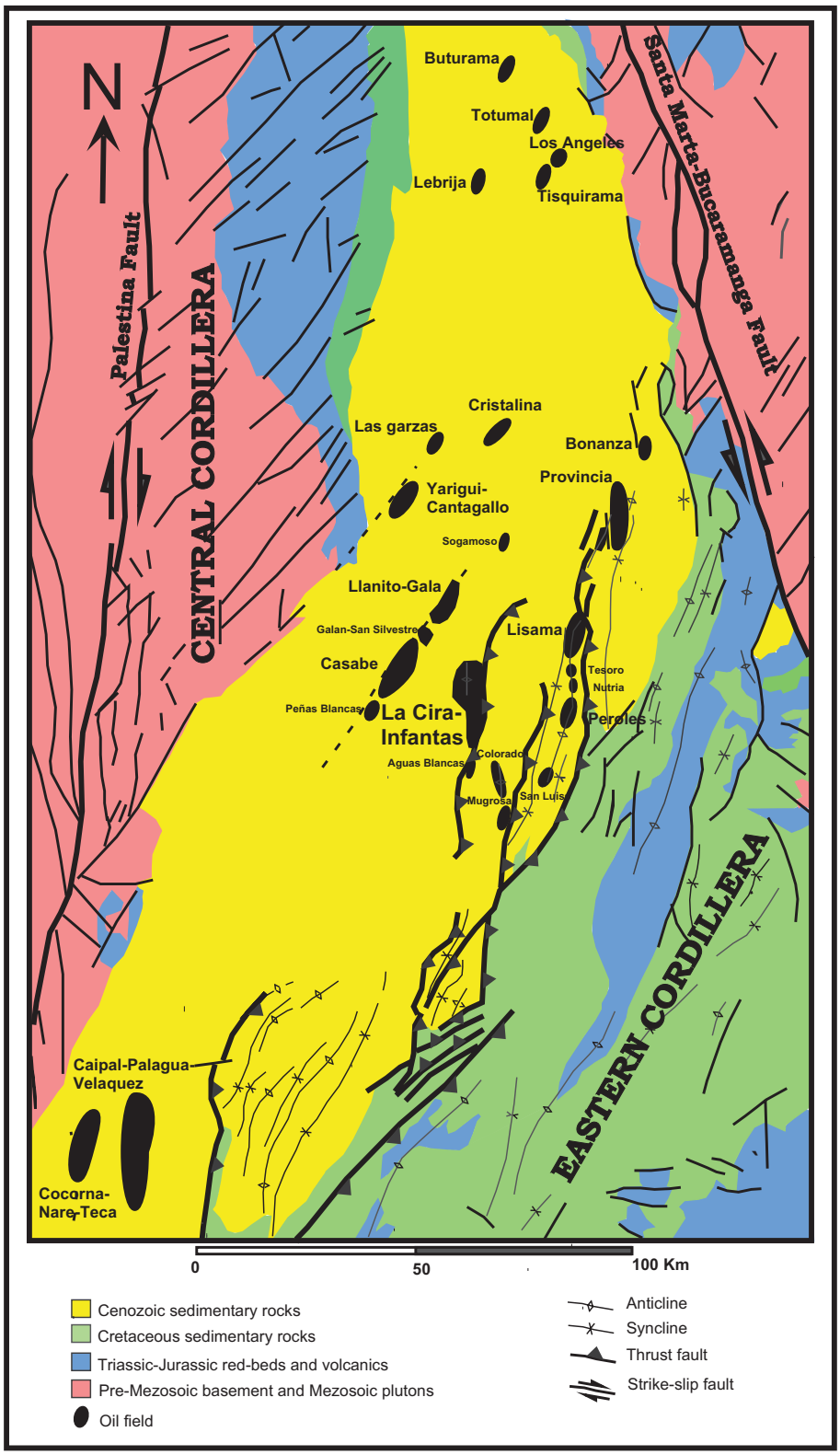

Figure 2.2: Geological map and producing oil fields of the Middle Magdalena Valley Basin. After Geotec (1988), Ingeominas (1976), and Ecopetrol (2000).

The Jurassic Giron Group, a heterogeneous succession of continental red beds and silicic to intermediate volcanics, is the oldest sedimentary unit in the MMVB and lies unconformably on the crystalline basement (Etayo et al., 1983). These rocks filled the Jurassic rift that developed in the current position of the MMVB and the Eastern Cordillera (Pindell, 1985; Villamil, 1998b). Cretaceous strata of Colombia were deposited over an evolving continental margin and show a steady accumulation typical of thermal subsidence (Villamil, 1998a). The sandy Tambor Formation indicates the beginning of the Cretaceous deposition during the Valanginian in MMVB. These strata rest unconformably on Jurassic red beds and were deposited in a continental to transitional environment (Morales et al., 1958). The underlying calcareous Rosablanca Formation was deposited in marine conditions during the Hauterivian-Barremian (Morales et al., 1958).

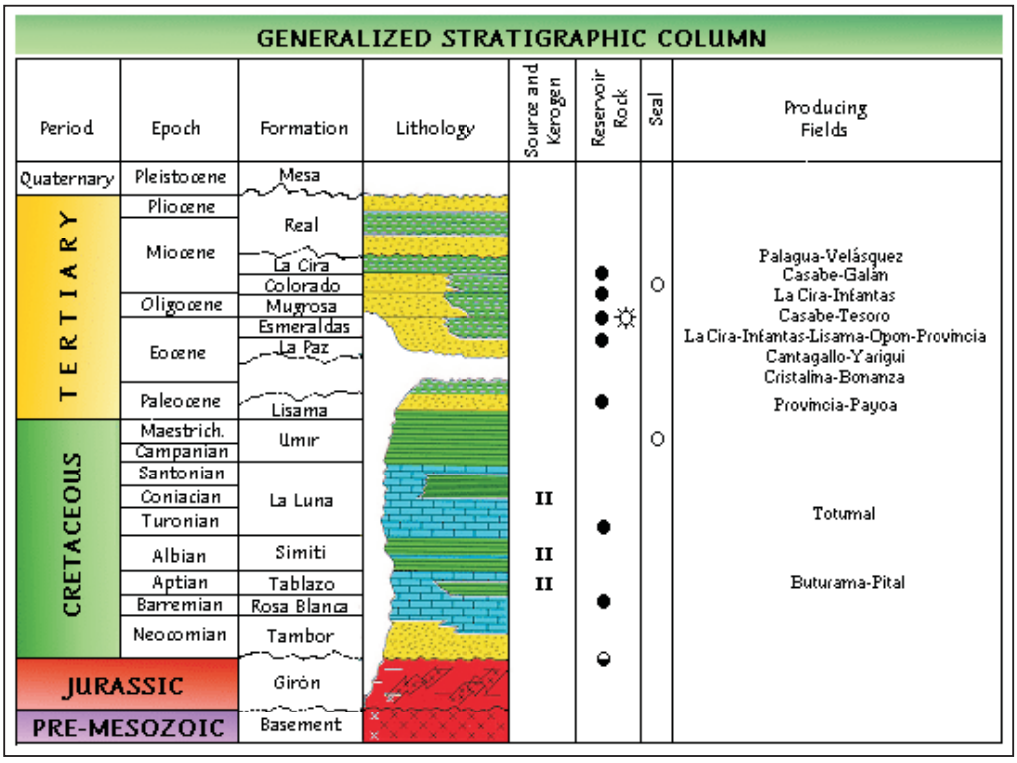

Figure 2.3: Generalized stratigraphic column of the Middle Magdalena Valley Basin. After Ecopetrol (2000).

Marine environments predominate during the Barremian to Santonian, controlling the deposition of the overlying La Paja, Tablazo, Simiti, Salto and the La Luna formations.

The Umir Formation was deposited during a regressive oscillation of Campanian-Maastrichtian age, and is comprised of shallow marine to lagoonal gray shales with interbedded coals and some sandstones (Morales et al., 1958).

The marine Cretaceous sequences are overlain by a succession of continental deposits. These strata are related to specific tectonic events in the Central and Eastern Cordilleras. The Tertiary stratigraphic column includes the Lisama Formation (Paleocene), La Paz and Esmeralda Formations (Eocene), Mugrosa Formation (Oligocene-Lower Miocene), Colorado Formation (Lower Miocene-Lower Middle Miocene), Real Group (Middle to Uppermost Miocene), and the Mesa Formation (Pliocene). These strata are composed of siliciclastic rocks deposited primarily in a continental environment, comprised of alluvial fans and a diversity of fluvial bodies (Ecopetrol, 2000; Olaya, 1997; Ramon, 1998; Suarez, 1997). Recent studies indicate two different petroleum sources associated with the Cretaceous rocks; a primary petroleum source rock in the La Luna Formation of Cenomanian to Santonian age, and a secondary source rock in the Tablazo Formation of Aptian age (Mora et al, 1996).

Although oil reservoirs discovered in the MMVB include a sequence of marine and non-marine Middle Cretaceous to fluvial Tertiary rocks, hydrocarbons have been commercially produced from Tertiary siliciclastic reservoirs. Cretaceous carbonates also show reservoir potential (Morales et al., 1952; Ecopetrol, 2000).

2.2.4 La Cira-Infantas Oil Field

The La Cira-Infantas (LCI) was the first oil field discovered in Colombia and was the largest until the discoveries of Caño Limon in 1984 and Cusiana in 1992. It was discovered by the Tropical Oil Company in 1918. La Cira-Infantas is located in the Middle Magdalena Valley Basin, near the center of Colombia, 250 km north of Bogota (Figure 2.2). The estimated oil originally in place was 3700 million barrels (MMBO). After 80 years of exploitation and the drilling of 1703 wells, the cumulative production has reached only 724 MMBO. This low recovery factor (19%) is mostly due to the heterogeneity of the reservoirs.

The siliciclastic reservoirs in La Cira-Infantas belong to the Colorado Formation (Zone A) and Mugrosa Formation (Zones B and C). Oil production comes from loosely

consolidated Tertiary sands of a highly faulted asymmetrical anticline. The net oil-sand thickness approaches a maximum of approximately 150 m on the crest of the La Cira structure (Morales et al., 1958).

The reservoir rocks are fine to medium grained, subarkosic, sometimes shaly sandstones, and are separated into three general intervals, Zones A, B, and C. Average porosity values are 20% to 23% in Zone C. Permeability may be as high as 1500 mD (Mesa, 1995; Dickey, 1992). Recent sequence stratigraphy analysis (Laverde, 1996; ICP-ECP, 1996) indicates that the depositional facies of La Cira-Infantas Tertiary rocks are associated with fluvial channel systems. Zones A and B represent mixed load channels or meandering systems, in contrast with Zone C, which was deposited as bed load channels or braided stream systems.

2.2.5 Data and Methodology

Ecopetrol collected 110 square kilometers of 3-D seismic data (24 fold) covering the entire La Cira-Infantas oil field (Figure 2.4). This seismic data were initially interpreted by Gutierrez (1996), and simultaneously integrated with geological and reservoir engineering data by a multi-disciplinary team of Ecopetrol experts. The seismic structural evaluation and subsequent discussion presented in this work are based on the original seismic interpretation by Gutierrez (1996), and new examination of the data.

The general interpretation process is as follows:

- Initially, several versions of the seismic volume were evaluated using different displays.
- In order to identify the seismic response of Tertiary siliciclastic reservoirs and associated stratigraphic units, well and outcrop data were integrated with the seismic data. Well-log curves and tops of 518 wells were converted from depth to time, using 15 well velocity functions. In addition, several synthetic seismograms were generated, and the surface geological and topography maps were loaded on the workstation.
- Based on continuity and correlation, seven seismic markers were selected for the structural mapping. Reflections were chosen that closely corresponded to the top of Sands-116, top of A-4, top of B-4, Eocene Unconformity, and the Cretaceous

calcareous levels associated to the Galembo, Salada, and Tablazo Formations (Figure 2.5).

- Seismic markers and fault planes were tracked throughout the data set in vertical section and time slices, using manual and automatic tracking techniques. Preliminary time and amplitude maps were generated for quality control and geological interpretation.

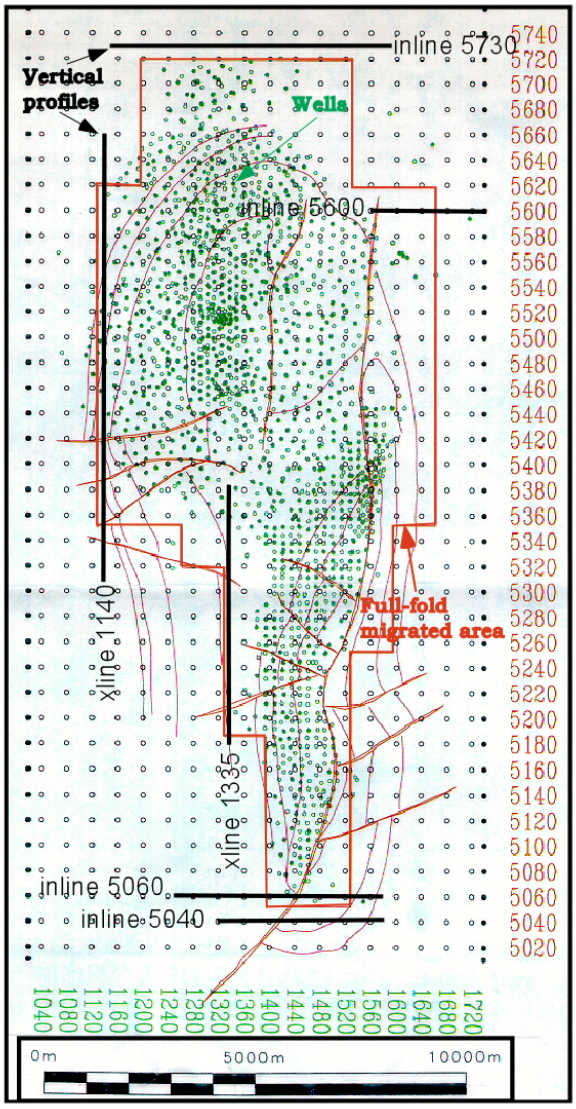

Figure 2.4: Base map of the La Cira-Infantas oil field showing the location of wells, surface geology, vertical profiles (inlines and xlines) used in this section to illustrate the structural features, and the full-fold migrated area of the 3-D seismic survey.

- Secondary horizon attributes were generated (azimuth, dip, edge, and coherence) and used to define the fault patterns. Faults traces were picked on the maps and compared with the fault traces or structural discontinuities interpreted in the vertical sections and time slices.

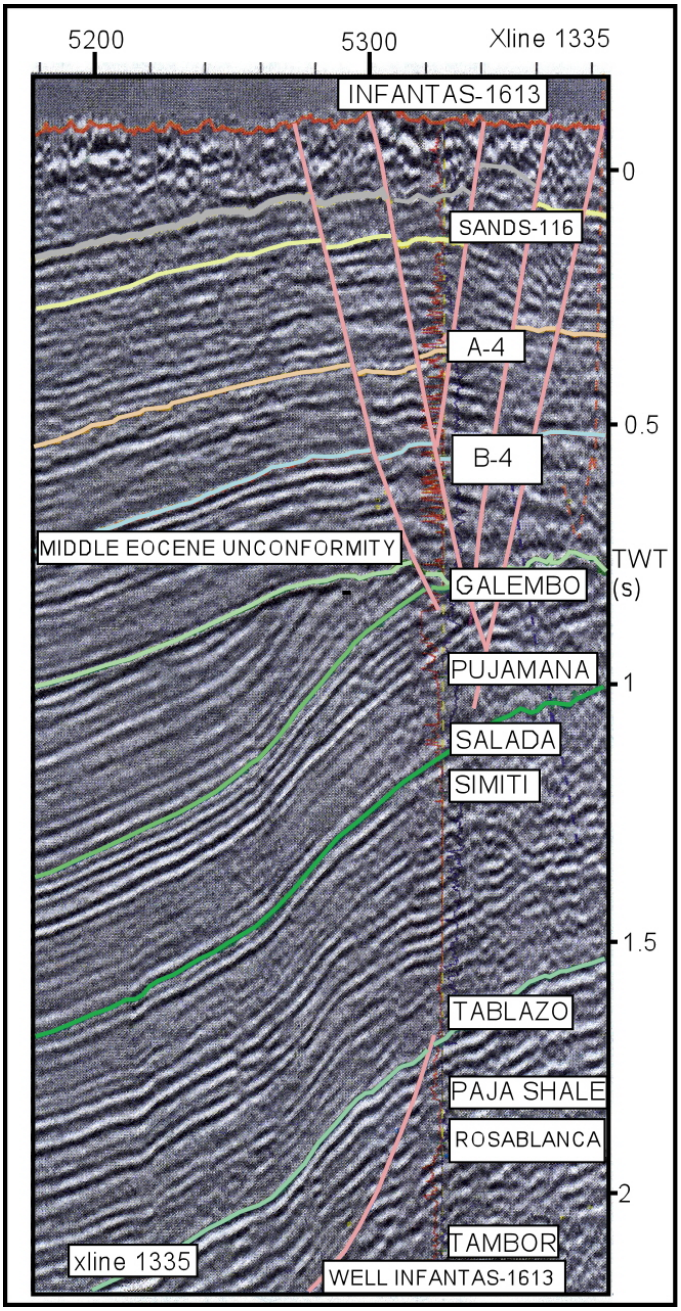

Figure 2.5: Xline 1335 showing the seven seismic markers selected for the structural mapping. The well Infantas-1613 has the most complete stratigraphic column in the area of study.

- Structural time maps were generated and their interpretation was validated, using detailed structural cross-sections and well data.
- The geometry of the delineated horizons and faults were shown as structural maps and graphs that form a base for the definition of new opportunities, and subsequent examination and discussion of the structural geology of the La Cira-Infantas oil field.

2.3 La Cira-Infantas Structural Configuration

Geographically, the La Cira-Infantas oil field is located in the central area of the MMVB. Although this area exhibits the least structural complexity in the basin, there is a prevalence of compressional structures, where pre-Cretaceous to Cenozoic rocks are deformed into an arrangement of strongly developed en echelon folds commonly faulted by closely related thrusts.

Several structural features were delineated and identified, after careful analysis of 3-D seismic data and validation with outcrop and well information. Based on the complex tectonic history of the basin and the main periods of deformation, the Cira-Infantas structural heterogeneities (folds and faults) can be divided in two main groups:

- Early Tertiary Structures
- Late Tertiary Structures

2.3.1 Early Tertiary Structures

The new seismic images show, a heavily folded, faulted, and eroded Cretaceous sequence below the Eocene unconformity (Figure 2.6). The primary structure of these Cretaceous sediments is a large antiform, elongated in the north-south direction. The west flank of this fold is well preserved in the area covered by the seismic survey and shows an approximate dip direction of $S80°W$.

The west flank of this structure is extensively cut by thrust faults that generated a series of asymmetric hanging-wall secondary folds. These folds have good exploration potential as possible deeper pool reservoirs (Figure 2.7). The structural configuration of early Tertiary structures describe here is quite different from the structural model

published by Morales et al. (1958), which consists of a long and narrow anticline below Infantas and an elongated dome underlying the La Cira structure.

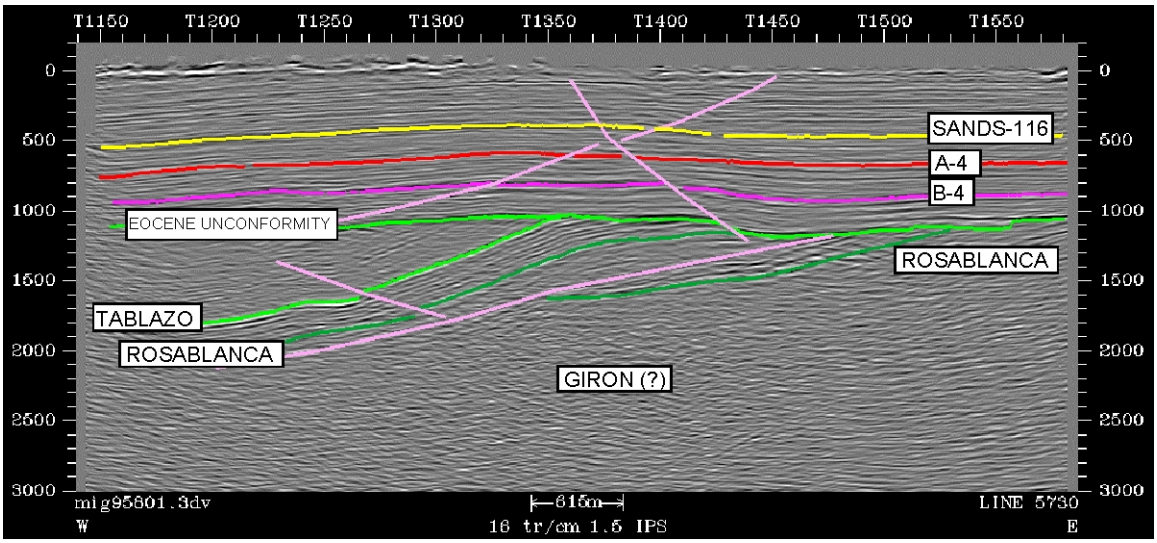

Figure 2.6: Inline 5730 showing the seismic expression of the late and early Tertiary structures in the northern La Cira area. Note the heavily folded, faulted, and eroded Cretaceous sequence below the Eocene unconformity. In contrast, the Tertiary sequence shows very minimal deformation in this area.

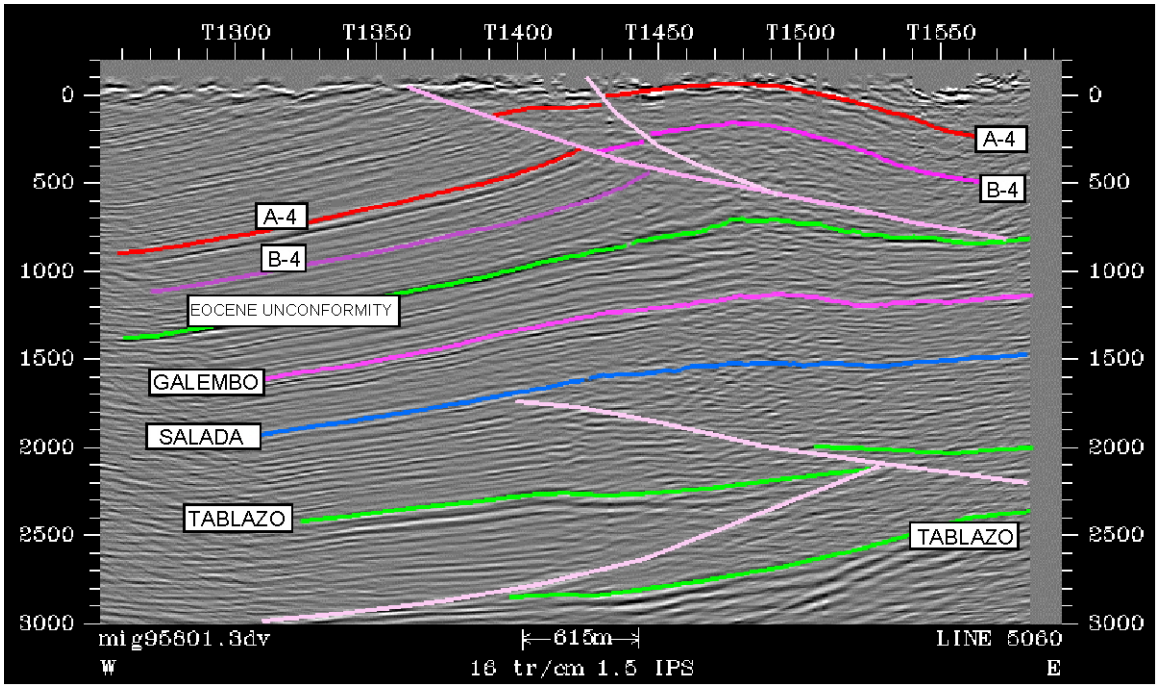

Figure 2.7: Inline 5060 showing the seismic expression of the late and early Tertiary structures in the southern Infantas area. The vertical scale units are in two-way time (ms).

2.3.2 Late Tertiary Structures

Late Tertiary heterogeneities associated with tectonic deformation are the focus of this chapter, including the La Cira and Infantas anticlines and associated features (Figures 2.8 and 2.9). The structural elements are characterized according fault attributes and bedding geometry.

Folds

The La Cira and Infantas anticlines are located in the Cachira paleohigh, a structurally controlled topographic high, which was active between the late Cretaceous and late Eocene (Olaya, 1997). Both structures show a clear and consistent left-handed en échelon-fold pattern, and appear to be the westernmost expression of a thrust belt that extends out into the MMVB from the Eastern Cordillera (Geotec, 1998 and Mojica and Franco, 1990).

Both folds have a clear surface geology expression, where the competent sandstone levels of the Tertiary formations create lineaments that clearly reflect the subsurface structural patterns. The topography also indicates the rate of faulting and folding. A uniform topographic expression with very little relief characterized the lower dip of the layers in the La Cira anticline, whereas sharp lineaments with a greater topographic configuration express the steeper inclinations of the strata in Infantas.

La Cira Anticline

The La Cira anticline is an asymmetric fold that plunges to the north and south. The axis is approximately north-south oriented and is parallel to the La Cira fault. This fault breaks the fold in the eastern flank and forms with the Infantas fault system a very gentle negative flexure in the middle. This anticline is compartmentalized by several normal faults, generally concentrated on the western flank. In contrast, the eastern synform is only slightly faulted (Figures 2.8 and 2.9).

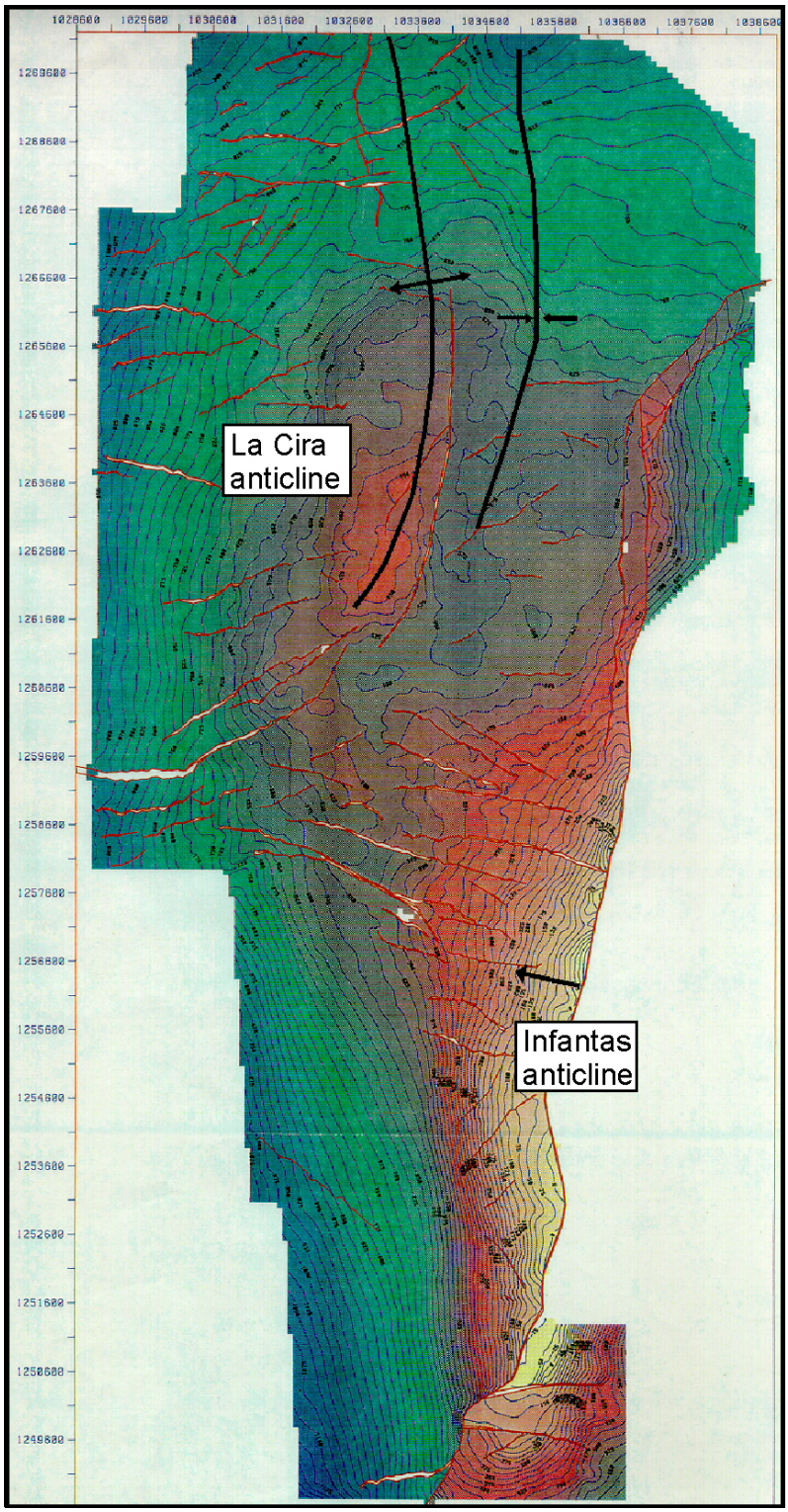

Figure 2.8: Time structural map of the B-4 marker in the La Cira-Infantas field. Yellow color indicates a high structural position.

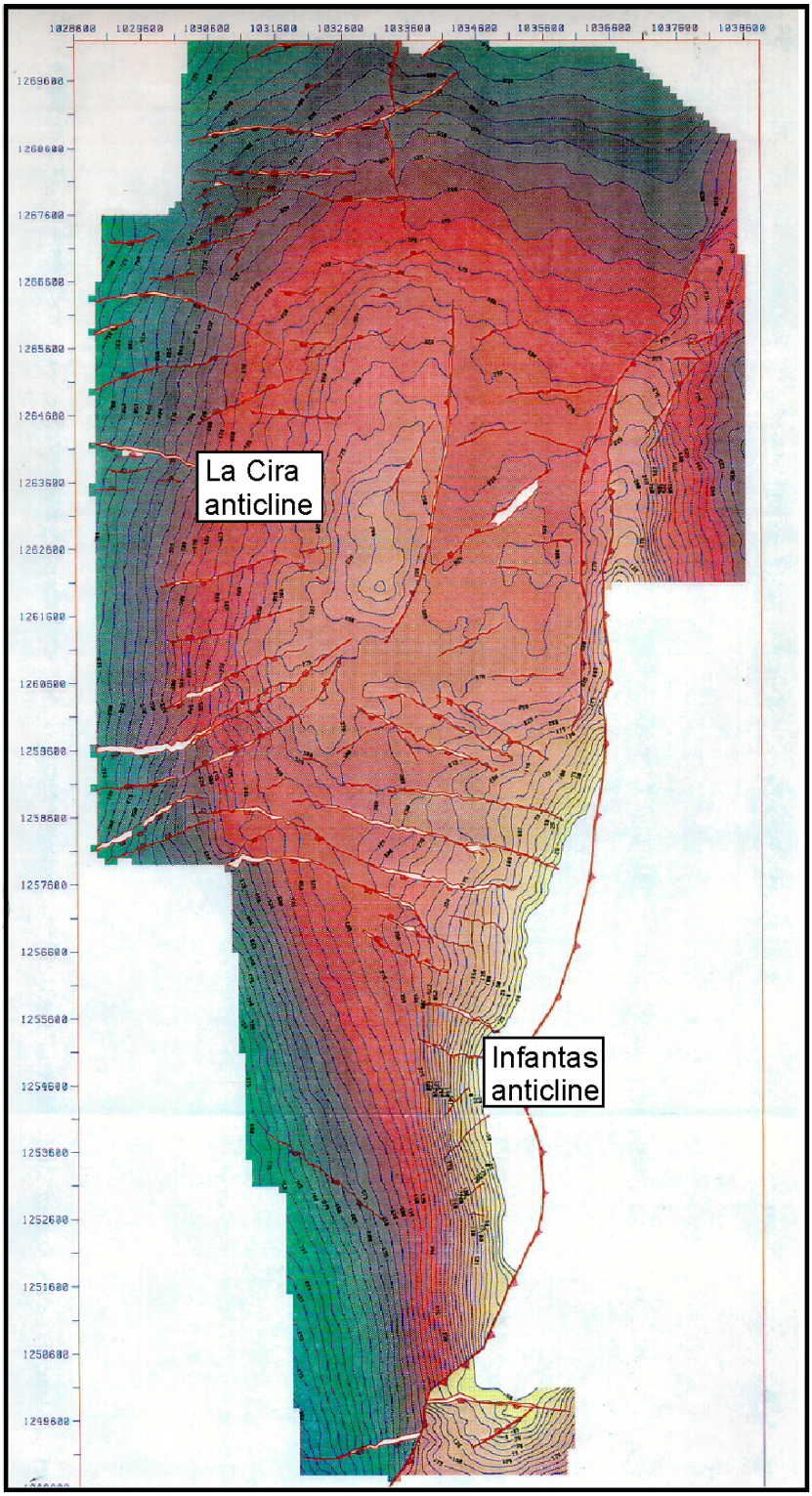

Figure 2.9: Time structural map of the A-4 marker in the La Cira-Infantas field. Yellow color indicates a high structural position.

Infantas Anticline

The Infantas fold is a narrow and elongated antiform whose axis also trends north-south. This antiform is broken along its crest line by the Infantas fault system, causing the uplift and partial erosion of the east flank. A well-preserved west flank is deformed by normal faults (Figures 2.8 and 2.9).

The Infantas fault System is the main eastern structural boundary in the oil field, playing an important role in the generation of the field trap. The former geological model based on wireline logs, suggested that the Infantas fault affected Cretaceous rocks (Morales et al., 1958). In contrast, the 3-D seismic imaging of the fault-plane area indicates that on the eastern side of the Infantas anticline, the fault plane glides on the base of the Tertiary sequence and does not affect the Cretaceous rocks. Therefore, there is a clear extension of the field to the east, where the Tertiary reservoirs truncate against the Infantas fault plane at positions that are more distant east than the easternmost Infantas wells. This new seismic interpretation of the Infantas fault system was confirmed by a recent well drilled in the hanging wall of the fault.

Thrust and Reverse Faults

Thrust and reverse faults in the La Cira-Infantas structure show a dominant NNE-SSW azimuth and east- or west-vergence. Their development is associated with the Tertiary tectonic evolution of the Central and Eastern Cordilleras (Figures 2.10 and 2.11).

Infantas Fault System

The Infantas fault system is comprised of a set of low-angle, east-vergent reverse faults that generally strike from north-south to $N30°E$. The surface exposure of their fault plane creates a sharp topographic lineament that correlates very well with the seismic expression of the fault system along the seismic survey. The offset along this system, as inferred from detailed seismic interpretation and surface geological mapping, clearly decreases from south to north in the area covered by the seismic data. Old geological interpretations (Morales et al., 1958; Irving, 1971; Mojica and Franco, 1990) show the Infantas system faulting the Cretaceous sediments.

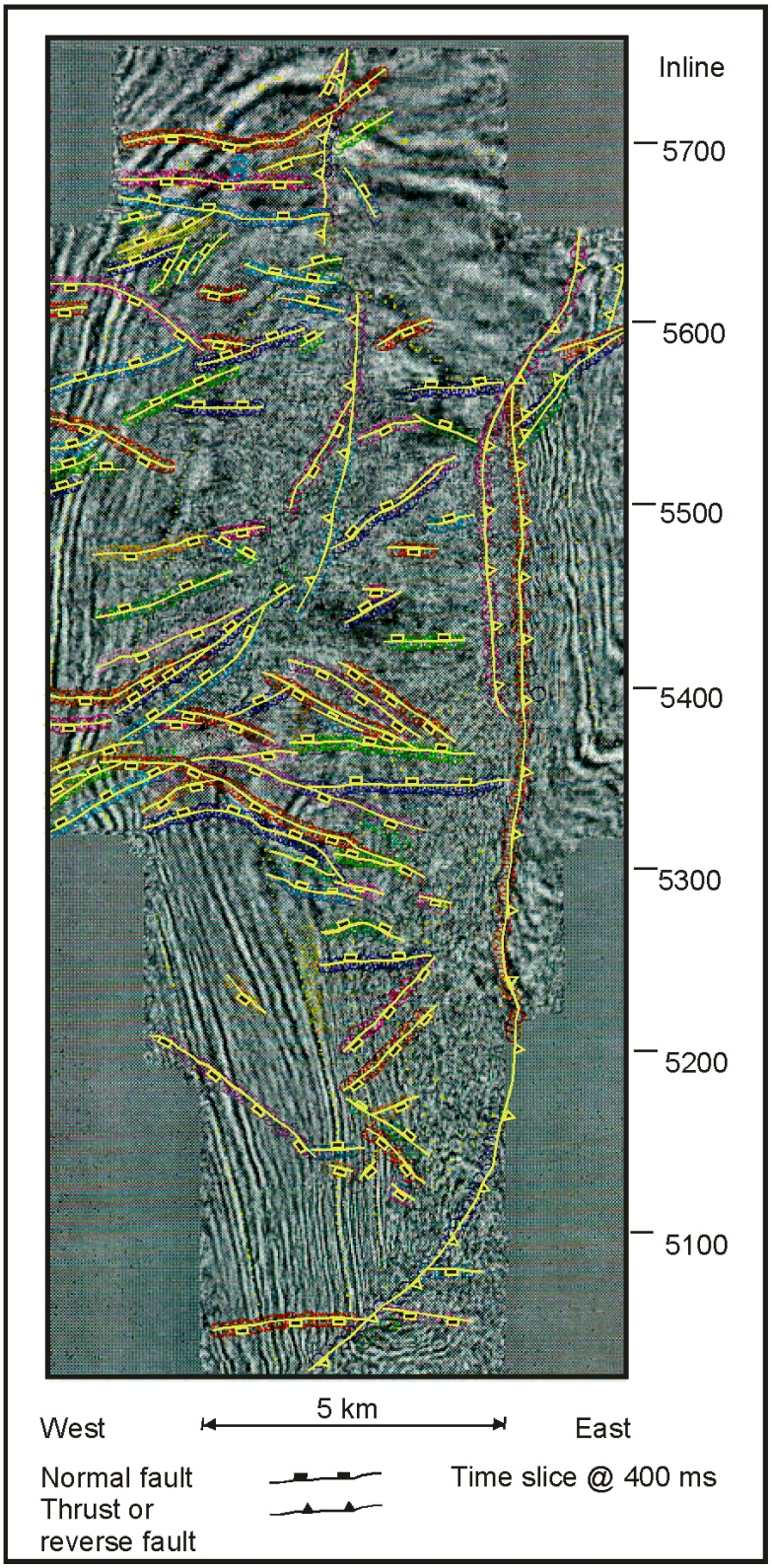

Figure 2.10: Time slice at 400 ms indicating the horizontal seismic expression and interpretation of the major structural heterogeneities

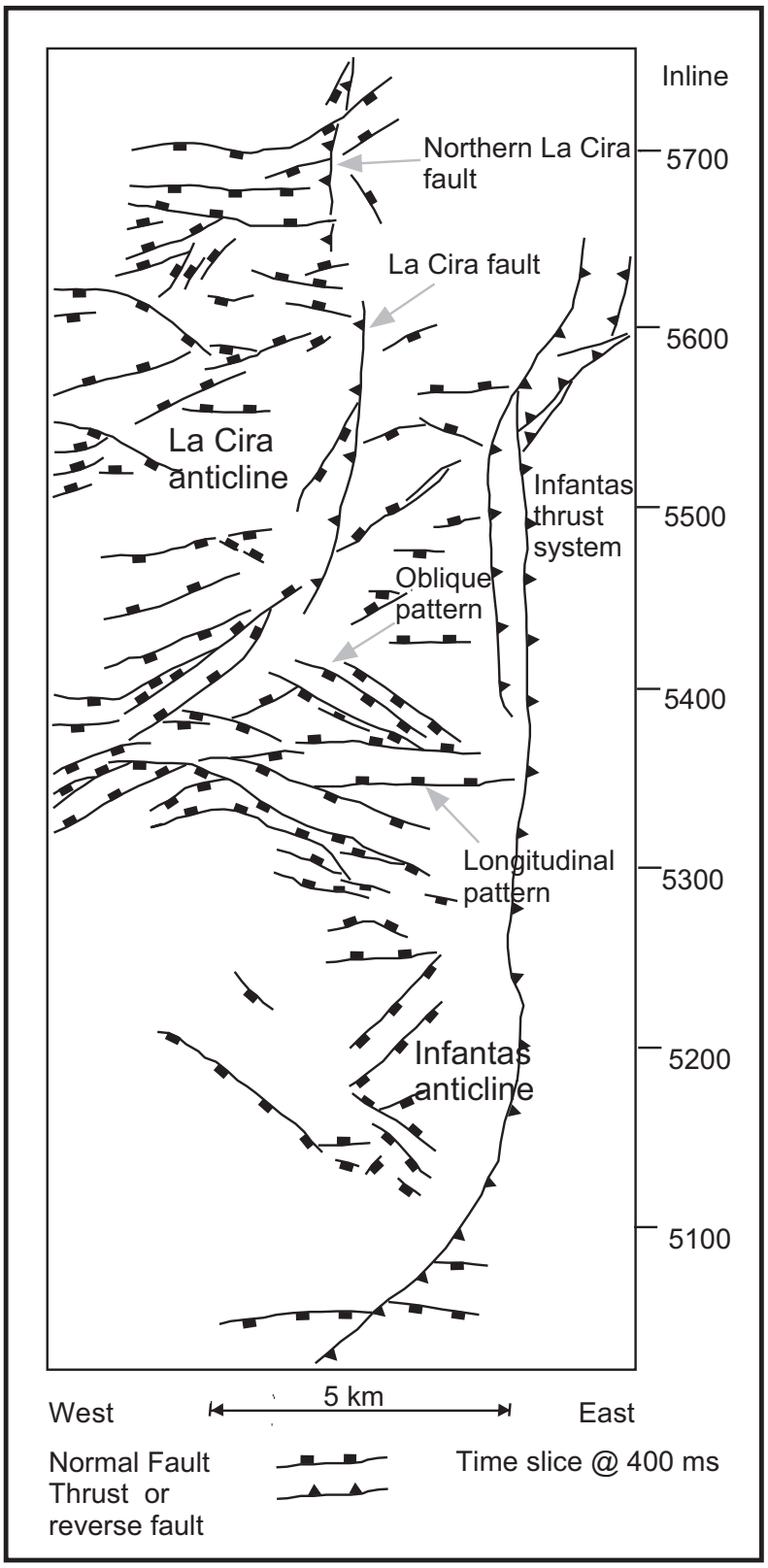

Figure 2.11: Structural patterns extracted from the interpretation of the major structural heterogeneities.

On the other hand, the new 3-D seismic data show how the fault planes of the Infantas system cut the entire Tertiary sequence, glide on a shaly section directly above the Eocene unconformity, and do not affect the Cretaceous sequence in the La Cira and Infantas areas (Figures 2.12 and 2.13). This new seismic-based description of this thrust system agrees with the probably wireline log-based interpretation published by Taborda (1965).

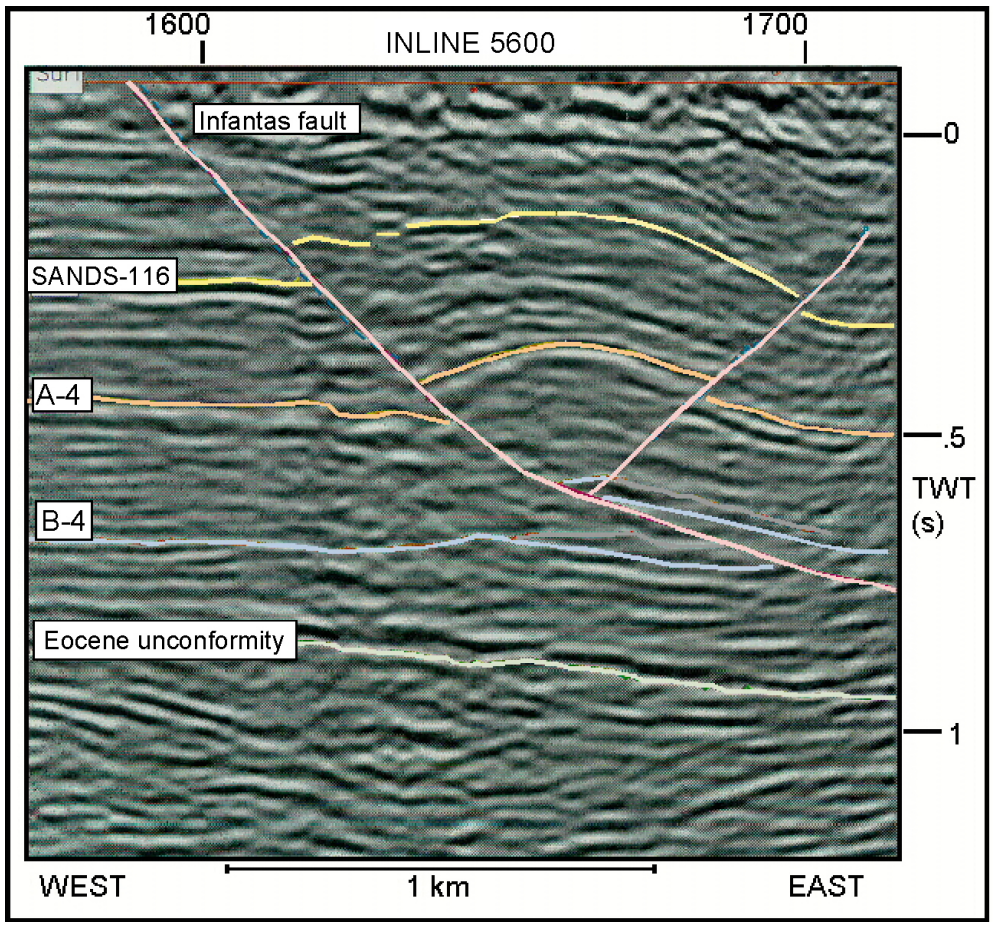

Figure 2.12: Inline 5600 showing the vertical seismic expression of the Infantas thrust on the eastern flank of La Cira anticline.

La Cira Fault

This structural feature is a high-angle reverse fault with west-vergence and a north-south azimuth. The fault is located in the central area of the La Cira anticline, showing a

surface exposure (Figures 2.8, 2.9, 2.10, and 2.11). The fault plane cuts the entire Tertiary sequence, reaching the Eocene unconformity. However, the fault does not drastically affect the Cretaceous deposits.

Northern La Cira Fault

This thrust fault is located in the northern La Cira area, presenting a low-angle plane with west-vergence, and a north-south strike. Similar to the Infantas thrust system, this fault cuts the entire Tertiary sequence, and glides on a shaly section directly above the Eocene unconformity. Some normal faults slightly cut through, displace, and divide the northern La Cira fault in three segments, creating a small variation in the strike orientation of its plane (Figures 2.8, 2.9, 2.10, and 2.11).

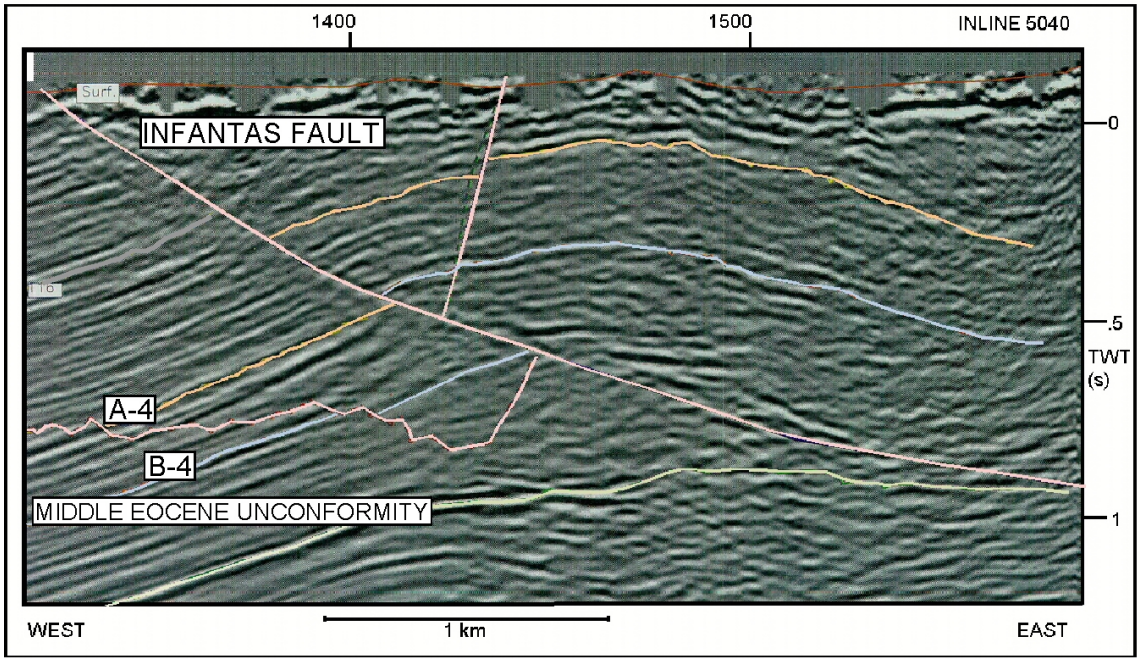

Figure 2.13: Inline 5040 showing the vertical seismic expression of the Infantas thrust in the Infantas anticline.

Normal Faults

The La Cira and Infantas anticlines are compartmentalized by many normal faults into an assemblage of reservoir blocks (Figure 2.14). On the basis of the normal fault

pattern in plan view, I identified two different and clear sets: a longitudinal set and an oblique set of faults.

Longitudinal Fault Pattern

These features are high-angle normal faults striking east-west, with variable north or south vergence (Figure 2.14). Their dominant orientation is perpendicular to the direction of the folds and thrust faults (Figures 2.10, 2.11, and 2.15). The faults appear to cut the complete Tertiary sequence, reaching the Middle Eocene unconformity and the Cretaceous rocks below. They are predominately located in the northern La Cira and northern and southern Infantas.

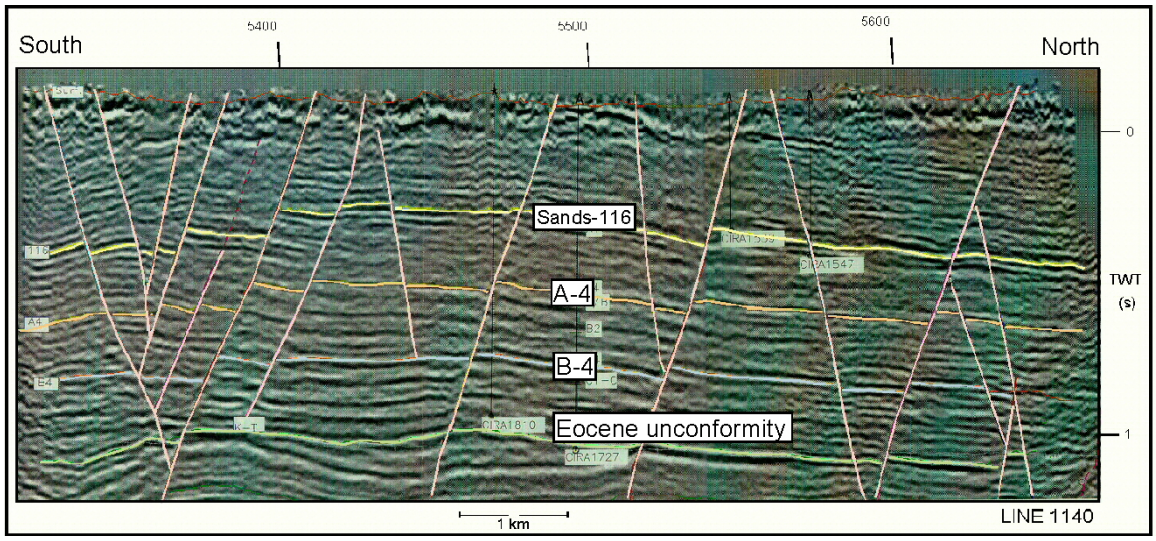

Figure 2.14: Xline 1140 showing the vertical seismic expression of the normal faults in the western flank of the La Cira anticline.

Oblique Fault Pattern

This group comprises a set of high-angle normal faults with a variable strike and dip orientation. In general, these faults strike between 0° and 30° on either side of the dominant east-west azimuth of the longitudinal set. Their dip directions change from NNW-NNE to SSW-SSE; thus, creating pairs of parallel traces with zigzag geometries (Figures 2.10, 2.11, and 2.15). In addition, there is a small group of transverse normal faults striking outside the primary range of dominant orientation.

Although most of the faults with oblique pattern show a dominant normal dip-slip displacement, some of the faults indicate juxtaposed distinctly different sedimentary thickness insinuating a strike-slip displacement (Figure 2.5). The number of faults is large and decreases with depth; therefore, the geometry of the Tertiary reservoir compartments also varies with depth. In addition, only a few main faults affect the Eocene unconformity. Figures 2.5 and 2.14 show how the vertical seismic expression of these faults reaches high complexity in the center of the field, displaying a "negative flower structure" (Lowell, 1985; Harding, 1990).

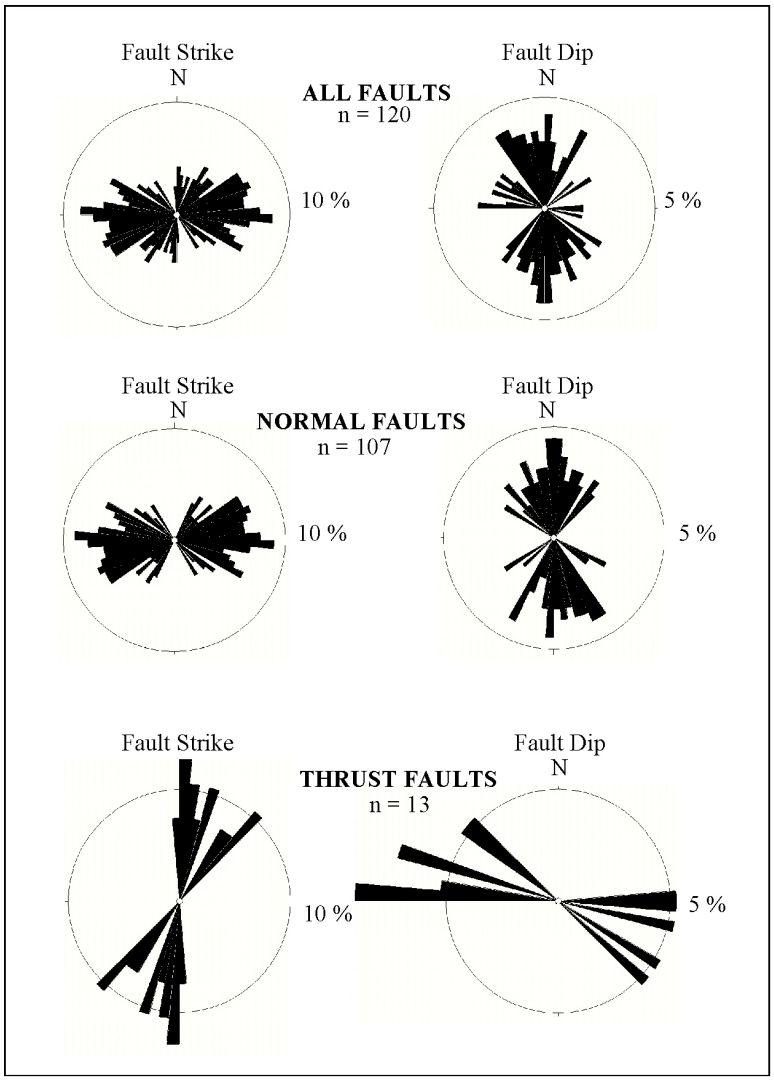

Figure 2.15: Rose diagrams of fault strike and dip orientations.

The intersections with longitudinal and oblique normal faults, and thrust faults, form in plan view complicated structures of right, acute, and obtuse angles. The normal faults are the structural heterogeneities that affect most the external geometry of the reservoir compartments, developing blocks elongated perpendicularly to the dominant north-south orientation of the La Cira and Infantas anticlines.

2.4 Slip Distribution on Normal Faults

The slip, also called displacement discontinuity, is the essential physical measurement that can be used to analyze the faults, whose description provides a better comprehension of faulting physics and the major mechanisms that control hydrocarbon distribution within the structure of an oil field. Estimation of slip along the exposed trace of a fault generally provides limited data about the slip distribution over the three-dimensional fault surface. Only the structural interpretation of three-dimensional seismic data, based on closely spaced measurements of the fault slip, permits an accurate mapping of the fault slip distribution. In this section, I present a realistic description and analysis of the slip distribution on normal faults, based on the precise 3-D seismic mapping of structural heterogeneities in the northern La Cira area, La Cira-Infantas oil field.

2.4.1 Normal Faults and Slip Distribution

A fault is a structure or narrow zone along which one side has moved relative to the other in a direction parallel to the surface or zone. Normal faults are inclined dip-slip faults along which the hanging wall block has moved down with respect to the footwall block. The measure of importance of faults is their displacement discontinuity or slip (Figure 2.16). Descriptions of the 3-D geometry of geological faults suggest that single, continuous normal faults have approximately elliptical tipline shapes, with horizontal major axes (Rippon, 1985; Barnett et al., 1987) (Figure 2.17).

Measurements of slip along the exposed trace of a fault usually provide limited information about the slip distribution over the three-dimensional fault surface. Only in a few cases, such as several multiple exposures of faults on several excavation levels, seismic imaging of many offset markers beds, and sand box experiments, can determine

the slip distribution over significant parts of a fault plane (Burgmann and Pollard, 1994; Willemse and Pollard, in press).

The actual dip slip (measurements of throw and heave) cannot be measured with conventional subsurface data sources, e.g., well logs. In contrast, 3-D seismic reflection surveys facilitate the detection of subtle variations of the components of dip slip. A good example is found through the analysis of the slip distribution in a set of structures located in the northern La Cira area, where normal faults slightly crosscut and offset compressive structures (Figure 2.18).

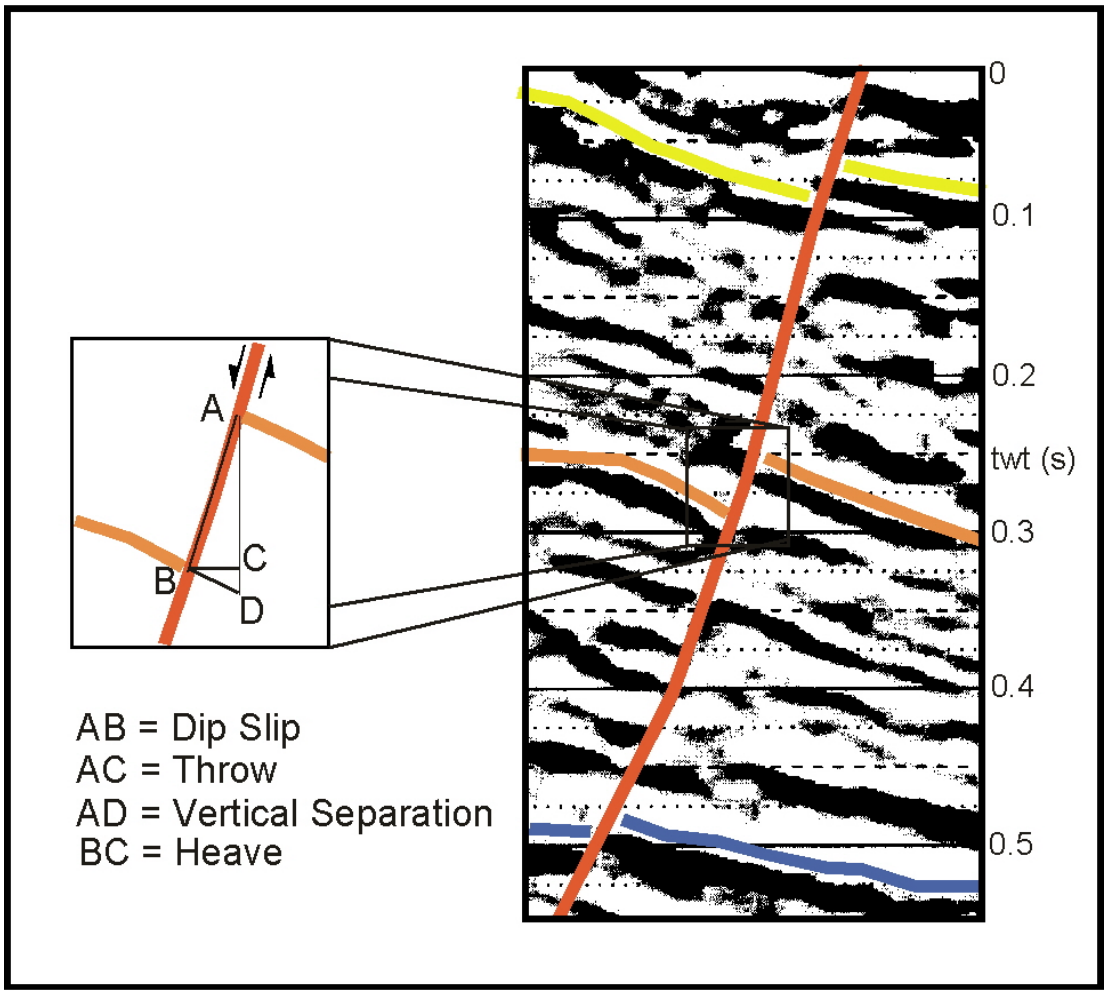

Figure 2.16: The fault slip term describes the actual relative displacement of a fault and is defined as the measurement of the distance of the actual relative motion between two formerly adjacent points on opposite sides of a fault (Adapted from Tearpock et al., 1991).

2.4.2 Northern La Cira Area

In this section, I focus the analysis of the slip distribution on a set of structures located in the northern La Cira, where normal faults slightly crosscut and offset compressive structures (Figure 2.19). This area is covered by good quality 3-D seismic data. Although the structural interpretation of 3-D seismic data provides valuable fault information for the analysis of the slip distribution, some assumptions are made:

- The data being used are of reasonable quality.
- The two-way time-to-depth conversion is known.
- The seismic markers have been interpreted correctly.
- Interpreted north-south seismic lines (xlines) are oriented perpendicular to the strike of the fault.

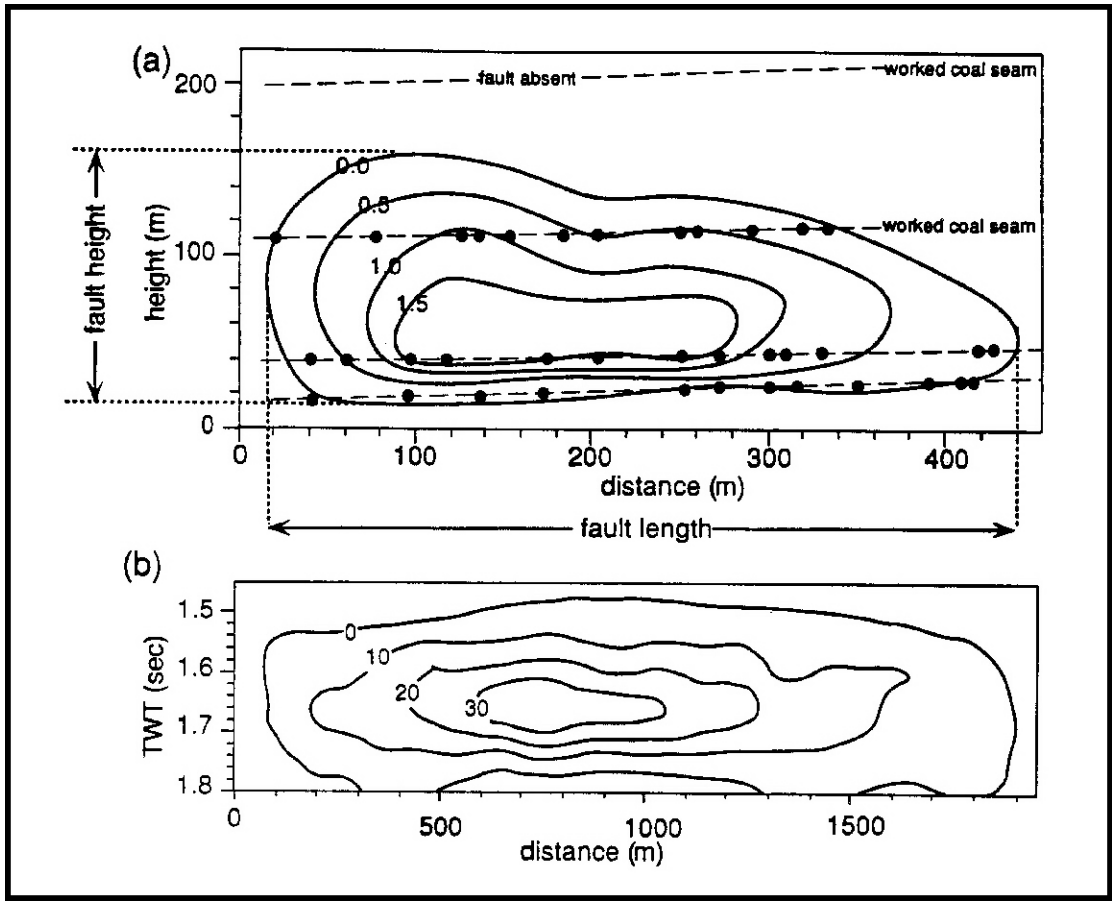

Figure 2.17: Descriptions of the three-dimensional geometry of ancient faults indicate that single and continuous normal faults have more or less elliptical tipline shapes with horizontal major axes (Willemse and Pollard, in press).

The elements of this analysis are summarized as follows:

- Initially two seismic markers related to the Sands-116 and A-4 reservoirs were selected and interpreted along the principal normal fault FCNC1 in this area (Figure 2.20). Based on standard interpretation techniques, the FCNC1 fault is described as a continuous normal fault (see section 2.3).

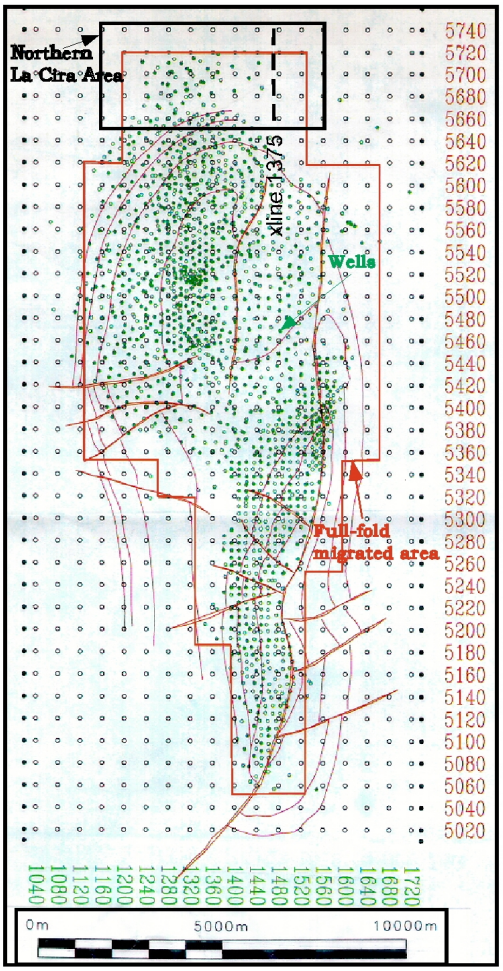

Figure 2.18: Base map of the La Cira-Infantas oil field showing the location of oil wells, surface geology, full-fold migrated area of the seismic survey, and the vertical profile (xline 1375) and the time slice in the northern La Cira area used in this section to illustrate the structural features.

- Collection of throw measurements in x-lines with 75 m separation. The throw is defined as the difference in vertical two-way time between the intersection of the fault surface with the seismic markers (Sands-116 and A-4) in both the footwall and hanging wall fault blocks (Figure 2.21).

- Conversion of the throw measurements into a set of dip slip data, using a simple geometric correction related to the average dip of the fault plane.
- Transformation of the two-way time slip data into depth slip data, using a detailed velocity function.
- Plotting of the dip slip as a function of the horizontal distance on the fault.

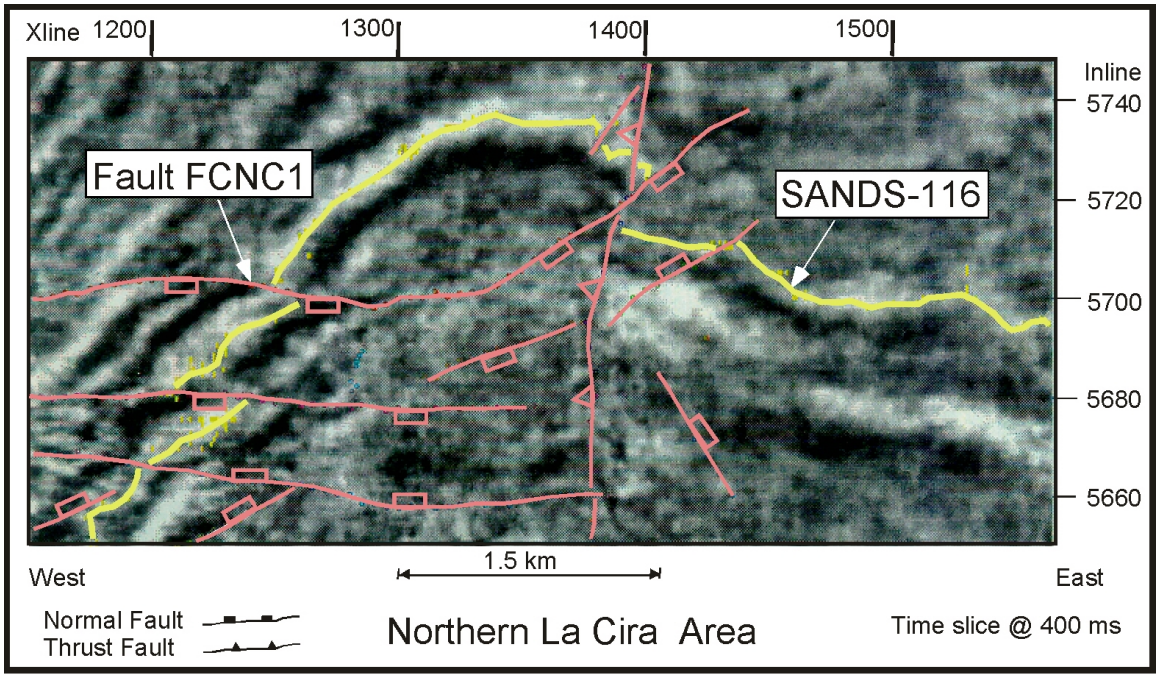

Figure 2.19: Time slice at 400 ms showing the horizontal seismic expression of the structural features that characterize the northern La Cira area.

Detailed examinations of the dip slip distribution on some of the normal faults in this area (e.g., normal fault FNCN1), does not follow the simple pattern usually expected from single and continuous normal faults, where the tipline shapes are symmetrical and elliptical (Figure 2.22). For example, the description of dip slip along the seismic markers Sands-116 and A-4 shows that the normal fault FNCN1, formerly interpreted as a continuous fault, consists of at least five overstepping segments (Figure 2.23). Some segments show a general symmetrical distribution about a central dip slip maximum (Figures 2.20 and 2.22).

These results agree quite well with some slip distribution models derived by Willemse and Pollard (in press), that show normal faults as a patchwork of segments,

linked along lines parallel and perpendicular to the overall slip vector. The non-uniform slip distribution along the main fault surface could affect the hydraulic behavior of the faults and create production problems in La Cira-Infantas. Therefore, integrating the slip analysis into the reservoir studies is essential to characterize flow paths, permeability, sealing capacity, and reservoir compartmentalization.

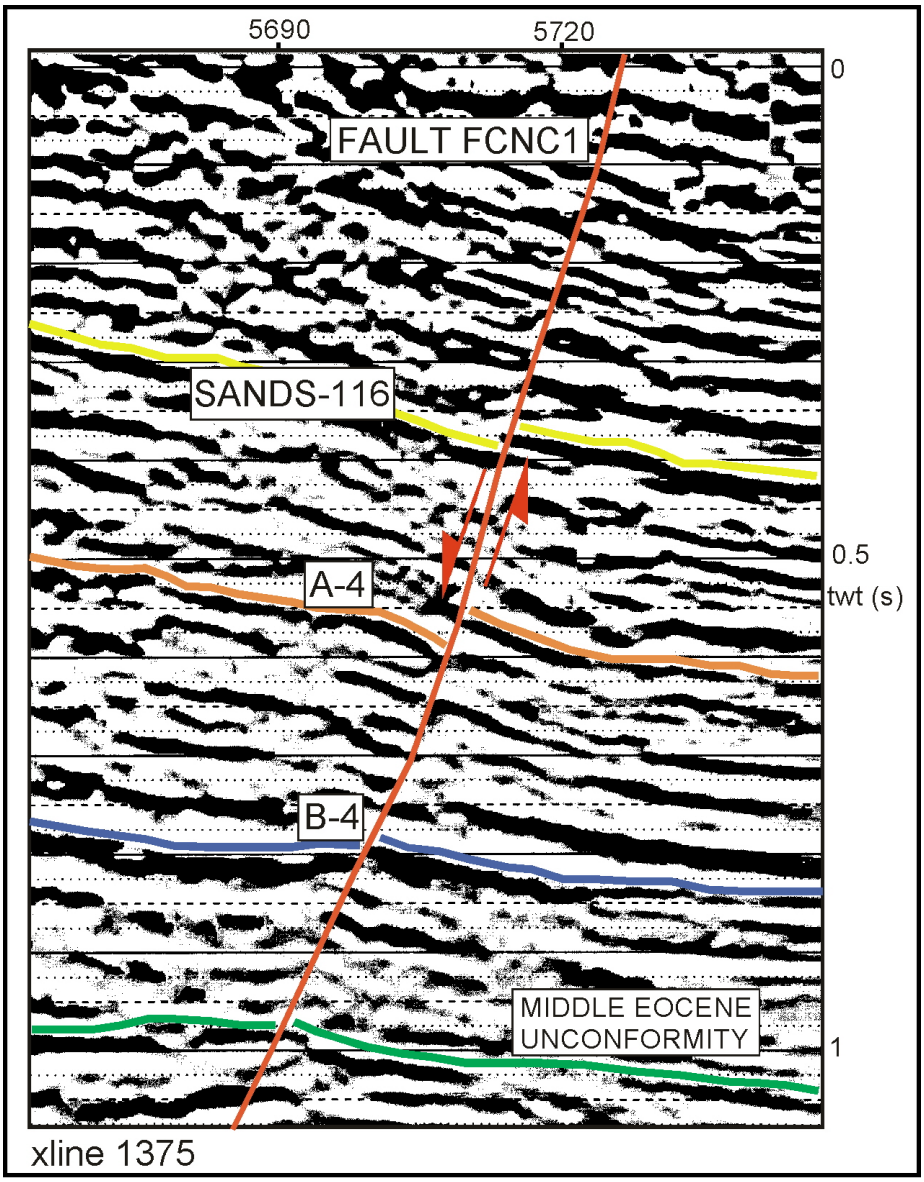

Figure 2.20: Xline 1375 showing the vertical seismic expression of the normal fault FCNC1. Note how the dip slip changes along the fault plane and shows a maximum central slip around the intersection with the A-4 marker.

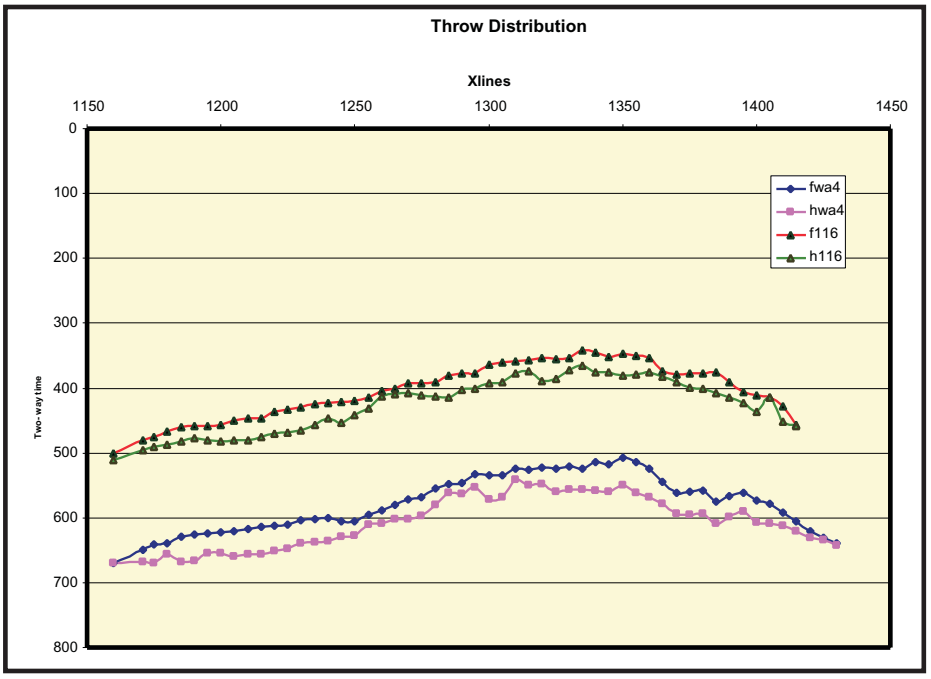

Figure 2.21: Strike projection of fault throw along the FCNC1 fault. The throw is the difference in vertical two-way time between the intersections of the fault surface with the seismic marker (Sands-116 and A-4) in both the footwall and hanging wall fault blocks.

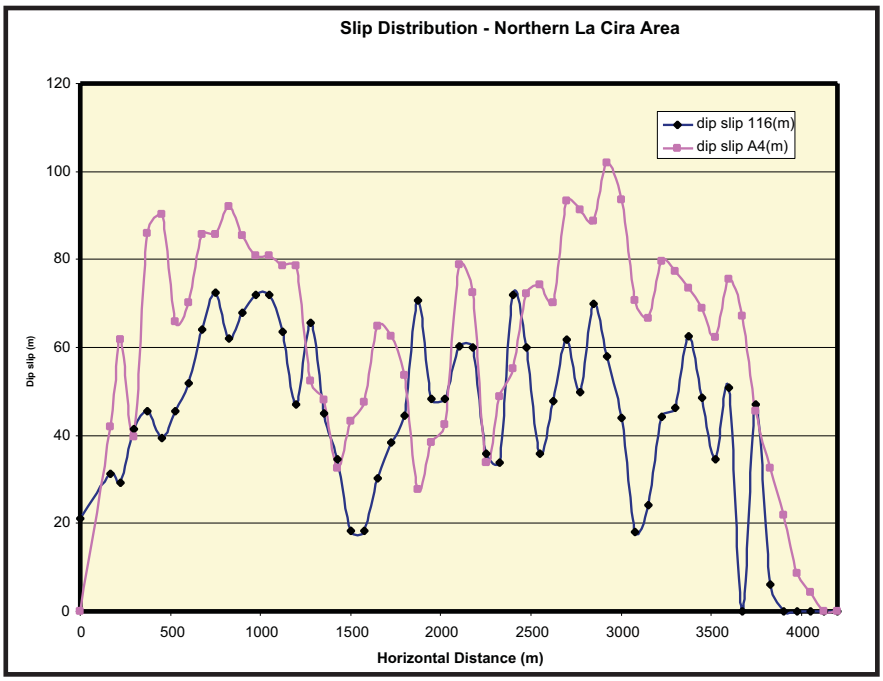

Figure 2.22: Strike projections of the dip slip distribution along the intersection of the FCNC1 fault with the seismic markers Sands-116 and A-4.

Moreover, the orientation of the fault segments is consistent with the pattern-based classification of the normal faults in La Cira-Infantas. While the western segments A, B, and C in Figure 2.23 are part of the faults that show a longitudinal pattern oriented east-west, the eastern segments D and E are part of the group of normal faults with oblique pattern in map view.

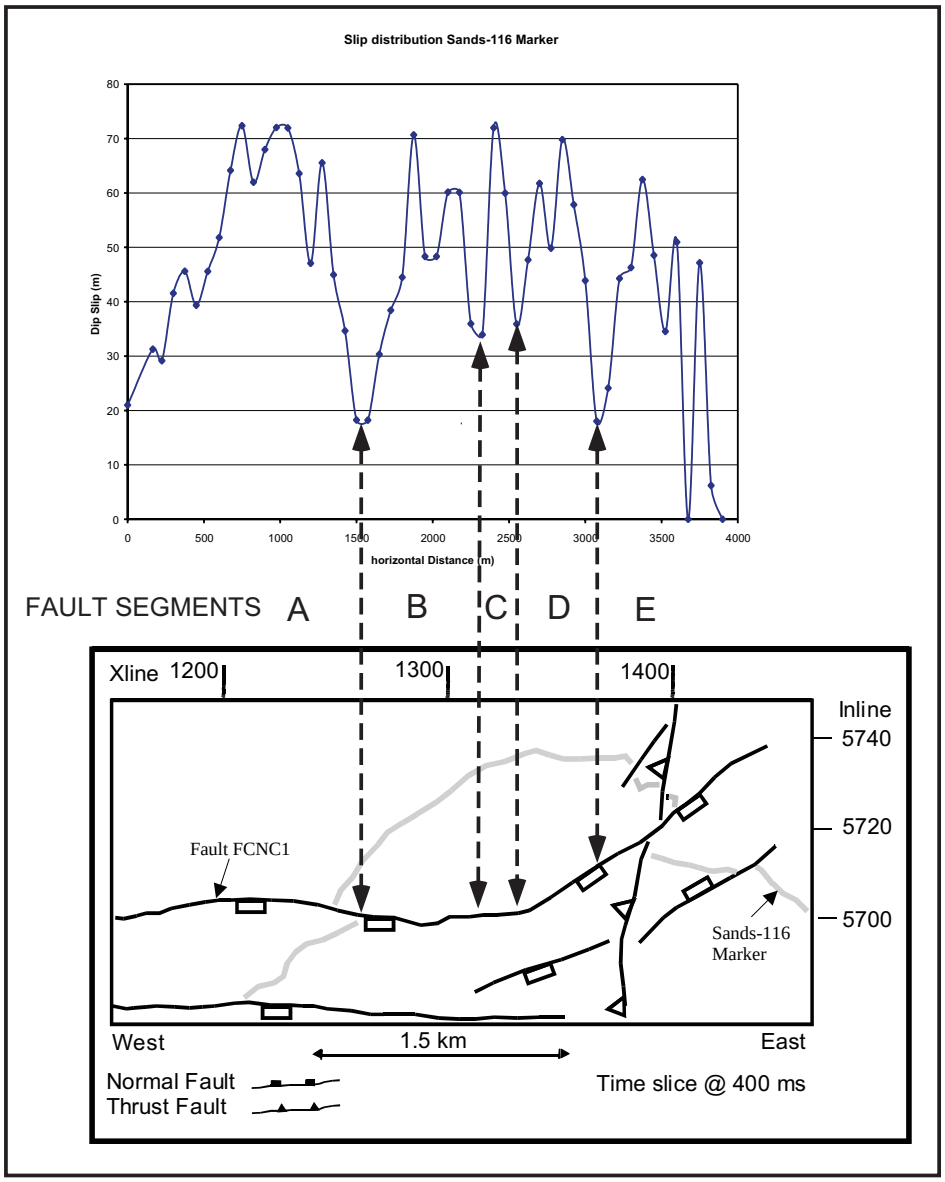

Figure 2.23: The distribution of the slip along the intersection of normal fault FNCN1 and the seismic marker Sands-116 suggests that this fault in the northern La Cira area, formerly interpreted as a continuous fault plane, consists of at least five overstepping segments (A to E). Western segments A, B, and C are part of the faults that show a longitudinal pattern oriented east-west, and eastern segments D and E are part of the group of normal faults with an oblique pattern in map view.

The slip is highly variable. These changes in the theoretical elliptical shape may be associated with variations in the frictional strength along the fault plane, spatial gradients of the stress field, inelastic deformation near fault terminations, variation of the elastic modulus of the host rock, or mechanical interaction with other faults (Burgmann and Pollard, 1994; Willemse et al., 1996; Maerten et al., 1999).

2.5 Structural Style

The late Tertiary structure of the producing trend of the La Cira-Infantas and contiguous Colorado and Mugrosa oil fields can be interpreted regionally as a relatively simple parallel and small-displacement wrench zone. The structural style consists of a single alignment of anticlines, arranged in a left-handed en échelon pattern, which are highly fractured by coexisting normal and reverse separation faults.

Wilcox et al. (1973) originally described a "simple parallel wrench fault" as a fault zone along which there is no indication for preferred convergence or divergence. Later, other workers used different terms for this kind of deformation. Harding and Lowell (1979) used "side-by-side wrench faults", Mann et al. (1983) used "slip-parallel faults", and Biddle et al. (1985) use "simple strike-slip faults". I employ the original definition of a simple parallel wrench fault in this work.

Simple parallel wrenching is a particular case of simple shear, where external rotation occurs in addition to internal rotation, and an expected geometric arrangement of structural features is generated (Lowell, 1985). Simple wrenching is the outcome of motions of crustal sections in opposite orientations parallel with their contiguous boundaries, where compressional and tensional stresses are generated in the overlying sedimentary cover. Crustal deformations and lab experiments indicate that the earliest deformations are plastic and included folding, followed by a mixture of plastic distortion and fracturing (Wilcox et al, 1973).

Figure 2.24 shows a strain ellipse of a left-lateral couple that effects rotational shear and shows the forces and combination of structural features that can arise from wrenching deformation. It also indicates the extensional and compressional components. The main structural features of the fundamental wrench model are: (a) en échelon folds, which are generally the earliest of the structural assemblage to grow normal to the

compressional direction and inclined at a low angle to the wrench zone. Situated in the same direction of the fold axes, thrust or reverse faults may appear during subsequent levels of fold deformation; (b) after origin of the folds, conjugate strike-slip faults or Riedel shears develop, comprised of synthetic faults inclined at a low angle to the wrench but in opposite orientation from the folds, and antithetic faults almost perpendicular to the wrench zone; (c) secondary synthetic faults or P shear, also inclined at a low angle to the wrench but in a similar orientation from the folds; (d) the main wrench or master fault, parallel or subparallel with the wrench zone; and (e) normal faults oriented perpendicular to the fold axes and the component of extension (Wilcox et al, 1973; Lowell, 1985; Biddle and Christie-Blick, 1985).

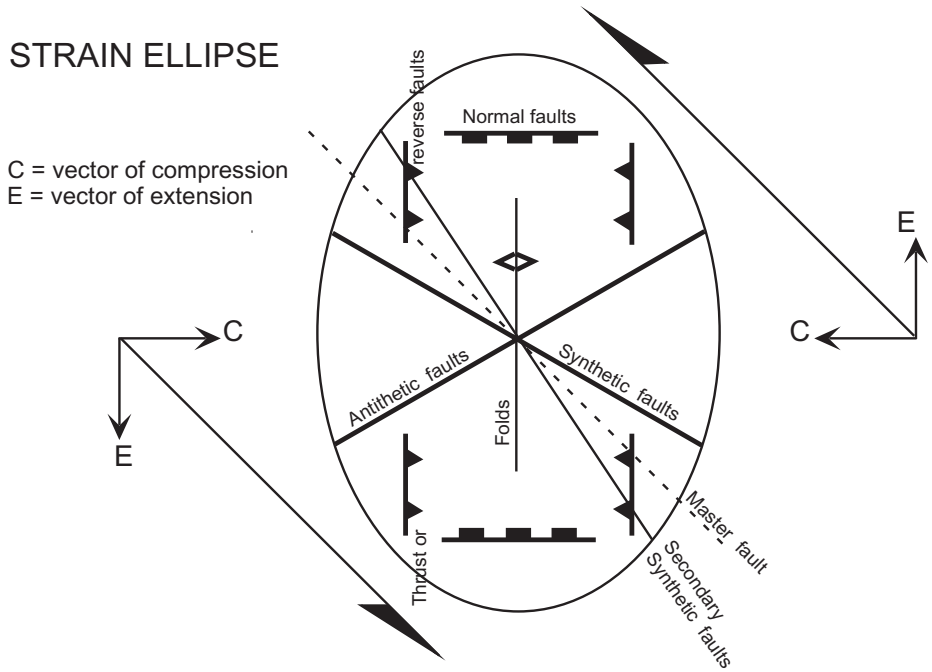

Figure 2.24: Wrench assemblage showing the angular relations between structural features that have a tendency to form in a left-lateral simple shear under perfect conditions (After Biddle and Christie-Blick, 1985).

2.5.1 Evidence of Wrenching

As I mentioned in section 2.3.2, the structural style of the La Cira-Infantas oil field consists of a single assemblage of anticlines. These anticlines are arranged in a left-handed en échelon pattern and are highly broken by coexisting normal-and reverse faults.

The La Cira-Infantas zone shows some structural characteristics, which support its classification as a small-displacement and simple parallel wrenching case, where important compressive and extensional forces are generated along the area of deformation. These forces are demonstrated by the development of both coexisting compressive and extensional structures

Small-displacement wrenching zones are characterized by sets of en echelon fold closures, which obliquely straddle the early stage wrench fault. In addition, strike-slip fault displacements are not enough to produce a major slip in facies or to interrupt general structural continuity (Harding, 1974). The strain ellipse of a left-lateral couple is used to compare the set of theoretical and experimental structural elements with the real structural patterns at field scale in La Cira-Infantas, in addition to the structural patterns at regional scale in the MMVB (Figure 2.25).

Although the prediction of the structural patterns based on experiments and theory include many assumptions, such as homogeneity of rocks, instantaneous deformation, and non-rotation of early-formed structures (Christie-Blick and Biddle, 1985), the La Cira-Infantas structural features adjust very well with the predicted ones. The elements that support the wrench model for the La Cira-Infantas structure are en échelon folds, normal folds, conjugate strike-slip faults, thrust and reverse faults, and parallelism of zone with documented wrench faults.

En Echelon folds

Biddle and Christie-Blick (1985) define "en échelon " as "a stepped arrangements of relatively short, consistently overlapping or underlapping structural elements such as faults or folds that are approximately parallel to each other but oblique to the linear or a relatively narrow zone in which they occur" (Figure 2.26). The structure of the producing trend of La Cira, Infantas, and adjacent Colorado and Mugrosa anticlines reveal a clear and consistent left-handed en échelon fold pattern, which obliquely straddle a very early incipient or non-developed wrench fault. These folds have been developed perpendicularly to the compressional component of the wrenching deformation.

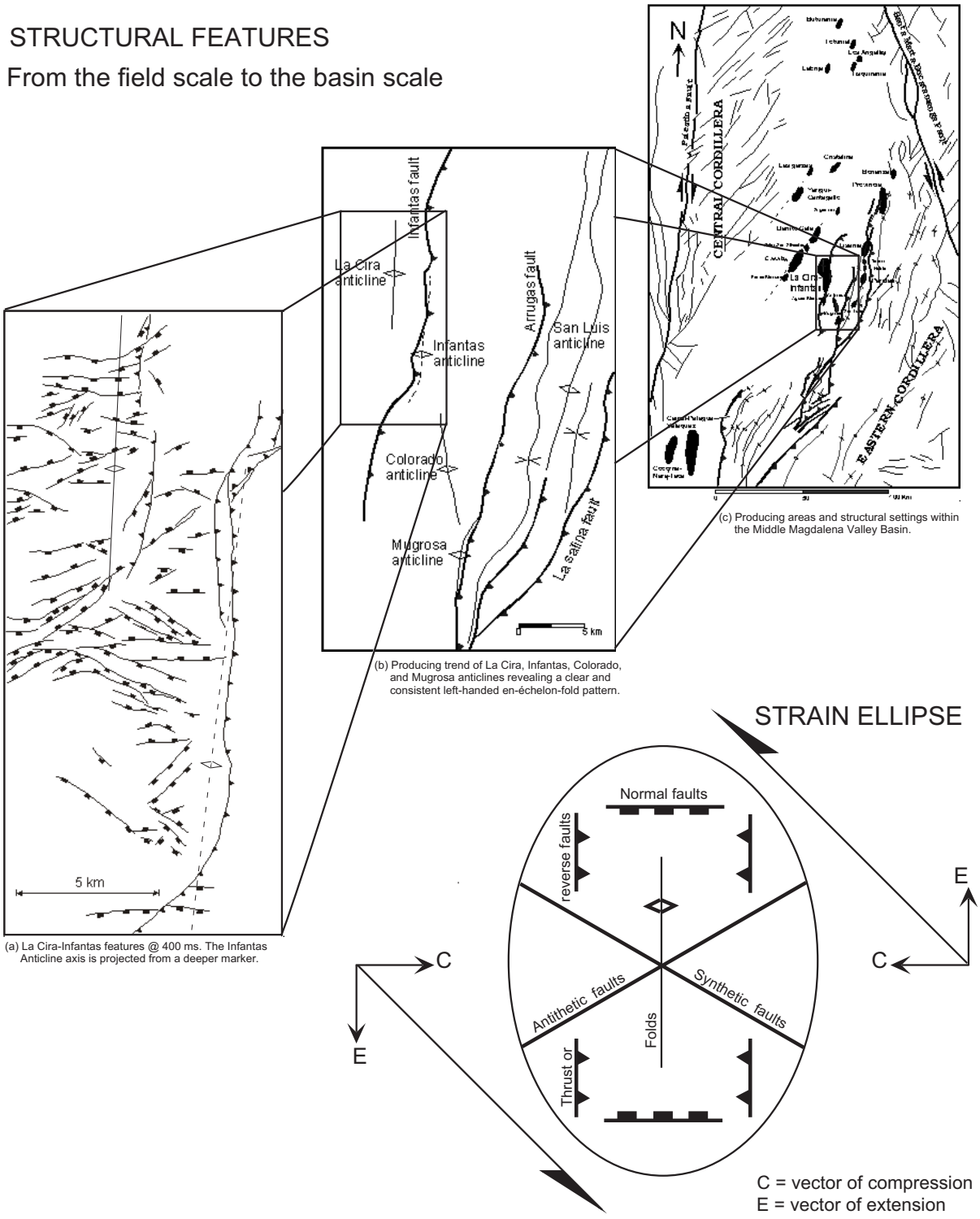

Figure 2.25: Diagram showing the structural features from the field scale to the basin scale. Also shown is how good they fit, especially the La Cira-Infantas field features, into a strain ellipsoid oriented according to an incipient, small-displacement, and parallel strike-slip fault zone. The master and secondary synthetic faults were not formed, since these features are usually developed in advanced stages of wrenching deformation (Wilcox et al., 1973; Christie-Blick and Biddle, 1985).

This en échelon fold pattern is geometrically different than the "relay" pattern shown by the San Luis anticline and parallel folds, which control the producing trend of San Luis, Lisama, Provincia, and other oil fields. The relay pattern characterizes typical tectonic regimes associated with regional shortening, as the closed thrust-front of the Eastern Cordillera (Figure 2.25, 2.26, and 2.27), rather than with strike-slip tectonics (Harding and Lowell, 1979).

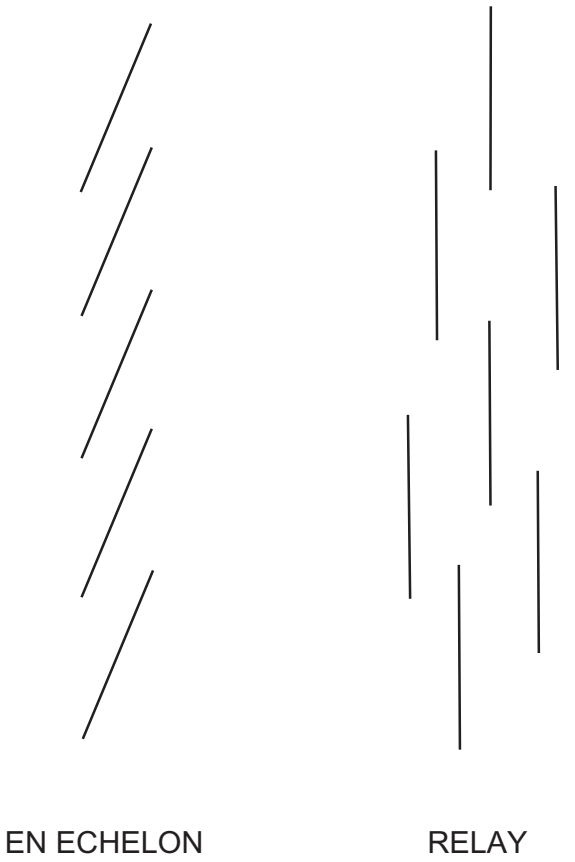

Figure 2.26: Simple structural patterns (Harding and Lowell, 1979; Christie-Blick and Biddle, 1985).

Normal Faults

A longitudinal set of normal faults has developed parallel to the short axis of the strain and the extensional component. This set crosses the en échelon fold axes at right angles and bisects the acute angle between the oblique fault set.

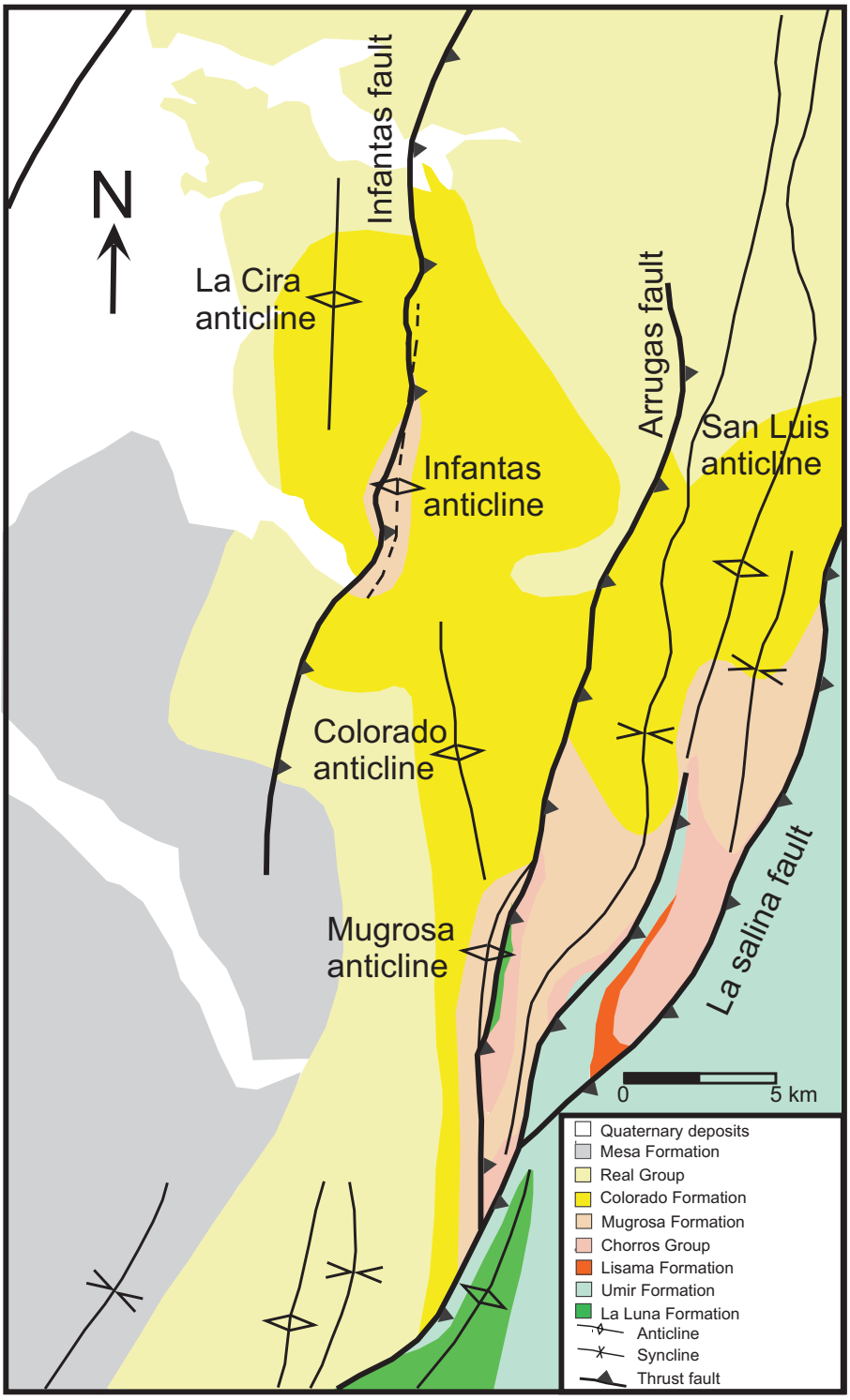

Figure 2.27: Geological map of the La Cira-Infantas area and closed structures (Ingeominas, 1966; Ingeominas, 1967).

Conjugate Strike-Slip Faults

Wrenching also probably developed in the La Cira-Infantas set of faults that show an oblique pattern in plan view (section 2.3.2). Based on their orientation, these faults can be divided in two groups. The main and largest group is characterized by antithetic faults that intersect the wrench strike at an angle between $60°$ and $90°$. In contrast, a smallest group of synthetic faults makes an angle between $10°$ and $30°$ with the wrench azimuth.

These kinds of faults, like in the La Cira-Infantas wrenching case, possibly inherit some of the extensional component of the wrench deformation and become vertical normal faults with negligible lateral displacement (Wilcox et al., 1973). Only in a few cases does this set of faults show juxtaposed dissimilar sedimentary thickness suggesting a clear strike-slip displacement (Figure 2.5).

Thrust and Reverse Faults

The Infantas thrust system, La Cira-Norte thrust, and La Cira reverse fault show a parallel orientation with the dominant north-south strike of folding, and were probably developed during subsequent stages of fold deformation. These faults were also developed normal to the compressional component of the wrench tectonics.

Parallelism of Zone With Documented Wrench Faults

Regionally, the linear and solitary zone of deformation that includes the La Cira, Infantas, Colorado, and Mugrosa anticlines and associated faults has a distinct parallel orientation with respect to the major and well-know Santa Marta-Bucaramanga wrench fault, which shows a large demonstrable lateral offset (Figure 2.25). The Santa Marta-Bucaramanga fault is a left-lateral, northwest-southeast trending, strike-slip fault. Campbell (1968) suggests a 110 km left-lateral displacement. Other workers support Campbell's strike-slip estimation with recent arguments and correlations (Kellogg, 1984; Pindell et al., 1998).

In addition, the geological map of the La Cira-Mugrosa trend reveals a regional antiform striking NNW-SSE, rather that the dominant NNE-SSW orientation of the structures in the Eastern Cordillera (Figure 2.19). The evolution of incipient strike-slip

faults, characterized by a zone of parallel and small displacement, as the structural model proposed for the La Cira-Mugrosa trend in this work, are documented in experiments (Wilcox et al., 1973). Similar geological analogs to the La Cira-Mugrosa trend are illustrated in well-studied tectonic regimes. For example Harding (1974) describes strike-slip faults with very small lateral displacement in the Newport-Inglewood zone, Los Angeles Basin.

2.6 Phases of Deformation

Proposed tectonic models for the MMVB indicate that this geological depression was initially an early Tertiary foreland basin originated by uplift of the Central Cordillera to the west. Later, during the Miocene-Pliocene deformation of the Eastern Cordillera, it became an intermontane basin (Morales et al., 1958; Taborda, 1965; Mojica and Franco, 1990; Schamel, 1991; Montgomery, 1992; Dengo and Covey, 1993; Cooper et al., 1995). Some workers even suggest an initial uplift of the Eastern Cordillera during the Oligocene (Villamil et al., 1999; Restrepo-Pace et al., 1999b).

Gomez (1997), Gomez and Jordan (1998), Gomez et al., (1998), Gomez et al., (1999a), Gomez et al., (1999b), and Gomez et al., (2000), proposed that during the early Paleogene the MMVB was a segmented foreland basin, having its source of sediments in the Central Cordillera, intrabasinal highs, and the Eastern Cordillera, whose uplift started in the early Paleogene. In addition, they suggested that a second stage of deformation in the Eastern Cordillera initiated during the late Paleogene, and the main uplift of the Eastern Cordillera resulted from Miocene-Pliocene thrusting. The current structural configuration of the La Cira-Infantas oil field is directly associated with at least two phases of Tertiary deformation of the Middle Magdalena Valley Basin. The uplift of the Central Cordillera, also called pre-Andean orogeny (Villamil, 1999), developed strongly compressive dip-slip structures, where Jurassic, Cretaceous, and probably lower Tertiary deposits were folded, faulted, and eroded during the Middle Eocene (Taborda, 1965) (Figures 2.28 and 2.29).

The unconformity generated by this regional Tertiary tectonic event has a clear angular expression in the seismic profiles along the northern MMVB (Suarez, 1997) and in the La Cira-Infantas structure (Figures 2.5, 2.6, and 2.14). This Eocene deformation

period generated a series of compressional structures, including the main antiform and secondary features (thrusts and minor folds) identified below the Eocene unconformity in the La Cira-Infantas area.

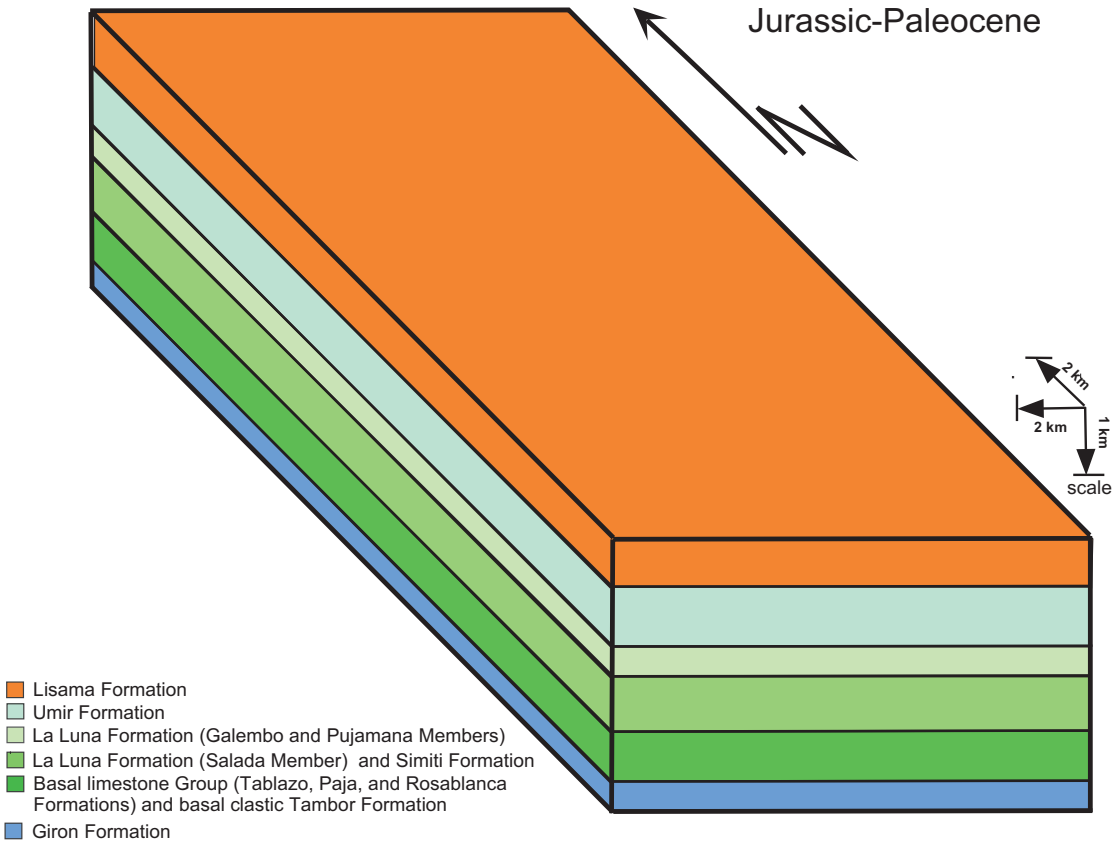

Figure 2.28: Block diagram across the La Cira-Infantas area during the Mesozoic to Early Cenozoic period. The Jurassic Giron Group, a heterogeneous succession of continental red beds and silicic to intermediate volcanics, lies unconformably on the crystalline basement. These rocks filled the Jurassic rift developed in the current position of the MMVB and the Eastern Cordillera. Cretaceous strata were deposited over an evolving continental margin and show a steady accumulation typical of thermal subsidence (Villamil, 1998a). The sandy Tambor Formation indicates the beginning of the Cretaceous deposition during the Valanginian in the MMVB. Marine environments predominate during the Hauterivian to Santonian, controlling the deposition of the overlying Rosablanca, Paja, Tablazo, Simiti, Salto, and La Luna formations. The Umir Formation was deposited during a regressive oscillation of Campanian-Maastrichtian age (Morales et al., 1958). The marine Cretaceous sequences are overlain by a succession of Early Tertiary continental deposits of the Lisama Formation (Paleocene).

A second period of tectonism is responsible for the folding, thrusting, and uplift of the late Paleogene-Neogene sedimentary cover. During this important Miocene-Pliocene

episode, the La Cira and Infantas anticlines were developed, faulted, uplifted, and partially eroded.

The Santa Marta-Bucaramanga fault began its important left-lateral strike-slip activity in the late Miocene generating the inversion and uplifting of the Eastern Cordillera. This regional wrenching tectonics probably induced secondary small-displacement and simple parallel wrench systems, initially developing a single alignment of anticlines arranged in a left-handed en échelon pattern (Figures 2.30 and 2.31). Later, these folds were slightly fractured by coexisting normal and reverse faults (e.g., La Cira fault).

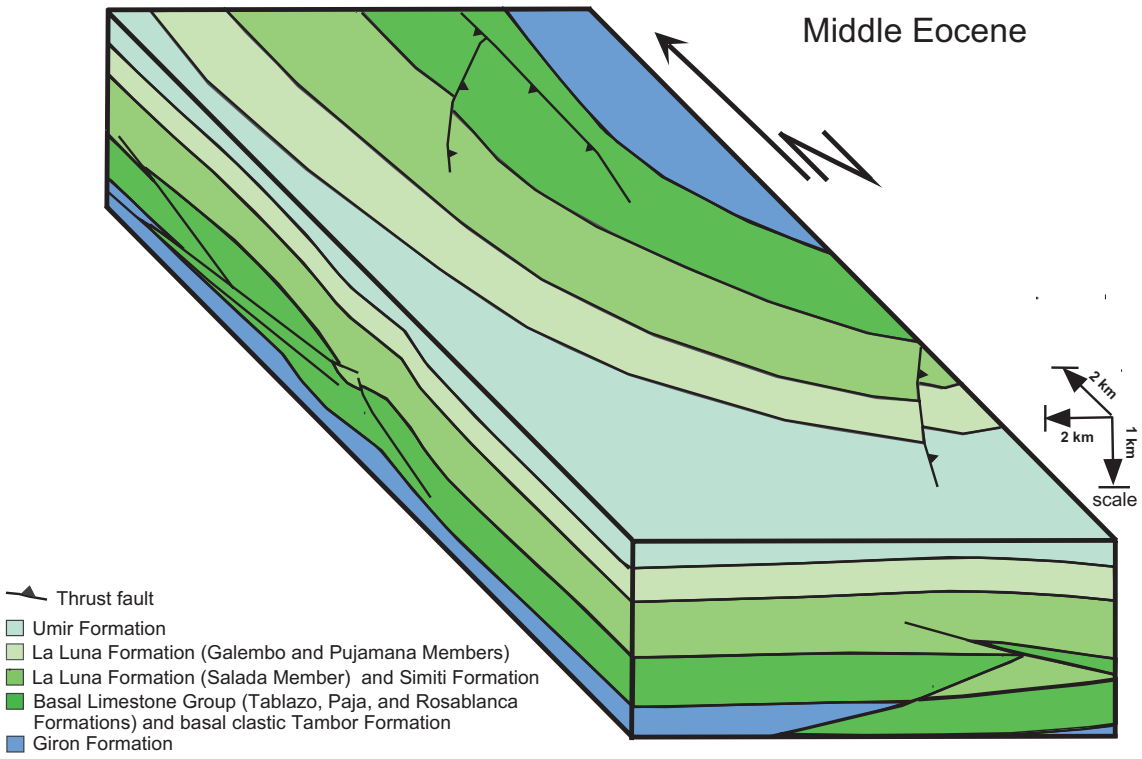

Figure 2.29: Block diagram across the La Cira-Infantas area during the Middle Eocene. The uplift of the Central Cordillera, also called pre-Andean Orogeny (Villamil et al., 1999), developed strongly compressive dip-slip structures, where Jurassic, Cretaceous, and probably lower Tertiary deposits were folded, faulted, and eroded during the Middle Eocene (Taborda, 1965).

More recently, a dominantly dip-slip compressive tectonic event, associated with the regional uplift of the complete Eastern Cordillera in the Pliocene-Pleistocene, accelerated the folding of the La Cira-Infantas structure. Coexisting normal and reverse separation faults simultaneously broke these folds. The regional Infantas thrust system was created

at this time, causing the uplift, faulting, and partial erosion of the eastern flank of the pre-existing Infantas anticline (Figure 2.32). The Infantas system can be interpreted as the westernmost expression of a thrust belt that extends into the MMVB from the Eastern Cordillera.

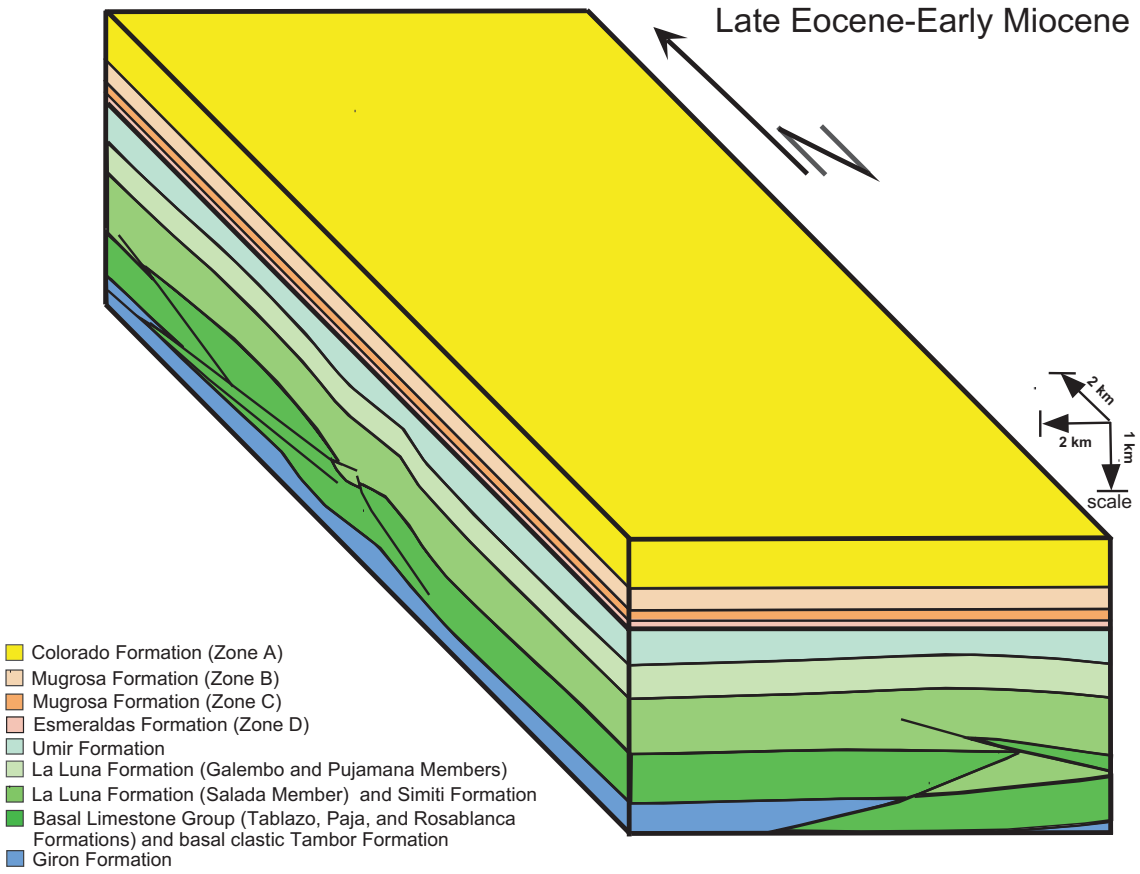

Figure 2.30: Block diagram across the La Cira-Infantas area during the Late Eocene to Early Miocene period. The folded, faulted, and eroded Cretaceous sequence is overlain by a succession of continental deposits. These strata are related to specific tectonic events in the Central and Eastern Cordilleras. The Tertiary stratigraphic column includes the Esmeralda Formation (Eocene), Mugrosa Formation (Oligocene-Lower Miocene), and Colorado Formation (Lower Miocene-Lower Middle Miocene).

Compressive late and early Tertiary structures in the La Cira-Infantas oil field are characterized by a dominant shortening west-east orientation. Similarly, analyses of wellbore-breakout orientations in the MMVB indicate that the maximum compressive principal stress is horizontal and oriented around $N68°W$ (Castillo and Mojica, 1990) and $N76°W$ (World Stress Map, 1999). Therefore, the orientation of the paleo-stress

field during the Tertiary and the present-day trends indicate a relative consistency in the regional stress field orientation during the Cenozoic.

Geological field mapping of oblique normal faults that crosscut and offset compressive structures and Quaternary deposits (Leon, 1991), suggest a possible younger episode of faulting. These observations agree with the seismic mapping of normal faults that slightly crosscut and offset compressive structures in the northern La Cira area. This recent faulting is possibly associated with present day activity of the Palestina, Bucaramanga, and La Salina fault systems (Paris and Romero, 1994).

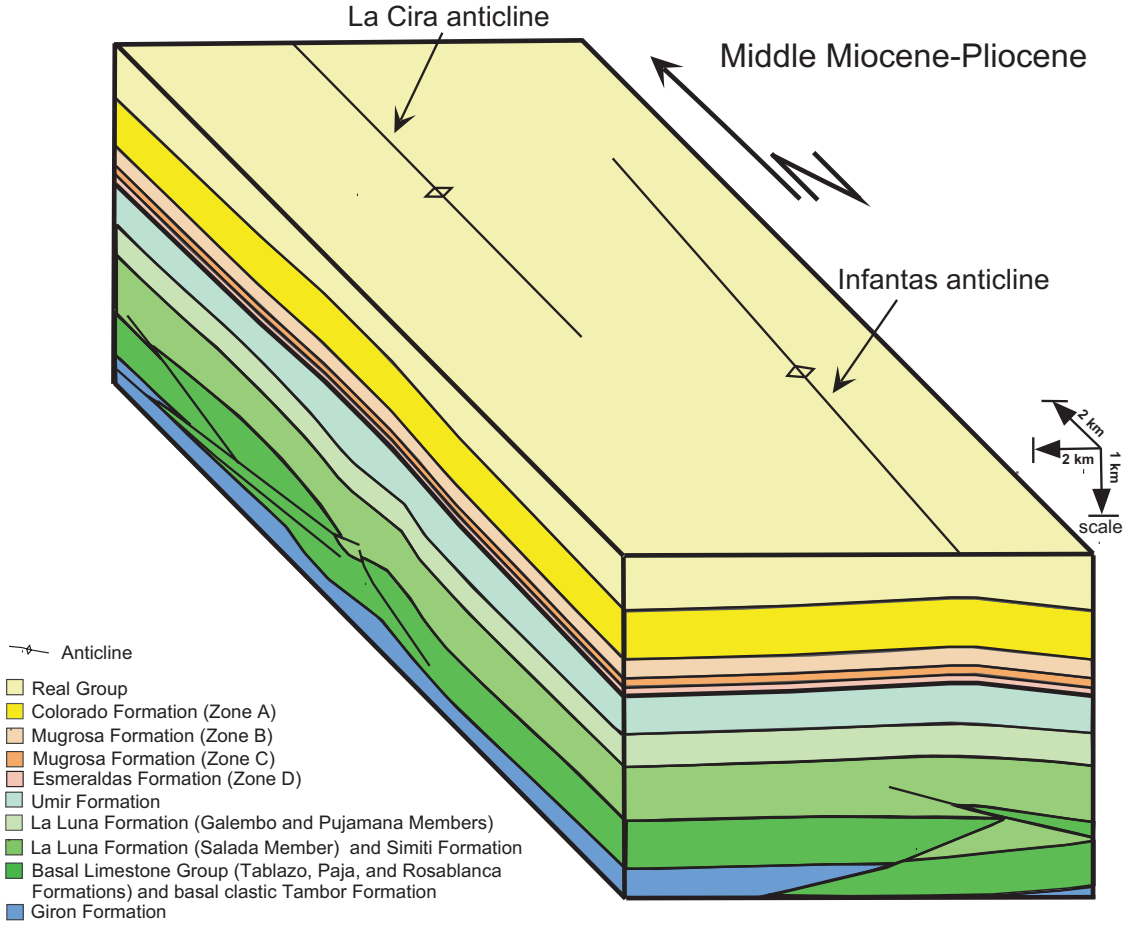

Figure 2.31: Block diagram across the La Cira-Infantas area during the Middle Miocene to Pliocene period. The Santa Marta-Bucaramanga fault began important left-lateral strike-slip activity in the late Miocene, developing the inversion and uplifting of the Eastern Cordillera. This regional wrenching tectonics probably induced secondary small displacement and simple parallel wrench systems, initially generating a single alignment of anticlines arranged in a left-handed en échelon pattern. Later, these folds were slightly fractured by coexisting normal and reverse faults.

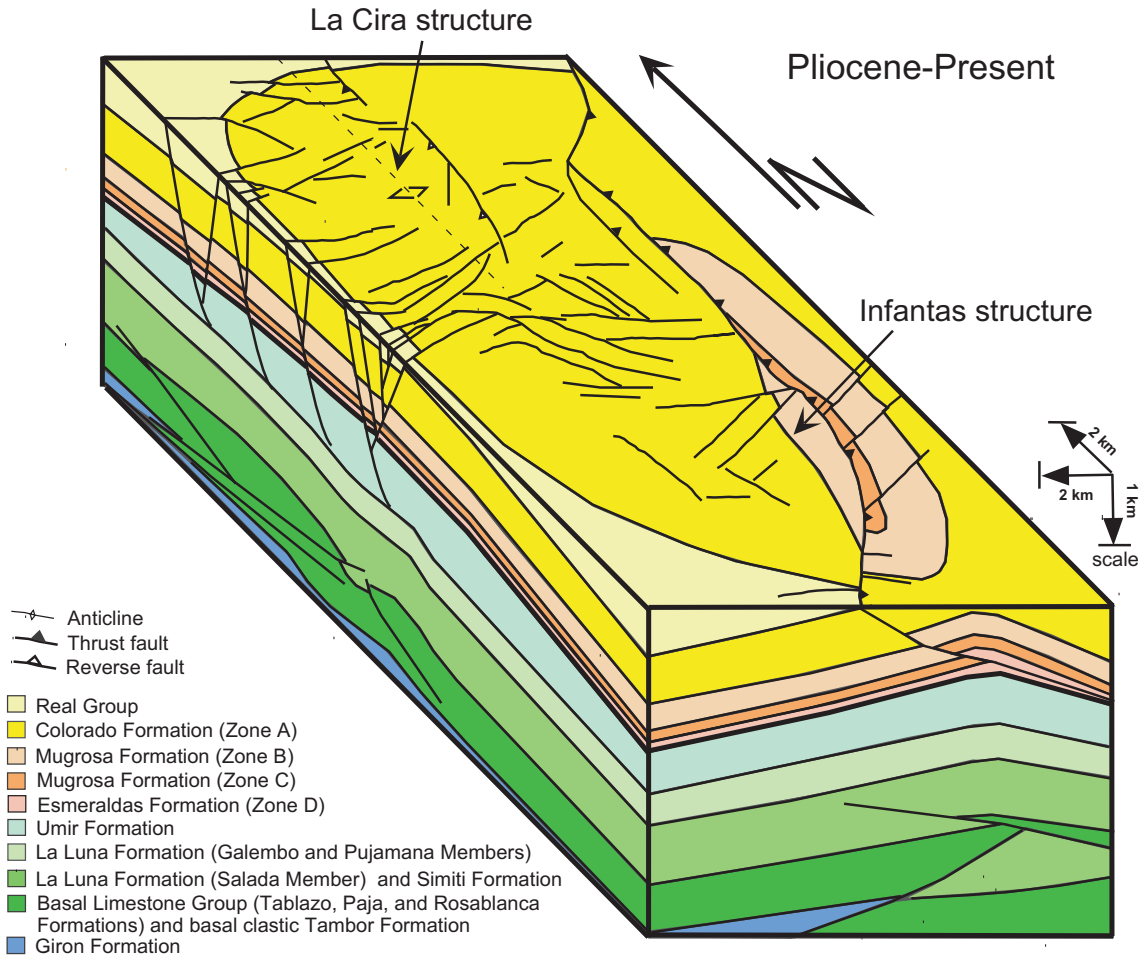

Figure 2.32: Block diagram across the La Cira-Infantas area during the Pliocene to present period. The regional uplift of the complete Eastern Cordillera in the Pliocene-Pleistocene generated a dominant dip-slip compressive tectonic event, accelerating the folding of the La Cira-Infantas structure and the development of coexisting normal and reverse separation faults. The regional Infantas thrust system was developed at this time causing the uplifting, faulting, and partial erosion of the eastern flank of the pre-existing Infantas anticline.

2.7 Conclusions

Based on the interpretation of 3-D seismic data, a conceptual model of the structural heterogeneities (faults and folds) in the La Cira-Infantas oil field was developed. The La Cira-Infantas oil field is comprised of a series of early and late Tertiary structural heterogeneities. The western flank of a large north-south elongated anticline underlies the Tertiary cover, and is highly fractured by thrust faults that generate a series of asymmetric secondary folds.

Late Tertiary structural heterogeneities include the La Cira and Infantas anticlines and three groups of associated faults. The first group includes a set of low-angle reverse faults with east- and west-vergence. They cut the entire Tertiary sedimentary column and glide on a shaly section directly above the Middle-Eocene unconformity. These faults usually strike between north-south to $N30°E$. In addition, there are a significant number of high-angle normal faults, which show oblique and longitudinal patterns. In general, the oblique set strike between $0°$ and $30°$ on either side of the dominant east-west azimuth of the longitudinal set. These normal faults compartmentalize La Cira and Infantas anticlines into a group of reservoir blocks.

The description of the structural heterogeneities using three-dimensional seismic data, based on closely spaced measurements of the fault slip, allows a detailed mapping and analysis of the slip distribution. The mapping of the dip slip along the seismic markers Sands-116 and A-4 suggests that the normal fault FNCN1 in the northern La Cira area, formerly interpreted as a continuous fault plane, consist of at least five overstepping segments. Because the fault segments are approximately elliptical in shape, the slip varies more quickly along the dip orientation than along strike.

This irregular slip distribution along the main fault surfaces may affect the hydraulic behavior of the faults, generating fluid flow anomalies and the resulting production problems in the La Cira-Infantas oil field. Therefore, integrating the slip analysis into the reservoir studies is vital to effectively characterize flow paths, fault sealing potential, and reservoir compartmentalization.

Folding, thrusting, and normal faulting of Paleogene and Neogene sediments in the La Cira-Infantas oil field are explained with a simple parallel and small displacement wrench zone, which was developed during the Late Miocene-Pliocene. Some faults show offsetting relations that suggest a possible younger stage of faulting, possibly related to present-day activity of the major fault systems in the basin.

2.8 Acknowledgments

The Stanford Rockphysics and Borehole Geophysics project (SRB) and Ecopetrol supported this work. I would like to thank Ecopetrol for providing the data. Thanks to Professor Atilla Aydin and Professor David Pollard for useful comments and discussion.

2.9 References

Barnett, J. A. M., J. H., Rippon, J. J. Walsh, and J. Watterson, 1987, Displacement geometry in the volume containing a single normal fault: AAPG Bulletin, **71,** p. 925-937.

Biddle, K. T., and N. Christie-Blick, 1985, Glossary-strike slip deformation, basin formation, and sedimentation, in K. T. Biddle and N. Christie-Blick, Eds., Strike-slip deformation , basin formation and sedimentation: SEPM, no. 37, p. 375-386.

Burgmann, R., and D. Pollard, 1994, Slip distribution on faults: Effects of stress gradients, inelastic deformation, heterogeneous host-rock stiffens, and fault interaction: Journal of Structural Geology, **16,** 1675-1690.

Castillo, J. E., and J. Mojica, 1990, Determinacion de la orientacion de esfuerzos actuales a partir de deformaciones tectonicas ("breakouts") en algunos pozos petroleros de los Llanos Orientales y del Valle Medio del Magdalena, Colombia: Geologia Colombiana, no. 17, p. 123-132.

Campbell, C. J., 1968, The Santa Marta wrench fault of Colombia and its regional setting, in Saunders, J. B., Ed., Transactions of the Fourth Caribbean Geological Conference, Port of Spain, p. 247-261.

Cooper, M. A., F. T. Addison, R. Alvarez, M. Coral, R. H. Graham, A. B. Hayward, S. Howe, J. Martinez, J. Naar, R. Penas, A. J. Pulham, and A. Taborda, 1995, Basin development and tectonic history of the Llanos Basin, Eastern Cordillera and Middle Magdalena Valley, Colombia: American Association of Petroleum Geologists Bulletin, **79,** no. 10, p. 1421-1443.

Christie-Blick, N., and K. T. Biddle, 1985, Deformation and basin formation along strike-slip faults, in K. T. Biddle and N. Christie-Blick, Eds., Strike-slip deformation, basin formation and sedimentation: SEPM, no. 37, p. 1-34.

Dengo, C. A., and M. C. Covey, 1993, Structure of the Eastern Cordillera of Colombia: Implications for trap styles and regional tectonics: American Association of Petroleum Geologists Bulletin, **77,** no. 8, p. 1315-1337.

Dickey, P., 1992, La Cira-Infantas Field, Middle Magdalena Basin, in E. A. Beaumont and N. H. Foster, Eds., Structural Traps VII, AAPG Treatise of Petroleum Geology, Atlas for Oil and Gas Field, p. 323-347.

Ecopetrol, 2000, http://www.ecopetrol.com.co/ecop/

Etayo, F., 1983, Mapa de terrenos geologicos de Colombia: Ingeominas, Publicacion Especial, Bogota (Colombia), no. 14-1, 235 p.

Etayo, F., 1985, The stratigraphic tectonic framework of the Colombian Andes: Symposium on geology of the Andes and its relation to hydrocarbon and mineral resources, Santiago-Chile, November 11-15.

Geotec, 1988, Mapa Geologico de Colombia, Bogota, Escala 1:1,200,000.

Gómez, E., 1997, Quantified Cenozoic evolution of the Middle Magdalena Valley Basin (Colombia): Ages, paleogeography, tectonics: American Association of Petroleum Geologists Bulletin, **81,** no. 10, p. 1774.

Gómez, E., and T. Jordan, 1998a, Relative timing of Cenozoic deformation of the Middle Magdalena Valley Basin and bounding mountain ranges, Colombia: AAPG/SEPM Annual Meeting Abstracts with Programs, May 17-20, 1998b, Salt Lake City, Utah.

Gómez, E., T. Jordan, S. Kelly, and E. Baquero, 1998, Building a constrained tecto-sedimentologic model of continental sedimentation: Evolving Tertiary paleogeography of the Middle Magdalena Valley Basin, Colombia. Geological Society of America Annual Meeting, Abstracts with Programs, October 22-26, 1998, Toronto, Canada.

Gómez, E., T. Jordan, S. Kelley, and M. Heizler, 1999a, Late Cretaceous and Cenozoic Basin Architecture of the Southernmost Middle Magdalena Valley, Colombia, multiple constraints on syndeformational sedimentation: AAPG/SEPM 1999 Annual Meeting, Abstracts with Programs, April 11-14, San Antonio, Texas.

Gómez, E., T. Jordan, K. Hegarty, and S. Kelley, 1999b, Diachronous deformation of the Central and Eastern Andean Cordilleras of Colombia and Syntectonic Sedimentation in the Middle Magdalena Valley Basin of Colombia. Fourth International Symposium

on Andean Geodynamics, Gottingen, Germany, October 4-6, 1999, Colloques et Seminaires Series, Georg August Universitat Gottingen, Institut de Recherche por le Developpement (IRD-ORSTOM).

Gómez, E., T. Jordan, R. Allmendinger, K. Hegarty, and S. Kelley, 2000, Unconformity-forming processes and syntectonic stratal geometries in actively deforming basins: Late Cretaceous to Cenozoic history of the Middle Magdalena Valley Basin and adjacent Andean Ranges of Colombia: AAPG/AVS Hedberg Research Conference, February 20-23, 2000, Caraballeda, Venezuela.

Gutierrez, M., 1996, Evaluation integral de yacimientos campos La Cira e Infantas: Reporte final interpretacion estructural basica del volumen 3D, Ecopetrol, Technical report, 14 p.

Harding, T. P., 1974, Petroleum traps associated with wrench faults: AAPG Bulletin, **58,** no. 7, p. 1290-1304.

Harding, T. P. and J. D. Lowell, 1979, Structural styles, their plate-tectonics habitats, and hydrocarbons traps in petroleum provinces, AAPG Bulletin, **63,** no. 7, p. 1016-1058.

Harding, T. P., 1990, Identification of wrench faults using subsurface structural data: Criteria and pitfalls: AAPG Bulletin,**74**, no. 10, p. 1590-1609.

ICP-ECP, 1996, Estratigrafia del Terciario del Valle Medio del Magdalena, caracterizacion estratigrafica y prospectividad: Ecopetrol, Technical report, 45 p.

Ingeominas, 1966, Mapa geologico del cuadrangulo I-11 “Cimitarra”, Escala 1:200.000.

Ingeominas, 1967, Mapa geologico del cuadrangulo H-11 “Barrancabermeja”, Escala 1:200.000.

Ingeominas, 1976, Mapa geologico de Colombia. Escala 1:1,500.000.

Irving, E. M., 1971, La evolucion estructural de los Andes mas septentrionales de Colombia: Boletin geologico, Ingeominas, 19, no. 2, p. 1-90.

Kellogg, J., 1984, Cenozoic tectonic history of the Sierra de Perija, Venezuela-Colombia, and adjacent basin, in W. E. Bonini, R. B. Hargraves, and R. Shagam, Eds., The Caribbean-South American plate boundary and regional tectonics: The Geological Society of America, Memoir 162, p. 239-261.

Laverde, F., 1996, Estratigrafia de alta resolucion de la seccion corazonada en el campo La Cira: Ecopetrol, Technical report, 37 p.

Leon, A., 1991, Mapa geologico del departamento de Santander: Bol. Geologia, Bucaramanga, Colombia, **20**, no. 35, p. 53-63.

Lowell, J., 1985, Structural styles in petroleum exploration: OGCI Publications, Oil & Gas Consultants International Inc, Tulsa, 460 p.

Mann, P., M. R. Hempton, D. Bradley D., and K. Burke, 1983, Development of pull-apart basins: Journal of Structural Geology, **91,** p. 529-554.

Maerten, L., E. Willemse, D. Pollard, and K. Rawnsley, 1999, Slip distribution on intersecting normal faults: Journal of Structural Geology, **21,** p. 259-271.

Mesa, A., 1995, Diagenesis y calidad del reservorio del campo La Cira: Ecopetrol, technical report, 44 p.

Mojica, J. and R. Franco, 1990, Estructura y evolucion tectonica del Valle Medio y Superior del Magdalena, Colombia: Geologia Colombiana, no. 17, p. 41-64.

Montgomery, S., 1992, Petroleum potential of Upper and Middle Magdalena Basins, Colombia, Part 1: Local and regional geology: Petroleum Frontiers, **9**, no. 2, 58 p.

Mora, C., F. Cordoba, O. Luna, L. F. Sarmiento, A. Rangel, B. Giraldo, H. Bartels, J. P. Reyes, L. B. Magoon, 1996, Petroleum Systems of the Middle Magdalena Valley, Colombia: AAPG Bulletin, **80,** no. 8, p. 1316.

Morales, L. G., D. J. Podesta, W. C. Hatfield, H.Tanner, S. H. Jones, M. H. Barker, D. J. O'Donoghue, C. E. Mohler, E. P. Dubois, C. Jacobs, and C. R. Goss, 1958, General geology and oil occurrences of the Middle Magdalena Valley, Colombia: Habitat of Oil Symposium, American Association of Petroleum Geologists, p. 641-695.

Olaya, I.D., 1997, Seismic stratigraphic characterization of the Lower Tertiary in the Cachira Paleohigh, Middle Magdalena Basin, Colombia: M..S. Thesis, CSM, Geology, Golden, Colorado, 100 p.

Paris, G. and J. Romero, 1994, Fallas activas en Colombia: Boletin Geologico, Ingeominas, **34,** no. 2-3, p. 1-53.

Pindell, J. L. 1985, Alleghenian reconstruction and subsequent evolution of the Gulf of Mexico, Bahamas, and the proto-Caribbean: Tectonics, **4,** p. 1-39.

Pindell, J. L., R. Higgs, and J. Dewey, 1998, Cenozoic palinspastic reconstruction, paleogeographic evolution and hydrocarbon setting of the northern margin of South

America in J. L. Pindell and C. Drake Eds., Paleogeographic evolution and non-glacial eustasy, Northern South America, SEPM Special Publication no. 58, p. 45-85.

Ramon, J.C., 1998, Sequence stratigraphic framework of Tertiary strata and oil geochemical evaluation, Middle Magdalena Basin, Colombia: Ph.D. Thesis, CSM, Geology, Golden, Colorado, 297 p.

Restrepo-Pace, P. A., K. H. James, and T. Villamil, 1999a, Fold and thrust belt hydrocarbon plays along the eastern margin of the Middle Magdalena Valley, Colombia: AAPG Bulletin, **83,** No. 8, p. 1336.

Restrepo-Pace, P. A., F. Colmenares, C. Higuera, and M. Mayorga, 1999b, Fold and thrust belt along the western flank of the Eastern Cordillera of Colombia: style, kinematics and timing constrains derived from seismic data and detailed surface mapping: AAPG Bulletin, **83,** No. 8, p. 1336.

Rippon, J. H., 1985, Contoured patterns of the throw and hade of normal faults in Coal Measures (Westphalian) of north-east Derbyshire: Proceeding of the Yorkshire Geological Society, **45**, part 3, p. 147-161

Schamel, S., 1991, Middle and Upper Magdalena Basins, Colombia, in K. T. Biddle, editor, Active margin basins, American Association of Petroleum Geologists, AAPG Memoir 52, p. 283-301.

Suarez, M. A., 1997, Facies analysis of Eocene La Paz formation, and regional evaluation of the post-middle Eocene stratigraphy, Northern Middle Magdalena Valley, Colombia: M.S. thesis, University of Colorado, Boulder, Colorado, 88 p.

Taborda, B., 1965, The Geology of the De Mares Concession: Geological field trips, Colombia, 1958-1978: Colombian Society of Petroleum Geologists and Geophysicists, p. 119-159.

Tearpock, D. and R. Bischke, 1991, Applied subsurface geological mapping: Englewood Cliff, NJ, Prentice Hall Inc, 648 p.

Tyler, N. and R. Finley, 1991, Architectural controls on the recovery of hydrocarbons from sandstone reservoirs, in A. D. Miall and N. Tyler, Eds., The three-dimensional facies architecture of terrigenous clastic sediments and its implications for hydrocarbon discovery and recovery: SEPM, Concepts in Sedimentology and Paleontology, **3**, p. 1-5.

Villamil, T., 1998a, A new sequence stratigraphic model for basinal cretaceous facies of Colombia, in Pindell J. L. and C. Drake Eds. Paleogeographic Evolution and Non-glacial Eustasy, Northern South America, SEPM Special Publication no. 58, p. 161-216.

Villamil, T., 1998b, Mezosoic paleogeographic evolution of Northern South America: Foundations for sequence stratigraphic studies in passive margin strata deposited during non-glacial times, in Pindell J. L. and C. Drake, Eds., Paleogeographic Evolution and Non-glacial Eustasy, Northern South America, SEPM Special Publication, no. 58, p. 283-318.

Villamil, T., P. Restrepo-Pace, and K. Svela, 1999, Campanian-Oligocene evolution and tectonostratigraphic development of Northwestern South America: AAPG Bulletin v**. 83,** no. 8, p. 1344.

Walsh, J. J., and J. Watterson, 1991, Geometric and kinematic coherence and scale effect in normal fault systems, in Roberts, A. M., G. Yielding, and B. Freeman, Eds., The geometry of normal faults, Special publication of the geological society, London, **56**, p. 193-203.

Wilcox, R. E., T. P. Harding, and D. R. Seely, 1973, Basic wrench tectonics: AAPG Bulletin, **57**, no. 1, p. 74-96.

Willemse, E., D. Pollard, and A. Aydin, 1996, Three-dimensional analyses of slip distributions on normal faults arrays with consequences for fault scaling: Journal of Structural Geology, **18**, 295-309.

Willemse, E. and D. Pollard, In press, Normal fault growth: Evolution of tipline shapes and slip distribution.

World Stress Map, 1999, Data from the database of the World Stress Map project

Chapter 3

Stratigraphy-Guided Rock Physics and Seismic Reservoir Characterization

3.1 Abstract

The success of secondary and tertiary hydrocarbon recovery hinges on reliable modeling of reservoir physical properties, most important of which are porosity, permeability, and hydrocarbon saturation. Reservoir heterogeneities prevent efficient drainage and sweep of hydrocarbons. The most efficient way of obtaining a 3-D description of the subsurface heterogeneity is through seismic surveys. Seismic data, in principle, can be converted into a volume of the reservoir's elastic properties such as acoustic and elastic impedance. The challenge remains to relate these elastic properties to porosity, lithology, and hydrocarbon saturation. Rock physics provides this link.

The needed relations between acoustic and elastic impedance and reservoir properties can be determined from well log and core data where the rock characteristics are measured simultaneously on the same rock sample. This study found that if subsets of log and core data are used that are constrained by a sequence stratigraphy framework, meaningful rock physics relations can be determined. These relations can be rationalized and explained by effective-medium models. The key to obtaining such models is consistency between the reservoir's sedimentological characteristics (e.g., texture and composition), well log data (e.g., GR), and core analysis (e.g., porosity and velocity). This concept was applied to map highly heterogeneous reservoir properties in Tertiary fluvial sandstones in the mature giant La Cira-Infantas oil field (Middle Magdalena Valley Basin, Colombia).

By analyzing well logs and core data, a governing effective-medium-based rock physics model was determined. The model implies that velocity and acoustic impedance

are reliable reservoir quality discriminators. Specifically, high velocity and acoustic impedance correspond to shales whereas low velocity and acoustic impedance indicate high-quality sands. The model also allows for fluid prediction from a combination of P- and S-wave data.

Rock-physics-and-stratigraphy-based interpretation of seismic data appears to be a promising approach for the detection of depleted, bypassed, and untapped reservoirs and deeper pools in mature fields such as La Cira-Infantas.

3.2 Introduction

3.2.1 Research Motivation

Depositional and diagenetic heterogeneities compartmentalize fluvial reservoirs into flow units of variable lateral and horizontal extent. These heterogeneities prevent efficient drainage and sweep of reservoirs and are frequently bound up with the facies architecture inherited from the original depositional system. These reservoir heterogeneities are among the principal causes of the very low recovery in numerous gas and oil fields around the world.

Tyler and Finley (1991) found a clear relationship between reservoir's architecture and conventional recovery efficiency by evaluating 450 major Texas reservoirs. They concluded that in a variety of depositional settings, the dominant factor that controls recovery efficiency is reservoir genesis, which includes depositional processes and diagenetic history. To date, there has been little work on developing specific techniques for reservoir characterization in fluvial sedimentary settings, based on rock physics analysis and 3-D seismology; moreover, much of the work done in seismic stratigraphy, particularly in marine sedimentary environments, has focused on use of 2-D seismic data.

The problem of recovery efficiency in heterogeneous reservoirs is of general significance because ancient fluvial oil deposits have considerable economic importance worldwide (Miall, 1996). Traditional seismic reservoir characterization puts emphasis on finding the geological meaning of reflection data and/or mathematical attributes thereof (e.g., seismic amplitude) (Sheriff, 1992; Hardage et al., 1994; Weimer and Davis, 1996; Brown, 1999). Geostatistics is often used to relate such attributes to reservoir physical

properties (Doyen, 1988; Hirsche et al., 1997). However, these techniques are often unable to deliver an accurate reservoir property description because they do not take advantage of deterministic physical links between seismic and reservoir properties.

In order to determine consistent relationships among type of deposits, flow units, rock properties, and petrophysical properties, a rock physics and seismic characterization of reservoir heterogeneities is documented in this chapter. Described here is a rock physics model for relating the elastic reservoir properties to porosity, mineralogy, pore fluid, and differential pressure, with the stratigraphic framework used as a constraint to select the relevant data subsets. The purpose of this model is to: (a) generalize the relations observed in well log and core data, (b) find the ranges of applicability of these relations, and (c) separate the effects of porosity from those of pore fluid on seismic properties. Finally, a new methodology is defined for seismic mapping of the internal architecture of fluvial sandstone reservoirs and the spatial distributions of petrophysical properties and their flow units, that combines core and well-log rock physics analysis with the stratigraphic interpretation of 3-D surface seismic.

3.2.2 La Cira-Infantas Oil Field Reservoirs

La Cira-Infantas (LCI) was the first oil field discovered in Colombia (1918). The estimated original oil in place is 3,700 million barrels (MMBO). After 80 years of exploitation and drilling of 1703 wells, the cumulative production has only reached 720 MMBO. One of the major causes for this low (19%) recovery is the high spatial heterogeneity of the LCI fluvial environment. La Cira-Infantas is located in the central section of the Middle Magdalena Valley Basin (MMVB) (Chapter 2, Figure 2.2). Although oil reservoirs discovered in the MMVB include a sequence of marine and non-marine Middle Cretaceous to fluvial Tertiary rocks, hydrocarbons have been commercially produced from Tertiary siliciclastic reservoirs (Chapter 2, Figure 2.3).

The siliciclastic reservoirs in LCI belong to the Colorado Formation (Zone A) and Mugrosa Formation (Zones B and C) (Figure 3.1). Oil production comes from loosely consolidated Tertiary sands of a highly faulted asymmetrical anticline. The reservoir rocks are fine to medium grained, subarkosic, clean-to-shaly sandstones (Mesa, 1995).

Average porosity is 21% in Zone A, 20% in Zone B, and 23% in Zone C. Permeability may reach 1500 mD. It is highly variable laterally and vertically (Dickey, 1992).

Recent sequence stratigraphy analysis (Laverde, 1996; ICP-ECP, 1996) indicates that the depositional facies of La Cira-Infantas Tertiary rocks are associated with fluvial channel systems. Zones A and B represent mixed load channels or meandering systems, in contrast with Zone C, which was deposited as bed load channels or braided stream systems.

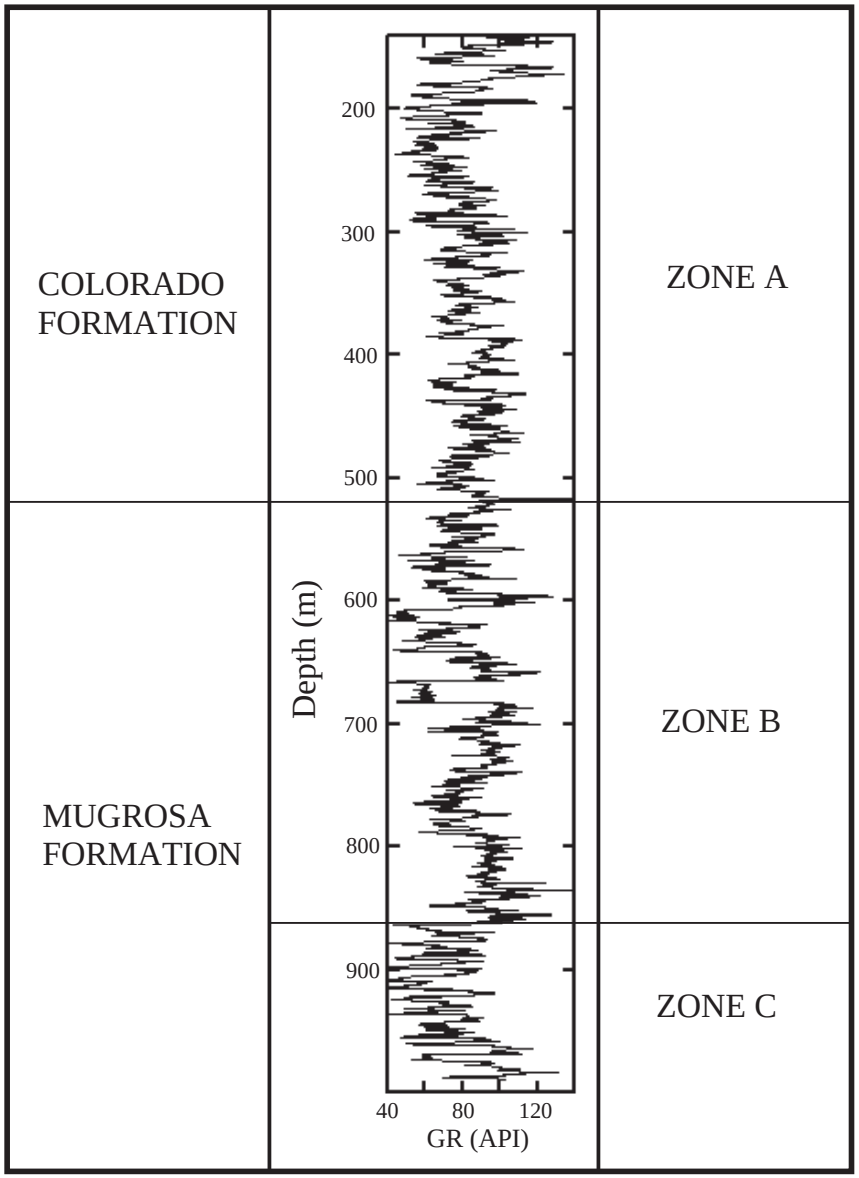

Figure 3.1: Tertiary stratigraphy and reservoir zones, La Cira-Infantas oil field.

Based on the concepts and models of Dickinson (1985), the tectonic setting that best fits the composition of the sandstone reservoirs in La Cira-Infantas (Figure 3.2) is a transitional continental block. This setting for the source area is consistent with the basin's position adjacent to the Central Cordillera (Chapter 2, Figure 2.2). This range is characterized by igneous-metamorphic rocks (Proterozoic), batholiths, and stocks (Triassic-Jurassic). This interpretation about sediment provenance during the Oligocene agrees with source area models presented by Gómez et al., (1999) and Villamil (1999).

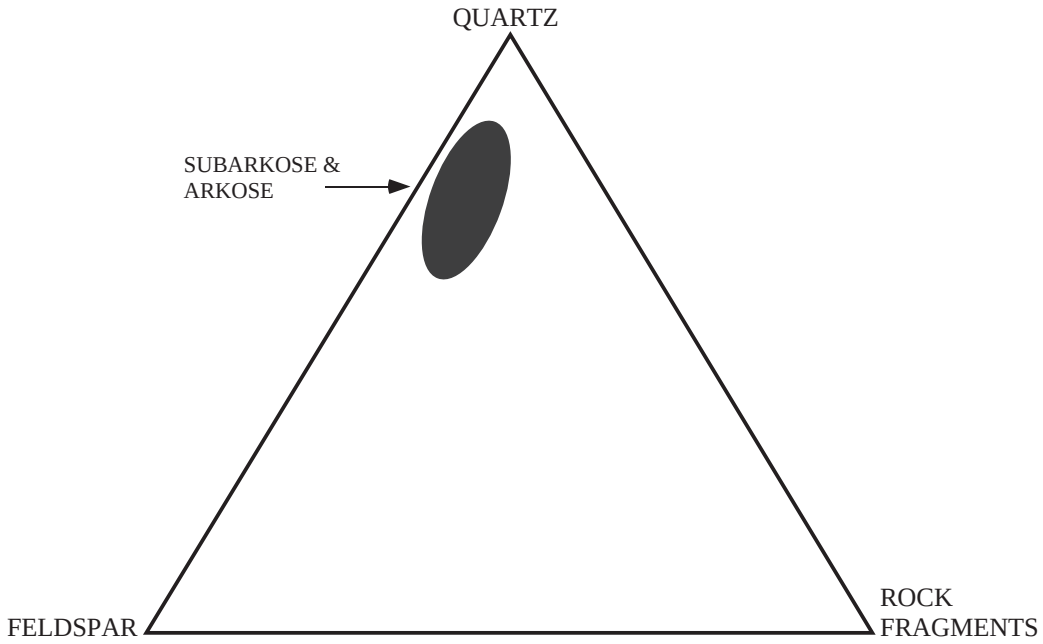

Figure 3.2: Compositional plot of Oligocene and Miocene sandstone reservoirs, La Cira-Infantas oil field (After Mesa, 1995).

3.2.3 Data and Methodology

Using a combination of core and well-log rock physics analysis and the stratigraphic interpretation of 3-D surface-seismic data, this study defines the internal architecture of a Tertiary fluvial sandstone reservoir and proposes a new methodology for seismically mapping spatial distributions of petrophysical properties. This multidisciplinary approach includes the analysis of reservoir heterogeneities at different scales, using rock core, wireline logs, and 3-D seismic data. The data available for this analysis include:

- More than 500 wells with log-based petrophysical analysis.

- Core descriptions: four cored wells.
- Core plugs: 40 measurements of Vp and Vs and 1930 permeability and porosity measurements.
- A petrography study of 230 thin-sections and five SEM analyses.
- Stanford Rockphysics Project database: ultrasonic velocity measurements collected by Han (1987), Yin (1992), and Estes et al. (1994).
- 3-D reflection seismic data, 110 square km, 24 fold. For this study, an area of 20 square km was selected in the northern part of the La Cira-Infantas field; La Cira Norte. The reasons for this selection are (a) the good quality of surface seismic, (b) the simple geologic structure, and (c) the availability of well logs in numerous wells in La Cira Norte.
- One set of dipolar sonic logs (Vp and Vs).
- 15 vertical seismic profiles.

The rock physics and seismic characterization of fluvial reservoirs is divided into two phases. The first phase focuses in the analysis of reservoir heterogeneities at wellbore scale. Heterogeneities at this scale include the pore network (pore and pore throats), grain size and composition, grain packing, lamination and bedding styles, sedimentary structures, lithofacies, and vertical stratification sequences (Slatt and Galloway, 1993).

The main tasks associated with this initial process are summarized as follows:

- Major types of deposits, vertical sequences, and depositional environments are identified from available core. In order to determine reservoir rock quality, different types of deposits, at the whole-core scale, were related to their mineralogical, textural, and pore-level properties and to permeability, porosity, and fluid saturation, as measured on core plugs.
- Petrophysical properties are analyzed, such as changes in texture, cementation, differences in sedimentary structures or bedding styles, and/or separations or prominent shales that may have bearing on fluid distribution and flow, in order to decide what types of deposit, or associations of lithofacies, are possible flow units.
- Several seismic parameters are calculated. The set of parameters include bulk and shear moduli, Vp/Vs ratio, Poisson's ratio, and impedance from P- and S-velocities, and density core and log data.

- Using a sequence-stratigraphy framework as a constraint to select the relevant data subsets, some relations among seismic parameters, and rock and petrophysical properties were generated for each type of deposit. Then, these correlations are compared to empirical relationships.
- Theoretical rock physics relationships are tested and new rock-physics models are generated for this particular set of reservoir rocks.

The second phase includes seismic analysis of the fluvial architectural elements and flow units at interwell scale and a complete 3-D seismic analysis and mapping of the fluvial heterogeneities and their flow units at fieldwide scale. Elements of interwell scale heterogeneity comprise lateral bedding geometries, styles, and continuity; and systematic lateral, and vertical textural patterns (Slatt and Galloway, 1993). Constituents of fieldwide variability include reservoir thickness, facies geometries and continuity, and bulk reservoir properties (Slatt and Galloway, 1993). The process is carried out as follows:

- Seismic inversion techniques are used to convert 3-D seismic surface data into a volume of the reservoir's elastic properties such as acoustic impedance. These elastic properties are related to porosity, lithology, pressure, and hydrocarbon saturation using the new the stratigraphy-constrained rock physics model.
- The new rock physics relations are used to seismically map the internal architecture and the reservoir quality in these Tertiary fluvial sandstones.

3.3 Rock Physics Effects and Reservoir Quality

This section focuses on the analysis of reservoir heterogeneities at wellbore scale. Elements of these kinds of heterogeneities consist of the pore network (pore and pore throats), grain size and composition, grain packing, lamination and bedding styles, sedimentary structures, lithofacies, and vertical stratification sequences (Slatt and Galloway, 1993). The pore geometry is affected by mineralogy (type, abundance, and position), texture (grain size, grain shape, sorting, and packing), detrital fines in intergranular areas, shale laminae, and type of pore-fill cement. The size and shape of the pore network are the results of various geological, physical, and chemical processes, and are generated during the genesis (sedimentation) and/or the geological history of the rock

(tectonic processes, diagenesis, etc.) (Schon, 1996). That is, the characteristics of the pore geometry are controlled by the depositional environment and diagenesis, and define the quality of the reservoir (Barr and Altunbay, 1995).

The most significant properties of reservoir rocks are porosity and permeability, because they control the volume and production of fluids in the reservoir. In other words, they determine the reservoir quality of a rock. Prediction of reservoir rock quality and its spatial distribution are usually one of the principal uncertainties in exploration and development drilling.

Seismic surveys are the most efficient way of obtaining a 3-D description of the subsurface heterogeneity and the reservoir quality at the interwell and field scale. Seismic surface data can be converted into a volume of the reservoir's elastic properties, such as acoustic and elastic impedance. The challenge remains to form a relationship among these elastic properties to porosity, lithology, and hydrocarbon saturation. Rock physics provides this connection.

Rock physics is the link between rock properties and seismic interpretation, and is the fundamental constituent to the quantitative integration of surface seismic data, well logs, and core information (Mavko and Nur, 1996). Elasticity theory provides relations for the velocity of P (V_P) and S (V_S) seismic waves in terms of elastic constants, and the elastic media can be established from velocity and density ρ measurements. For an isotropic, homogeneous, and elastic media,

$$V_P = \sqrt{\frac{\lambda + 2\mu}{\rho}} = \sqrt{\frac{K + \frac{4}{3}\mu}{\rho}}, \text{ and} \tag{3.1}$$

$$V_S = \sqrt{\frac{\mu}{\rho}}, \tag{3.2}$$

$$\frac{V_P}{V_S} = \sqrt{\frac{1-\nu}{0.5-\nu}} \tag{3.3}$$

where λ and μ are the Lamé constants, K is the bulk modulus, and ν is Poisson's ratio. Rocks or materials with high bulk moduli are stiff (that is, they have low

compressibility), and those with high Lamé constant or shear moduli are rigid. A change in lithology usually produces important variations in stiffness and rigidity, and minor changes in density. In addition, a change in the saturation of the fluid modifies the stiffness and density, and commonly does not modify rigidity.

Seismic velocities and density depend on porosity and also on other rock properties such as lithology (clay content, grain size, sorting, structural anisotropy, etc), fluid content, depth, pressure, age, compaction, cementation, and temperature. Seismic velocity depends strongly on porosity, and frequently the increase in velocity with the reduction in porosity is the main factor controlling velocities.

The parameters that control fluid flow are predominantly characteristics of the pore geometry (pore size, shape, etc.) and relationships such as porosity and velocity related to the pore geometry attributes. Although permeabilty is not directly related to velocity or acoustic impedance, these parameters are certainly not completely independent. In fact, porosity and pore shape influence both bulk modulus and permeablity.

Acoustic impedance is a significant rock physics parameter, because the reflection coefficient of normal incident waves is a function of the impedance contrast across the boundary causing the reflection. The acoustic impedance for a P-wave is

$$z = V_p \rho \ , \tag{3.4}$$

and the normal reflectivity is given by the simple expression

$$R = \frac{\rho_2 V_2 - \rho_1 V_1}{\rho_2 V_2 + \rho_1 V_1}, \tag{3.5}$$

where ρ_1 and V_1 are the density and velocity in the incident medium, and ρ_2 and V_2 are those beyond the interface. In other terms, the zero-offset reflection coefficient is expressed as

$$R = \frac{z_2 - z_1}{z_2 + z_1}, \tag{3.6}$$

where z_1 and z_2 are the acoustic impedance values in the layer above and below the reflection boundary, respectively.

3.3.1 Porosity Effect

To determine accurate relationships between porosity and seismic wave velocities is vital, especially when seismic data are applied to predict and map rock properties, such as lithology, porosity, and porosity-related properties (permeability, pore fluids, pore pressure, etc). However, to find these relations is not a trivial task. Mavko and Nur (1996) explain the reason for the difficulty and suggest the following solution: "The effective elastic properties of porous media and the related elastic wave speeds are fundamentally controlled not by porosity, ϕ, but by the *rate of change* of porosity with stress, $R = \partial\phi/\partial\sigma$, which depends on the shape of the pores and their connectivity. Therefore, it is only with specific assumptions or information about the pore space geometry, that special relations between velocity and porosity, itself, can be derived."

Three different approaches have been used to relate the effects of porosity on velocity: empirical relations, bounds, and deterministic models (Mavko et al, 1998). Strictly speaking empirical relations only apply to the specific set of rocks studied and they may fail to predict velocity-porosity relations outside the range of values or rock types for which they are estimated (e.g., Wyllie et al, 1956; Raymer et al, 1980; Han, 1987, etc).

On the other hand, bounds are derived from fundamental principles and can have broad applicability, but they provide the range of velocities that are possible at a given porosity, or vice versa (Mavko and Nur, 1996). For instance, the Hashin-Shtrikman (HS) Bounds (Hashin and Shtrikman, 1963) are upper and lower bounds for predicting the effective moduli given the fractions, *f*, and the bulk, *K*, and shear moduli, □ of each constituent, and can be modified for multiple constituents, and they are termed as

$$K^{HS\pm} = K_1 + \frac{f_2}{(K_2 - K_1)^{-1} + f_1(K_1 + \frac{4}{3}\mu_1)^{-1}}, \tag{3.7}$$

$$\mu^{HS\pm} = \mu_1 + \frac{f_2}{(\mu_2 - \mu_1)^{-1} + \frac{2f_1(K_1 + 2\mu_1)}{5\mu_1(K_1 + \frac{4}{3}\mu_1)}}, \tag{3.8}$$

An adjusted upper HS bound, which takes into account of the critical porosity of the material (Nur et al., 1998; Mavko and Nur, 1996), is characteristic of a stiff cemented rock; in contrast, the lower bound is characteristic of a soft, uncemented sediment.

Core-based Analysis

This section describes the measurements of porosity, permeability, and V_P and V_S in about 40 core plugs from wells LC-1880, LC-1991, and LC-1879. V_P and V_S have been measured at varying confining pressure in air-saturated samples. Velocity measurements at 5 MPa and 10 MPa confining pressure are the focus of this core-based analysis, because they are most similar to the reservoir effective pressure in Zones A, B, and C. The elastic properties of porous sedimentary rocks are essentially controlled by porosity and matrix mineralogical composition. The core measurements from La Cira-Infantas reservoir and non-reservoir rocks show a simple and strong dependence of velocity on porosity (Figures 3.3, 3.4, and 3.5).

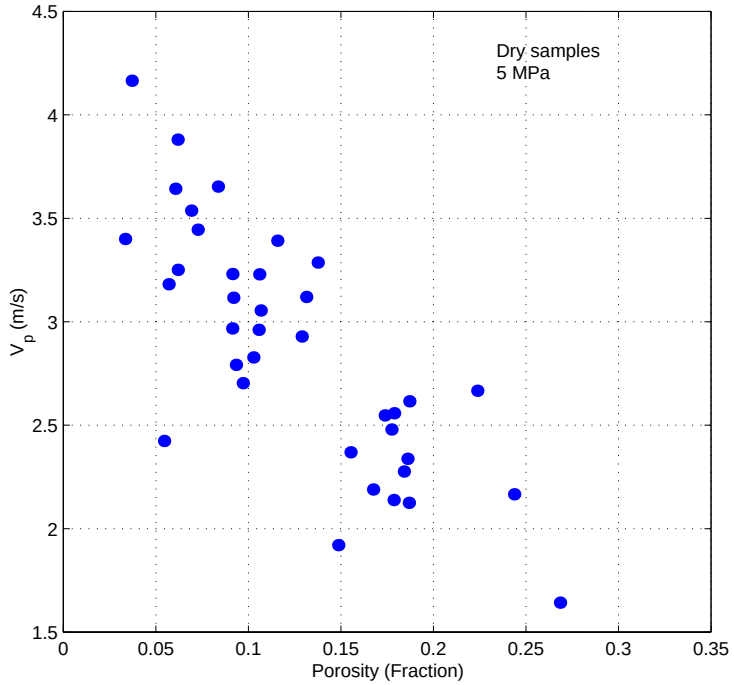

Figure 3.3: Compressional velocity (V_p) versus core porosity.

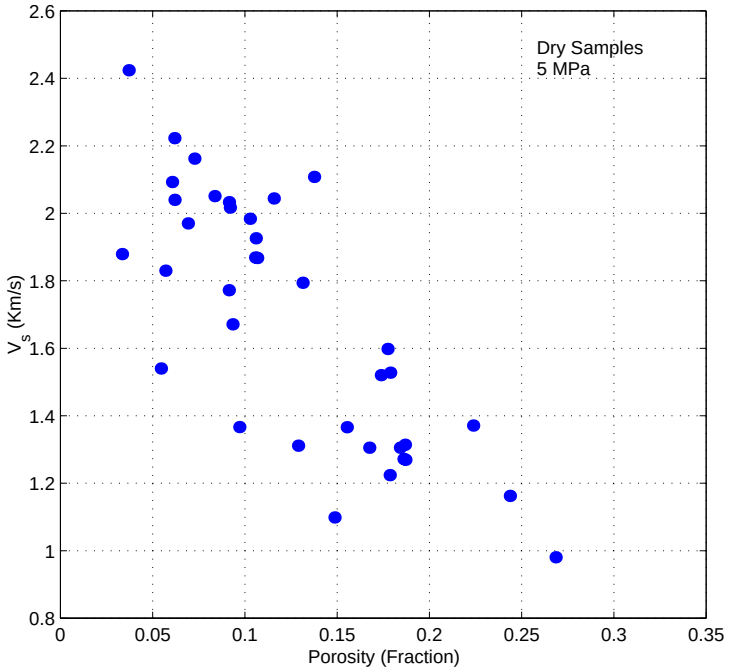

Figure 3.4: Shear velocity (V_s) versus core porosity.

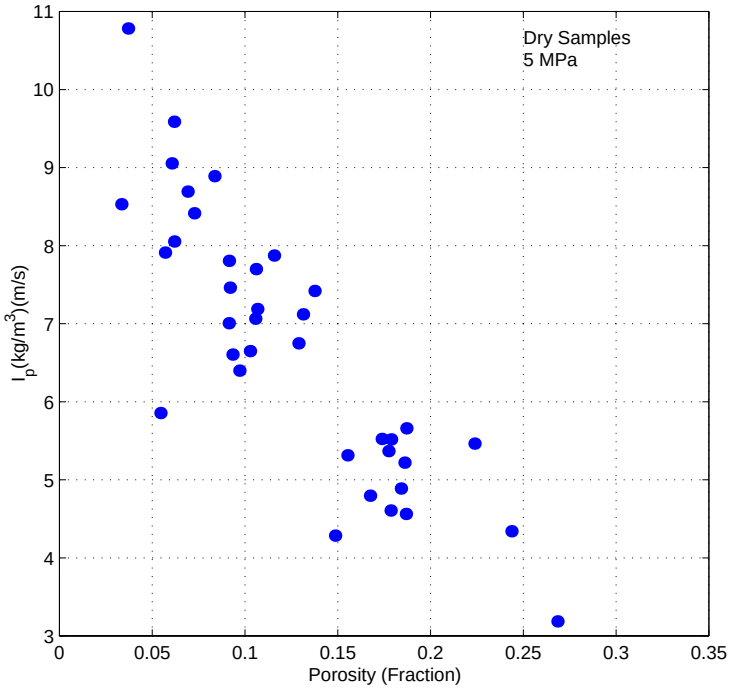

Figure 3.5: Acoustic impedance (I_p) versus core porosity

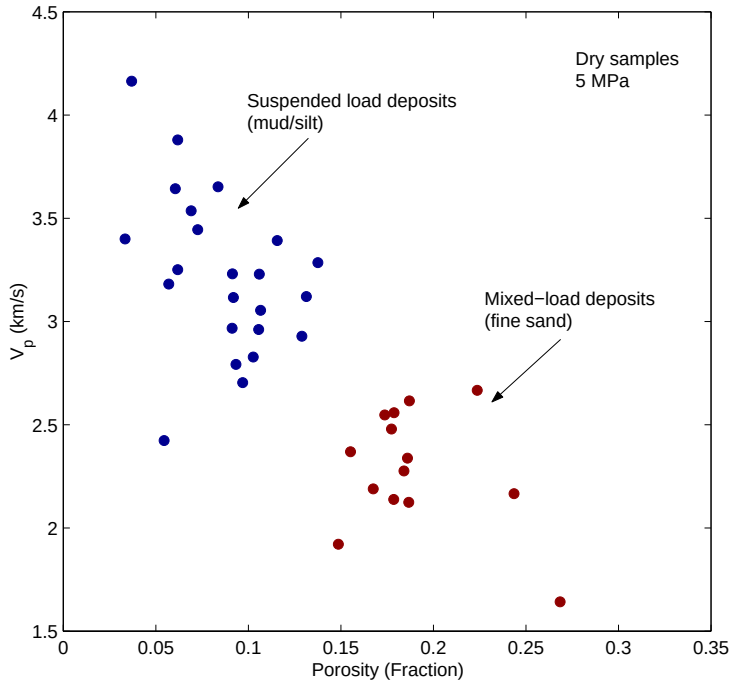

Figure 3.6: Compressional velocity (V_p) versus core porosity. Core samples are separated by grain size.

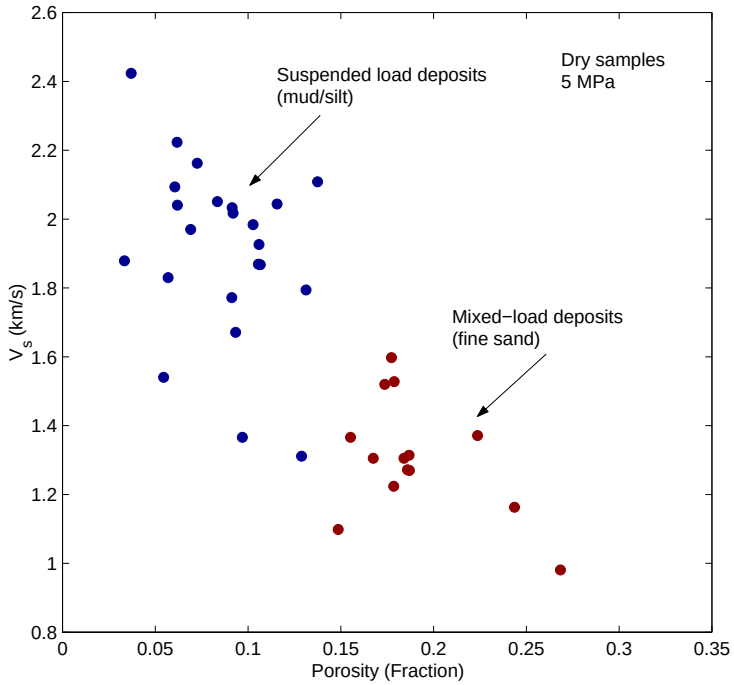

Figure 3.7: Shear velocity (V_s) versus core porosity. Core samples are separated by grain size.

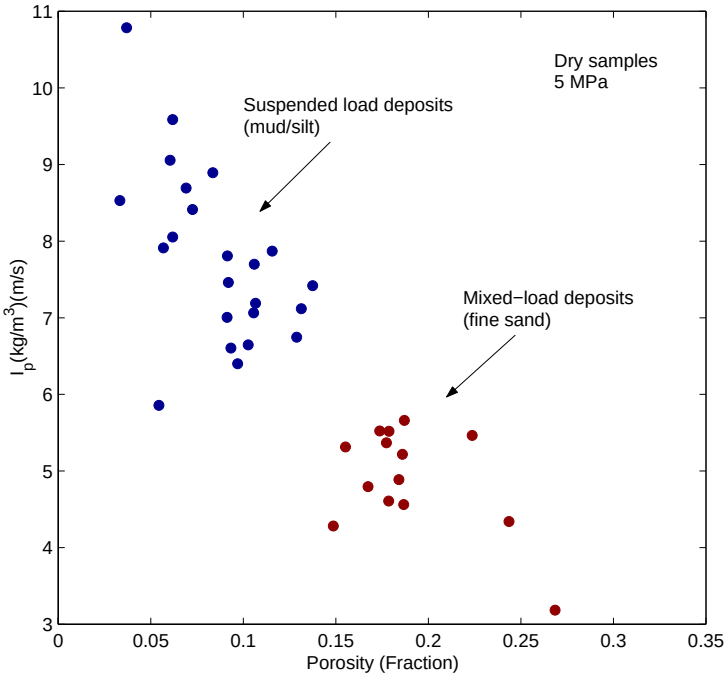

Figure 3.8: Acoustic impedance (I_p) versus core porosity. Core samples are separated by grain size.

These cross-plots also illustrate the important effect of rock texture, particularly grain size, in the rock velocities, acoustic impedance, and porosity. Suspended load deposits (Orton and Reading, 1993), associated with very fine grain rocks, show low porosity and high velocity and impedance. In contrast, mixed-load deposits (Orton and Reading, 1993), associated with fine sands, show high porosity and low velocity and impedance (Figures 3.6, 3.7, and 3.8).

3.3.2 Clay Effect

Han (1987) and Yin et al. (1988) demonstrated the effects of dispersed matrix clay on velocity in synthetic sand-clay mixtures. Later, Marion (1990) modeled these effects, and showed that velocities in sands increase with increasing clay content as long as the sediments are grain-supported. When the clay-volume percentage is less than the porosity, clay is only a component of the pore-filling material, not the matrix; therefore it stiffens the pore component of the material and increases velocity.

Core-based Analysis

Velocity, porosity, and mineralogy were measured in 21 dry samples from La Cira-Infantas (Figure 3.9). The goal was to precisely determine relations between velocity, clay content, and porosity. The core plugs come from shaly zones (non-reservoir rocks). The measurements indicate that the clay content in the shaly intervals is relatively low, thus shaly zones are made up mostly of silt rather than clay.

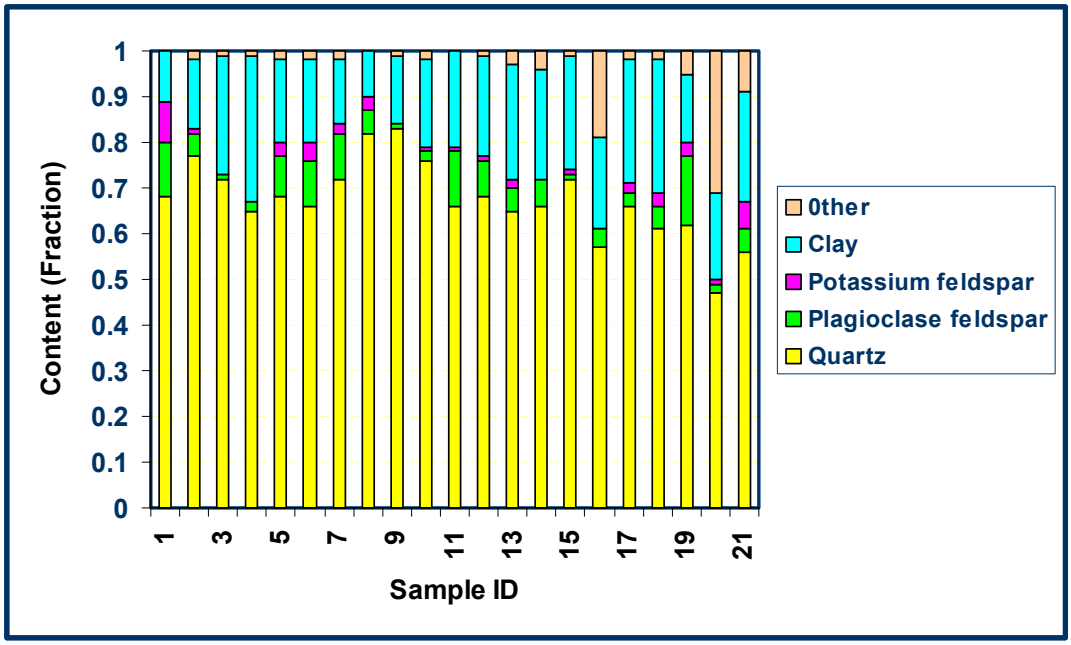

Figure 3.9: Mineralogical composition (x-ray diffraction analysis) of 21 core samples from La Cira–Infantas shaly zones. Other minerals include carbonates, gypsum, barite, and halite. Clay minerals include smectite, illite, chlorite, and kaolinite.

It is not clay content that determines the velocity; but rather the porosity. The shaly zones in La Cira-Infantas apparently do not have very high clay content, but instead have very low porosity. They are generally made out of silt and very fine sand grains.

3.3.3 Texture and Composition Effect

Porosity and permeability are the most important properties of reservoir rocks because they define the reservoir quality of a rock (Bloch, 1994a). Prediction of reservoir

rock quality and its spatial distribution are generally one of the main uncertainties in hydrocarbons exploration and development (Kupecz et al., 1997). The quality of a clastic reservoir can be predicted in diagenetically-simple rocks and can be related to depositional environmentally-restricted parameters, such as rock texture and framework composition (Bloch and McGowen, 1994; Bloch, 1994b) (Figure 3.10).

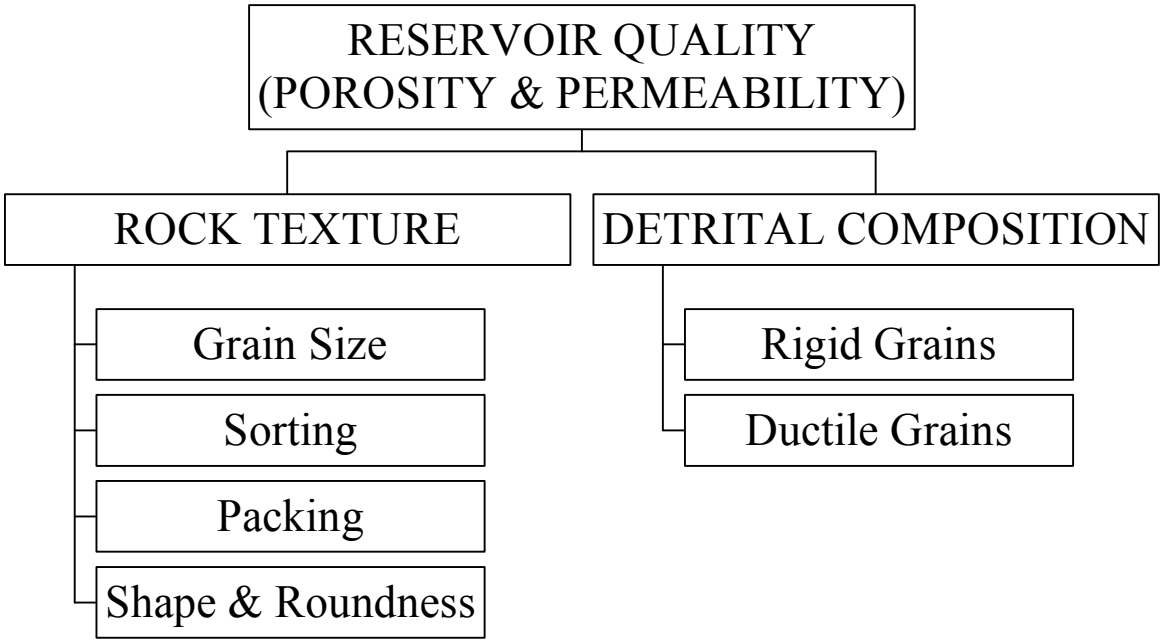

Figure 3.10: Environmentally-restricted parameters that affect the reservoir quality of diagenetically-simple clastic rocks.

The composition, mechanical properties, and relative content of detrital mineral components in clastic rocks affect physical and chemical diagenesis, and therefore the quality of the reservoir rock. Commonly, sandstones with a high content of mechanically-rigid grains exhibit good reservoir quality. For example, highly stable quartz arenites are most likely to preserve high porosities and permeabilities after mechanical compaction. In contrast, a rock with a high content of ductile grains has a framework with low stability; therefore, mechanical compaction by itself can drastically reduce original porosity and permeability (Bloch, 1994b).

Texture includes a group of small-scale geometrical features of the constituent grains, such as size, sorting, packing (spacing of grains), fabric, shape, and rounding (Blatt et al.,

1980). Beard and Weyl (1973), working with unconsolidated sands, studied the effect of texture on porosity and permeability. They particularly investigated the influence of grain size and sorting, because these are the most important textural parameters controlling pore space. Grain size is a basic descriptive characteristic, and grain sorting is a measurement of the variety of grain sizes and the magnitude of the spread of these sizes around the mean size. Generally, sands from dissimilar aqueous environments show a well-documented correlation between sorting and grain size, where fine sands are better sorted than very fine sands or silts (Blatt, et al, 1980). Beard and Weyl (1973), found (1) porosity is basically independent of grain size but strongly controlled by sorting, (2) permeability decreases as grain size becomes finer and as sorting becomes poorer, and (3) low sphericity (grain shape) and high angularity (grain roundness) increase porosity and permeability.

Folk (1951) introduced the important concept of textural maturity to incorporate a variety of textural characteristics. This arrangement of characteristics presents a succession of stages that is the product of kinetic energy input during sedimentation. Folk's textural maturity classification comprises four stages: immature, submature, mature, and supermature (Figure 3.11).

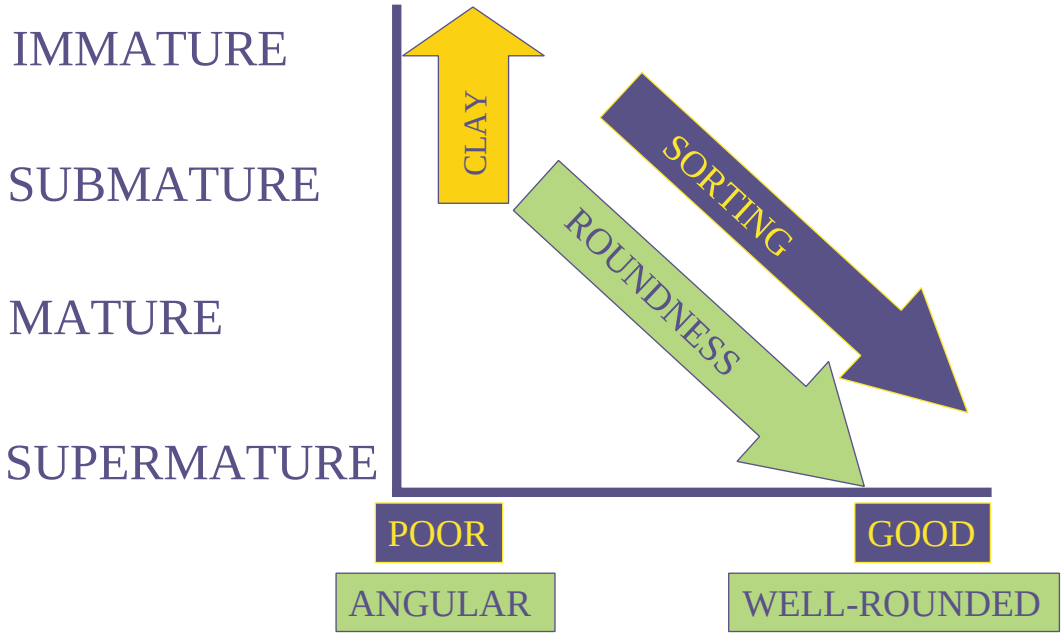

Figure 3.11: Textural maturity classification. Modified from Folk (1951).

Immature sediments contain considerable clay and the grains are poorly sorted and angular. They represent a low energy sedimentary environment that is unable to take apart the constituents of the sediments. Submature sediments have very little to no clay, but the non-clay particles are poorly sorted and angular. Mature sediments contain no clay and are well sorted and angular. Supermature sediments have no clay and are both well sorted and rounded. They represent a very high energy sedimentary environment and high sediment transport rates. Although Folk's classification follows a sequential organization, some rocks indicate a textural inversion. One example is a bimodal grain size mixture, where well-rounded grains are surrounded by a clay-rich matrix, or have well-rounded but poorly sorted grains. Such bimodal mixtures should be considered as the lowest stage of textural maturity.

In clastic rocks with a high content of mechanically rigid grains, bimodality has an important effect on reservoir quality. Clarke (1979) analyzed the effect of grain sorting on reservoir properties and concluded that, in some clastic rocks, reservoir quality is affected more by bimodality than by diagenesis. Taking into account the important effect of sorting in reservoir quality, it is a critical task to establish accurate relations between a reservoir's elastic properties and textural parameters. The main purpose of this section is to suggest experimental and theoretical relations between seismic wave velocities and grain sorting and composition. These relations are essential when seismic or sonic data are used to predict reservoir quality in clastic rocks.

Effect of Sorting on Elastic Velocity–Experimental Data

As previously mentioned, Beard and Weyl (1973), in work with unconsolidated sands, studied the effect of texture on porosity and permeability, however, they did not include acoustic velocity measurements in their extensive analyses. Estes et al. (1994) measured velocity, porosity, and permeability on unconsolidated mixtures of mechanically rigid grains, including natural sands and glass beads. The experiments carried out by Estes et al. are very important, especially the measurements on glass beads, because they illustrate the effect of sorting on velocity and porosity, excluding compositional effects and other textural effects, such grain shape and roundness. Figure 3.12 shows schematically the Estes et al. experiment and their results. In this particular

example, the samples were made by artificially mixing, in various amounts, large size glass beads with much smaller size glass beads.

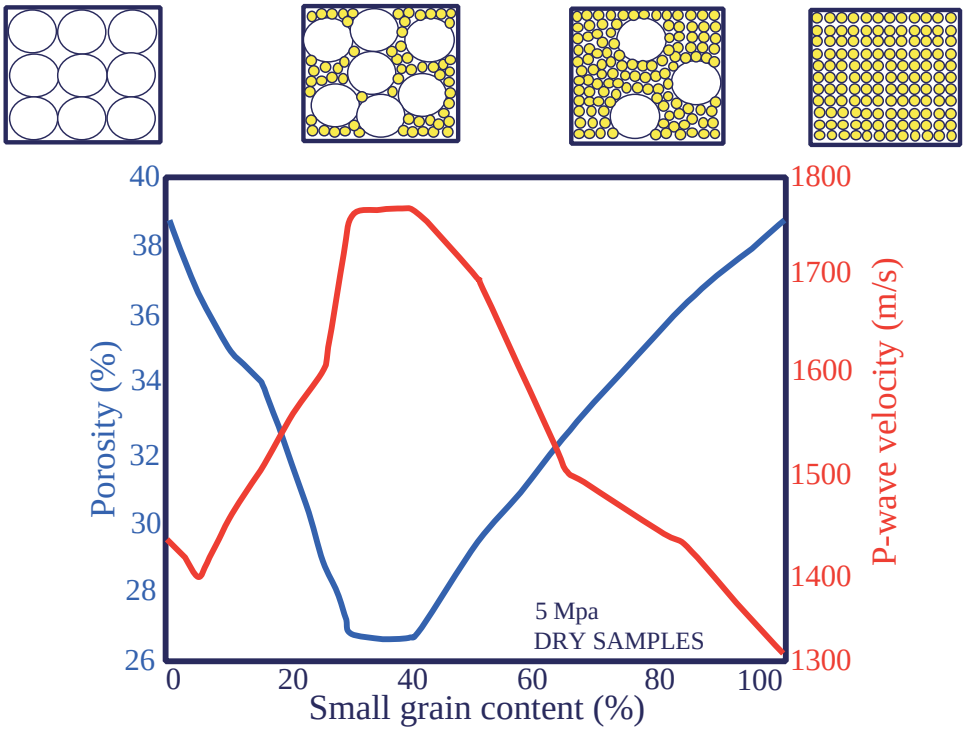

Figure 3.12: Example of the effect of textural sorting on porosity and velocity in bimodal mixtures of glass beads (Dataset from Estes et al., 1994).

The large and small well-sorted end members have similar porosity values, as expected, but when the smaller beads fill the pore space between the larger beads, the porosity drastically decreases. In other words, the observed clear dip in porosity is directly associated with a poor sorting of the grain mixture (Figure 3.12, blue line). These well-known results were fully documented by Cumberland and Crawford (1987). The glass mixture also shows a velocity peak that pairs with the dip in porosity when the beads samples are poorly sorted (Figure 3.12, red line). In this case, the deterioration of grain sorting results in a more efficient packing, thus causing the matrix mixture to stiffen and the velocity to increase.

Figure 3.13 is a cross plot of velocity versus porosity measurements from the Estes et al., (1994) glass bead dataset. This plot shows the effect of textural sorting, fluid saturation, and pressure on porosity and velocity. The blue arrow indicates the trend

created by the effect of sorting in a mixture of glass beads with similar fluid saturation (dry) and pressure (5 MPa). The well-sorted or texturally-mature end points show the highest porosity and the lowest velocity in the bimodal mixture. The deterioration of grain sorting produces the lowest stage of textural maturity, the lowest porosity, and the highest velocity in the bimodal mixture. This textural change creates a reduction in porosity from 39% to 27% and an increase in velocity from the range of 1300-1400 m/s to 1750 m/s.

The green arrow indicates the trend created by the effect of fluid saturation and pressure on porosity and velocity in a mixture with similar textural maturity. For example, the point of lowest textural maturity increases the velocity from 1750 m/s to 2750 m/s when the pressure increases from 5 MPa to 30 MPa. Similarly, the velocity increases from 1750 m/s to 3250 m/s when the dry pore space is saturated with water. In contrast, the pressure effect on porosity on this particular dataset is very small since the glass bead mixture has a mechanically stable framework and preserves high porosities after mechanical compaction.

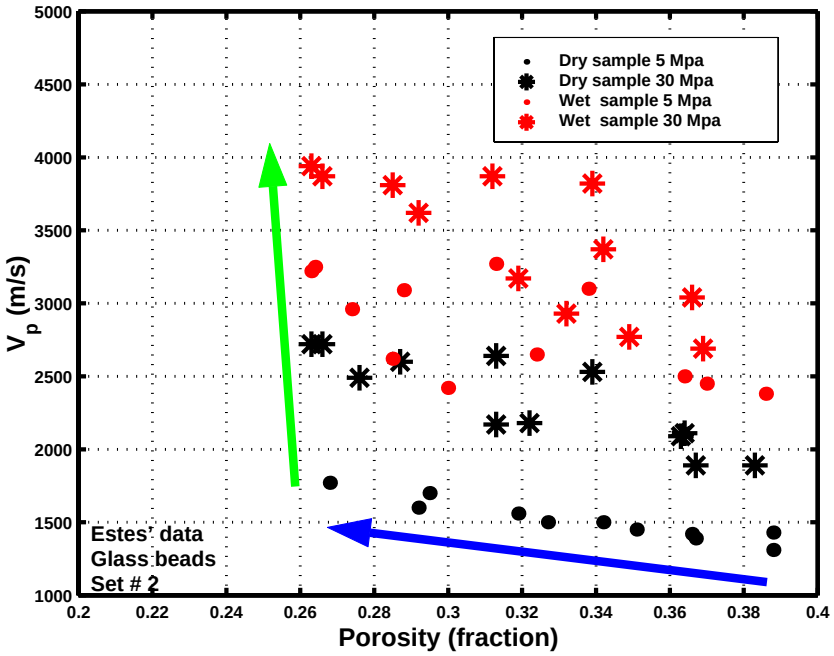

Figure 3.13: Cross plot of velocity versus porosity measurements in the Estes et al. (1994) glass beads dataset. It shows the effect of textural sorting, fluid saturation, and pressure on porosity and velocity.

These interesting observations in synthetic materials can be extrapolated to natural sedimentary rocks and can be used to extend the work of Clarke (1979) who concluded that there is a negative effect on porosity and permeability due to sorting of clastic reservoirs. In general, these measurements show that sediments with a uniform rigid composition and a low stage of textural maturity will exhibit a high velocity, in comparison with mature or supermature sediments. In other words, if the rock framework is mechanically stable, well-sorted clastic rocks with a simple diagenesis will exhibit better reservoir properties and lower elastic velocities that poorly-sorted clastic rocks.

Reservoir quality is not exclusively a function of rock texture. Composition and the relative content of detrital mineral components in clastic rocks also play an important role in the mechanisms of porosity reduction, such as mechanical compaction. Yin et al. (1988) and Yin (1992), in work with uncemented mixtures of rigid (sand) and ductile (clay) granular materials, investigated the combined effect of texture and clay content on porosity, permeability, and velocities. Bimodal samples were prepared by mixing, in different proportions, clean, well-sorted Ottawa sand grains with pure room-dried fine kaolinite particles.

Figure 3.14 is a cross plot of velocity versus porosity measurements for the Yin datasets. This plot shows the effect of textural sorting, detrital mineral composition, and pressure on porosity and velocity. Yin's measurements reveal systematic changes of porosity and velocity with clay content and the associated textural change. The red dots indicate the trend created by the effect of mechanical compaction in a sample of 100% well-sorted or texturally mature sands grains. This sand sample with a high content of mechanically-rigid grains is most likely to preserve high porosities and permeabilities after mechanical compaction.

The blue dots show the trend created by the effect of mechanical compaction in a sample of 100% kaolinite fine particles. This fine grain sample with a high content of ductile grains shows low framework stability. In this case, mechanical compaction by itself can drastically reduce original porosity and permeability.

The green dots indicate the trend created by the effect of sorting and mechanical compaction in a bimodal mixture of 60% Ottawa sands grains and 40% kaolinite fine grains. This particular grain mixing generates the highest deterioration of grain sorting

and produces the lowest stage of textural maturity. This stage is characterized by the lowest porosity and the highest velocity in the bimodal mixture.

When measurements are plotted at the same differential pressure, new trends are revealed. For example, a clear "inverted V" is discovered in the dataset if only the end-points at 50 MPa are outlined. Marion (1990) observes this "inverted V" in the Yin's dataset and isolates different trends in the porosity-velocity relationship: one for shaly sands and the other for sandy shales.

The shaly sands trend is between the 100% sands grains mixture and the bimodal mixture of 60% Ottawa sands grains and 40% kaolinite fine grains. In contrast, the sandy shales trend is between the pure kaolinite mixture and the bimodal mixture. Marion concludes that the "inverted V" is due to clay content and compaction. This conclusion can be extended and it can be defined that the "inverted V" is created by the effect of textural sorting, the framework stability of the grain mixture, and the degree of physical compaction.

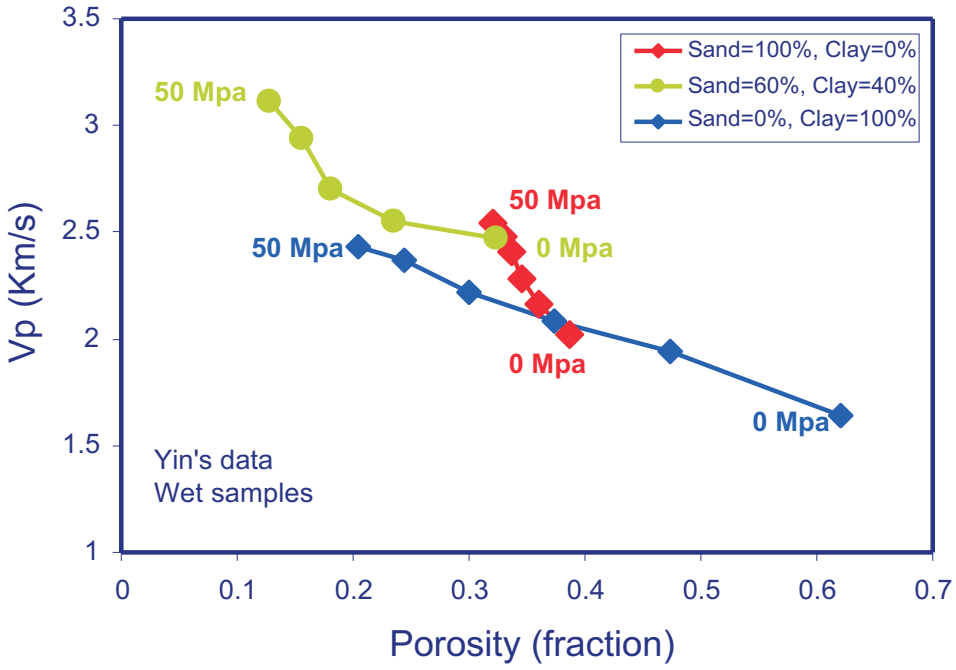

Figure 3.14: Cross plot of velocity versus porosity measurements in the Yin at al. (1988) and Yin (1992) datasets. It shows the effect of textural sorting, detrital composition, and physical compaction on porosity and velocity.

The combined effect of sorting and composition is illustrated in Figure 3.15. The plot schematically shows the typical trends under compaction of two bimodal mixtures at the low stage of textural maturity, and compares the Estes et al., (1994) dataset with the Yin et al. (1998) and Yin (1992) datasets. Both sets have similar textural sorting, but a very different grain composition. As previously indicated, the Estes et al. data framework is very stable and only minorly reduces the porosity (green arrow). In contrast, the presence of ductile grains (e.g., clay) in the Yin's data, reduces the stability of the framework, increases the compaction rate, and drastically reduces the porosity (blue arrow).

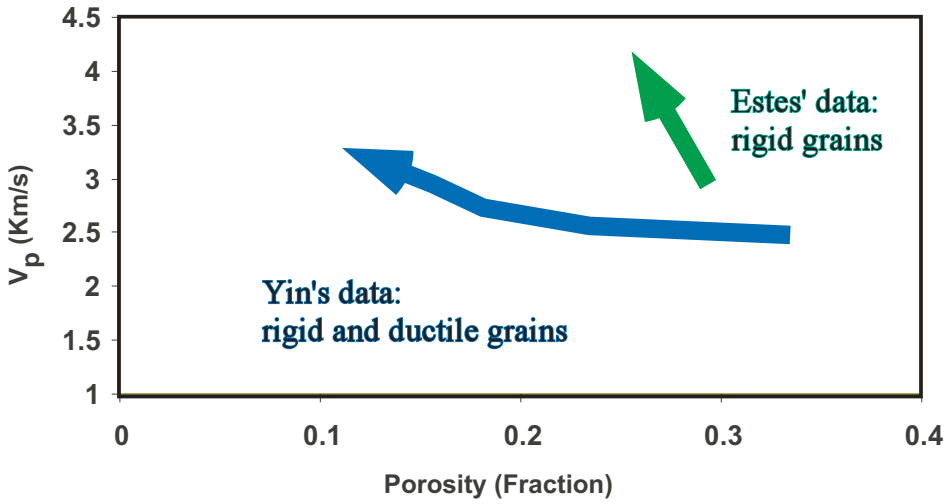

Figure 3.15: Sorting and composition, low stage of textural maturity.

Effect of Sorting on Elastic Velocity–Theory

Some effective medium models for granular composites, such as the constant cement and uncemented sand models (Dvorkin et al., 1991, 1994; Dvorkin and Nur, 1996), mimic the process of deteriorating sorting in sands (Appendix A). Core analysis supports the hypothesis that in the constant cement model, the data and the theoretical curve deviate from the contact cement curve, because grain sorting starts to deteriorate at the cemented porosity point (Avseth et al., 2000). This also provides the reasoning for the uncemented sand model: smaller particles fall between the larger well-sorted grains (Figure 3.16).

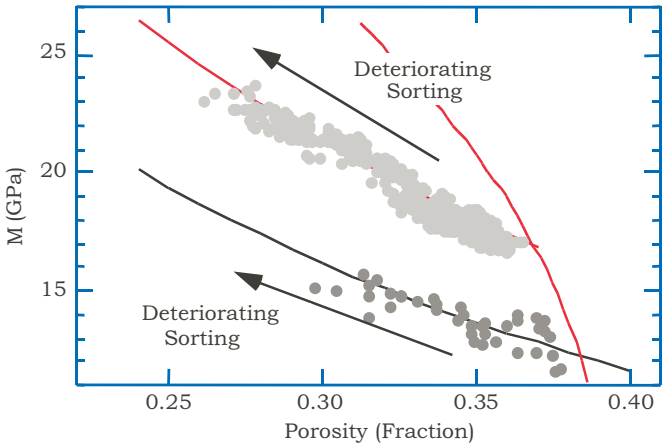

Figure 3.16: Porosity reduction in sands due to deteriorating sorting. M means compressional modulus.

Geometry of a Bimodal Grain Mixture. The focus of this analysis is a bimodal mixture of elastic spheres or perfectly rounded grains. An initial assumption establishes that there are only two grain sizes present in the mixture: large grains and small grains. The diameter of the former is much larger than that of the latter. Depending on the volumetric fraction of the large and small grains, various configurations are possible, as shown in Figure 3.17, where on the left (frame a) we have only large particles and on the right (frame e) only small particles. Let the number of large particles in a representative volume be L and that of small particles be l (Figure 3.18). The radii of the particles are R (for large particles) and r (for small particles).

The total volume of the small grains when they are packed together at porosity ϕ_{cs}, which is the critical porosity for the small grains (as in Figure 3.17, frame a), is

$$\frac{4}{3}\frac{\pi r^3 l}{1-\phi_{cs}}. \tag{3.9}$$

That of the large grains when they are packed together at porosity ϕ_{cl}, which is the critical porosity for the large grains (as in Figure 3.17, frame a), is

$$\frac{4}{3}\frac{\pi R^3 L}{1-\phi_{cl}}. \tag{3.10}$$

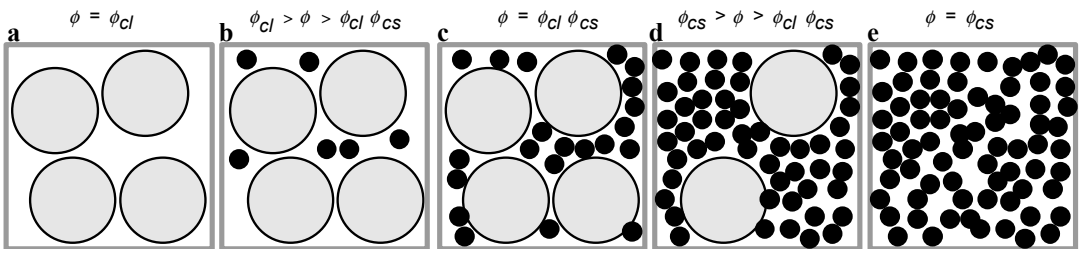

Figure 3.17: Porosity reduction in sands due to deteriorating sorting.

The pore-space volume of the large grains packed together is

$$\frac{4}{3}\frac{\phi_{cl}\pi R^3 L}{1-\phi_{cl}}. \tag{3.11}$$

If the volume of the small grains in a pack is smaller than the pore-space volume of the large grains in a pack, all small grains can be accommodated inside the pore space of the large grain pack. We then have a configuration as shown in Figure 3.17, frame b. The condition for this geometry is

$$\frac{4}{3}\frac{\pi r^3 l}{1-\phi_{cs}} \le \frac{4}{3}\frac{\phi_{cl}\pi R^3 L}{1-\phi_{cl}} \Rightarrow \left(\frac{r^3 l}{1-\phi_{cs}}\right) / \left(\frac{R^3 L}{1-\phi_{cl}}\right) \le \phi_{cl} \Rightarrow \beta \le \phi_{cl}, \tag{3.12}$$

where

$$\beta \equiv \left(\frac{r^3 l}{1-\phi_{cs}}\right) / \left(\frac{R^3 L}{1-\phi_{cl}}\right). \tag{3.13}$$

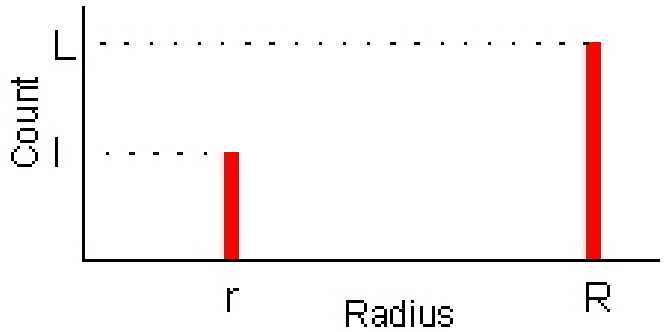

Figure 3.18: Size distribution in a binary particle mixture.

The total porosity ϕ of this mixture is

$$\phi = \phi_{cl} - \beta(1 - \phi_{cs}). \tag{3.14}$$

If the volume of the small grain pack equals that of the pore-space volume of the large grain pack, then $\beta = \phi_{cl}$ and

$$\phi = \phi_{cl}\phi_{cs}, \tag{3.15}$$

as in Figure 3.17, frame c.

In the case of $\beta > \phi_{cl}$, the large grains will be suspended in the pack of the small grains (Figure 3.17, frame d). The total volume of the composite is

$$\frac{4}{3}\pi R^3 L + \frac{4}{3}\frac{\pi r^3 l}{1 - \phi_{cs}} \tag{3.16}$$

and the pore volume is that of the small grain pack:

$$\frac{4}{3}\frac{\phi_{cs}\pi r^3 l}{1 - \phi_{cs}}. \tag{3.17}$$

As a result, the total porosity of the composite is

$$\phi = \frac{\phi_{cs}}{1 + (1 - \phi_{cl})/\ \beta}. \tag{3.18}$$

If $\beta = \phi_{cl}$, then the large grains touch each other and $\phi = \phi_{cl}\phi_{cs}$. If $\beta = \infty$, which means that only the small grains are present, the porosity of the composite is ϕ_{cs}. The summary of these results is:

$$\begin{aligned}
&\phi = \phi_{cl} \quad \Leftarrow \beta = 0;\\
&\phi = \phi_{cl} - \beta(1 - \phi_{cs}) \quad \Leftarrow \beta < \phi_{cl};\\
&\phi = \phi_{cl}\phi_{cs} \quad \Leftarrow \beta = \phi_{cl};\\
&\phi = \phi_{cs} / \ [1 + (1 - \phi_{cl})/\ \beta] \quad \Leftarrow \beta > \phi_{cl};\\
&\phi = \phi_{cs} \quad \Leftarrow \beta = \infty.
\end{aligned} \tag{3.19}$$

The corresponding graph of the total porosity of the composite is given in Figure 3.19.

Elasticity of a Bimodal Grain Mixture. In this section, an initial assumption is that $\beta \geq \phi_{cl}$, i.e., the small grains fill the entire pore space of the large grain pack, or the large grains are suspended in the small grain pack (Figure 3.17, frames c, d, and e). Here also, a second assumption defines that the elastic moduli of the large grain material are much larger that those of the small grain pack. In this case, and because the small grain pack (soft) envelopes the large grains (stiff), a new approach is presented, where the effective elastic moduli of the composite is modeled as the lower Hashin-Shtrikman bound of two elastic components where the soft component is defined as the small grain pack and the stiff component is defined as the large grain pack.

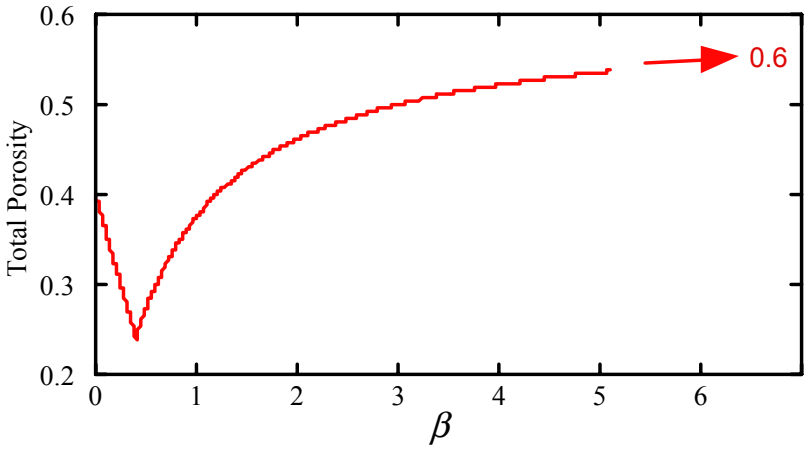

Figure 3.19: Total porosity versus the ratio of the small grain pack volume to the large grain pack volume. The critical porosity for large grains is 0.4 and that for small grains is 0.6.

For $\beta \geq \phi_{cl}$, the total volume of the composite is given by Equation 3.16 and the volume of the small grain pack is $4\pi r^3 l / [3(1-\phi_{cs})]$. Therefore, the volumetric concentration of the small grain pack (the soft component) in the composite is

$$f_{Soft} = \frac{1}{1+(1-\phi_{cl})/\beta}. \tag{3.20}$$

The Hashin-Shtrikman lower bound then gives the following effective-medium elastic moduli of the dry composite:

$$K_{EM} = [\frac{f_{Soft}}{K_{Soft} + (4/3)G_{Soft}} + \frac{1 - f_{Soft}}{K_l + (4/3)G_{Soft}}]^{-1} - \frac{4}{3} G_{Soft},$$
$$G_{EM} = [\frac{f_{Soft}}{G_{Soft} + Z_{Soft}} + \frac{1 - f_{Soft}}{G_l + Z_{Soft}}]^{-1} - Z_{Soft}, \; Z_{Soft} = \frac{G_{Soft}}{6} \frac{9K_{Soft} + 8G_{Soft}}{K_{Soft} + 2G_{Soft}}, \tag{3.21}$$

where K_l and G_l are the bulk and shear moduli of the large grain material, respectively, and K_{Soft} and G_{Soft} are the bulk and shear moduli of the small grain pack, respectively.

If the small grain pack can be approximated by a random dense pack of identical elastic spheres, its elastic moduli can be calculated from the Hertz-Mindlin contact theory (Mavko et al., 1998) as

$$K_{Soft} = [\frac{n_s^2 (1 - \phi_{cs})^2 G_s^2}{18\pi^2 (1 - \nu_s)^2} P]^{\frac{1}{3}}, \; G_{Soft} = \frac{5 - 4\nu_s}{5(2 - \nu_s)} [\frac{3 n_s^2 (1 - \phi_{cs})^2 G_s^2}{2\pi^2 (1 - \nu_s)^2} P]^{\frac{1}{3}};$$
$$\nu_s = \frac{1}{2}(\frac{K_s}{G_s} - \frac{2}{3}) / \; (\frac{K_s}{G_s} + \frac{1}{3}), \tag{3.22}$$

where K_s and G_s are the bulk and shear moduli of the small grain material, respectively, P is the differential pressure, and n_s is the coordination number (the average number of contacts per grain) for the pack of small grains. This approximation may not be appropriate if the small grain pack is a pack of, for example, clay particles.

Consider now the case $\beta \le \phi_{cl}$ (Figure 3.17, frames a, b, and c). The two elastic end-members are: (1) $\beta = 0$, i.e., the pack of the large grains (without small grains present in the pore space, Figure 3.17, frame a) with porosity ϕ_{cl}; and (2) $\beta = \phi_{cl}$, i.e., the small grains fill the entire pore space of the large grain pack (Figure 3.17, frame c).

The elastic moduli of the first end-member (at $\beta = 0$) can be calculated from the Hertz-Mindlin contact theory by assuming that the large grains are identical elastic spheres with bulk modulus K_l, shear modulus G_l, and coordination number n_l.

Then the bulk modulus K_1 and the shear modulus G_1 are:

$$K_1 = [\frac{n_l^2(1-\phi_{cl})^2 G_l^2}{18\pi^2(1-\nu_l)^2} P]^{\frac{1}{3}},\ G_1 = \frac{5-4\nu_l}{5(2-\nu_l)}[\frac{3n_l^2(1-\phi_{cl})^2 G_l^2}{2\pi^2(1-\nu_l)^2} P]^{\frac{1}{3}};$$
$$\nu_l = \frac{1}{2}(\frac{K_l}{G_l} - \frac{2}{3}) / (\frac{K_l}{G_l} + \frac{1}{3}). \tag{3.23}$$

The bulk and shear moduli of the second end-member are given by Equations 3.21 where f_{Soft} has to be replaced by ϕ_{cl}:

$$K_2 = [\frac{\phi_{cl}}{K_{Soft} + (4/3)G_{Soft}} + \frac{1-\phi_{cl}}{K_l + (4/3)G_{Soft}}]^{-1} - \frac{4}{3}G_{Soft},$$
$$G_2 = [\frac{\phi_{cl}}{G_{Soft} + Z_{Soft}} + \frac{1-\phi_{cl}}{G_l + Z_{Soft}}]^{-1} - Z_{Soft},\ Z_{Soft} = \frac{G_{Soft}}{6}\frac{9K_{Soft} + 8G_{Soft}}{K_{Soft} + 2G_{Soft}}. \tag{3.24}$$

These two end points can be connected by a lower Hashin-Shtrikman bound curve. In order to calculate the volumetric fractions of the two end members in the composite, a new assumption must be made to define that the two end-members added together result in the given numbers of small and large grains (Figure 3.20).

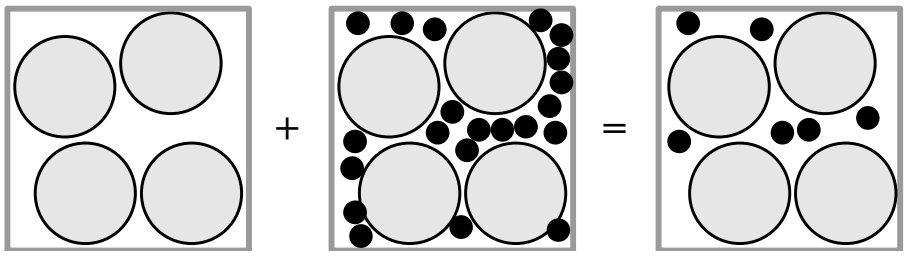

Figure 3.20: Two end members added provide required configuration.

If the volume fraction of the first end member in the composite is f_1 and that of the second end member is $f_2 = 1 - f_1$, then the number of the small grains in a unit volume of the composite is

$$l = \frac{f_2\phi_{cl}(1-\phi_{cs})}{4\pi r^3 / 3} \tag{3.25}$$

and the number of the large grains is

$$L = \frac{1-\phi_{cl}}{4\pi R^3 / 3}. \tag{3.26}$$

Then

$$\beta \equiv (\frac{r^3 l}{1-\phi_{cs}}) / (\frac{R^3 L}{1-\phi_{cl}}) = f_2 \phi_{cl}. \tag{3.27}$$

As a result,

$$f_2 = \beta / \phi_{cl},\ f_1 = 1 - f_2. \tag{3.28}$$

Then, the Hashin-Shtrikman lower bound of the mixture of the elastic end members with the bulk and shear moduli K_1 and G_1, and K_2 and G_2, respectively, and volume fractions f_1 and f_2, respectively, is

$$\begin{aligned} K_{EM} &= [\frac{f_1}{K_1 + (4/3)G_1} + \frac{f_2}{K_2 + (4/3)G_1}]^{-1} - \frac{4}{3}G_1, \\ G_{EM} &= [\frac{f_1}{G_1 + Z_1} + \frac{f_2}{G_2 + Z_1}]^{-1} - Z_1,\ Z_1 = \frac{G_1}{6}\frac{9K_1 + 8G_1}{K_1 + 2G_1}, \end{aligned} \tag{3.29}$$

and it is assumed that the first end member is softer than the second end member.

Equations (3.21) and (3.29) provide the elastic moduli of the composite's dry frame. In the low-frequency limit, the shear modulus of the saturated composite is the same as that of the dry frame. The bulk modulus of the saturated composite K_{Sat} can be calculated from that of the dry composite using Gassmann's equation

$$K_{Sat} = K_{Solid}\frac{\phi K_{EM} - (1+\phi)K_{Fluid}K_{EM}/K_{Solid} + K_{Fluid}}{(1-\phi)K_{Fluid} + \phi K_{Solid} - K_{Fluid}K_{EM}/K_{Solid}}, \tag{3.30}$$

where K_{Fluid} is the bulk modulus of the pore fluid and K_{Solid} is that of the composite solid. K_{Solid} can be calculated by mixing the material of the large grains with that of the soft grains and using, for example, Hill's average (Mavko et al., 1998). The volume of the solid material in the large grains is $4\pi R^3 L/3$ and of the small grains is $4\pi r^3 l/3$. The

volume fraction f_l of the large grain material in the entire solid phase of the composite is then

$$f_l = \frac{R^3 L}{R^3 L + r^3 l} = \frac{1}{1 + r^3 l / (R^3 L)} = \frac{1}{1 + \beta(1-\phi_{cs}) / (1-\phi_{cl})}. \tag{3.31}$$

The resulting Hill's average is

$$K_{Solid} = \frac{1}{2}[f_l K_l + (1-f_l)K_s + (\frac{f_l}{K_l} + \frac{1-f_l}{K_s})^{-1}]. \tag{3.32}$$

This new bimodal grain mixture model is applied successfully to field data in the Section 3.4.2.

3.3.4 Application of Theoretical Rock Physics Models to Synthetic Data

To match theory to the elastic behavior of laboratory data, the uncemented sand model of Dvorkin and Nur (1996) (Appendix A) and the Estes et al., (1994) synthetic dataset are used. This model is an effective-medium model that connects two end-points in the elastic-moduli-porosity plane. One end-point is at the critical porosity (about 40%) where the sand is modeled as a pack of elastic spheres.

The other end-point is at zero porosity where the elastic moduli of the rock are those of the solid phase. The connecting trajectory is designed to model the porosity reduction where smaller particles are deposited away from the large grain contacts (deteriorating sorting). The pressure dependence is introduced through the elastic moduli of the dry frame at the critical porosity, according to the Hertz-Mindlin elastic sphere contact model.

Velocity versus porosity for Estes et al. glass beads dataset at different pressures is plotted in Figure 3.21. The overlapped unconsolidated model curve in red is for 100% dry rock. The effective pressure in the model is 5 MPa. and the framework mineralogy used for modeling is glass. Note the excellent match between the theoretical prediction and the experimental data. This observation illustrates how well the uncemented model from Dvorkin and Nur (1996) predict the effect of textural sorting on velocity and porosity, if the framework composition is uniform.

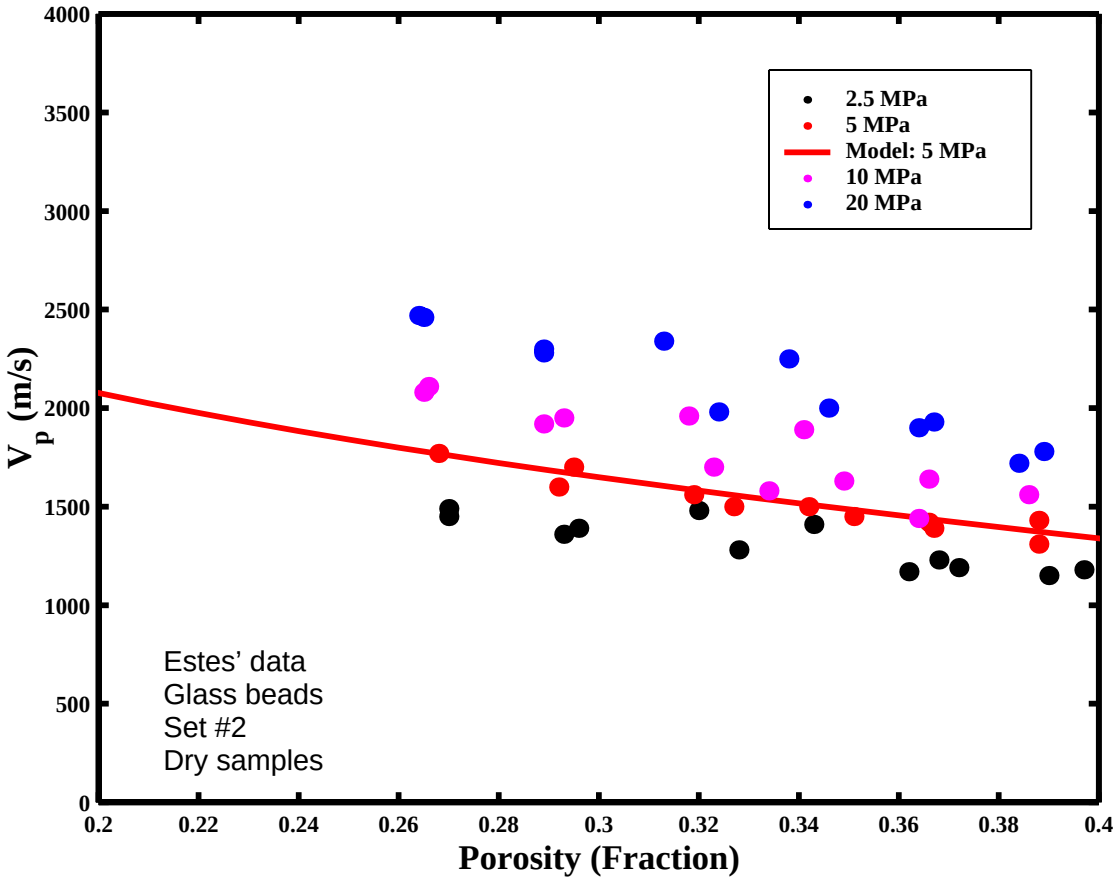

Figure 3.21: Velocity versus porosity for Estes at al. glass beads dataset at different pressures. The data points are color-coded according to the pressure. The overlapped unconsolidated model curve in red is for 100% dry rock. The effective pressure in the model is 5 MPa. The framework mineralogy used for modeling is 100% glass.

3.4 Stratigraphy-constrained Rock Physics Model for Reservoir Quality Prediction

Conventional seismic characterization of hydrocarbon reservoirs focus on finding the geological significance of reflection information and/or attributes thereof (e.g., seismic amplitude). Mathematical techniques, such as geostatistics, neural networks, and cluster analysis are often used to relate such attributes to reservoir physical properties. However, these techniques are often unable to provide correct reservoir property description because they do not take advantage of deterministic physical links between seismic and reservoir properties.

By analyzing well logs and core data, and integrating essential concepts of sedimentary geology and theoretical rock physics, I determine a governing effective-medium-based rock physics model for La Cira-Infantas reservoirs. This LCI rock physics model relates the elastic reservoir properties to porosity, mineralogy, pore fluid, and differential pressure, using the stratigraphic framework as a constraint to select the relevant data subsets. These relations can be rationalized and explained by effective-medium models.

The key to obtaining such models is consistency between reservoir sedimentological characteristics (e.g., texture and composition), well log data (e.g., GR), and core analysis (e.g., porosity and velocity). The practical goals of the rock physics model are to: (a) simplify the relations observed in well log and core data, (b) define the ranges of applicability of these physical relations, (c) separate the effects of porosity from those of pore fluid on seismic properties, and (d) interpret seismic impedance inversion in terms of reservoir quality.

3.4.1 Cycles in Stratigraphy

Stratification is a fundamental characteristic of sedimentary rocks. Cyclic and episodic processes or events, and biologic and diagenetic overprint generally produce stratification in the sedimentary record. Strata usually show a specific rhythmicity or cyclicity, due to regularly alternating beds or repeated series of particular lithologies, which are better known as depositional cycles (Einsele et al., 1991).

Genetically, depositional cycles are controlled by two groups of sedimentary mechanisms: autogenic (within-basin) and allogenic (extra-basinal). Autogenic examples in fluvial systems are the migration and superposition of channel systems. In constrast, allogenic sequences are caused by changes external to the basin, such as climatic variations, tectonic movements (Miall, 1997).

Geoscientists study sedimentary processes, including cyclicity and resultant depositional products, at different time and physical scales. Miall (1996) suggests a classification of reservoir architectural units and their associated sedimentary processes, according to depositional time scale, into 10 classes spanning at least 12 orders of magnitude, from the lamina at one extreme to a basin-fill complex at the other extreme.

Miall also reviews a hierarchy of physical scales, presenting at least 14 orders of magnitude, from the few square centimeters in area of the smallest scale of a ripple foreset, to the ten of thousands of square kilometers of a major sedimentary basin.

The original sedimentary cycles can be affected by several diagenetic processes. Diagenesis comprises a range of mechanical and chemical processes during burial history, such as mechanical compaction, cementation, replacement of unstable minerals, displacement of components, dolomitization, and dissolution (Blatt et al., 1980; Boggs, 1995).

3.4.2 Mugrosa Formation Reservoirs (Zones B and C)

The siliciclastic reservoirs in LCI belong to the Colorado Formation (Zone A) and Mugrosa Formation (Zones B and C). Oil production comes from loosely consolidated Tertiary sands. The reservoir rocks are fine to medium grained, subarkosic, clean-to-shaly sandstones. Average porosity is 20% in Zone B, and 23% in Zone C. Permeability may reach 1500 mD (Figure 3.22). It is highly variable laterally and vertically (Dickey, 1992).

This section focus in characterizing the rock properties and rock physics attributes of the Mugrosa Formation reservoirs. Zone B comprises a thick succession (550 m) of alternating fine-grain sandstones and shales (Dickey, 1992). The lower part of the sequence consists of dull blue and brown, massive, mottled shales with some thin interbeds of fine-grained sandstones and light-green sandy shales. The upper part of the formation is gray, fine to coarse grained, somewhat pebbly sandstone, interbedded with minor amounts of green and mottled shales (Morales et al, 1958).

Zone C is the most prolific reservoir in La Cira-Infantas. This reservoir zone is gray to grayish green, fine- to medium-grained, rarely coarse and pebbly sandstones, with interbedded gray, blue, and red shales (Morales et al., 1958). Sequence stratigraphy indicates that the depositional facies in the La Cira-Infantas Tertiary rocks are associated with fluvial channel systems. Zone B represents mixed load channels or meandering systems, whereas Zone C was deposited as bed load channels or braided stream systems (Laverde, 1996).

In order to relate the elastic reservoir properties to porosity, mineralogy, pore fluid compressibility, and effective pressure, modern high-quality well-log data from La Cira-

Infantas wells 1880 and 1882 are used, where core data are available as well. First, the position of La Cira-Infantas sands in the rock physics space is identified by plotting velocity versus porosity for a major fining-up sedimentary cycle, between 791 m and 915 m of depth, in well LC-1880 (Figure 3.23).

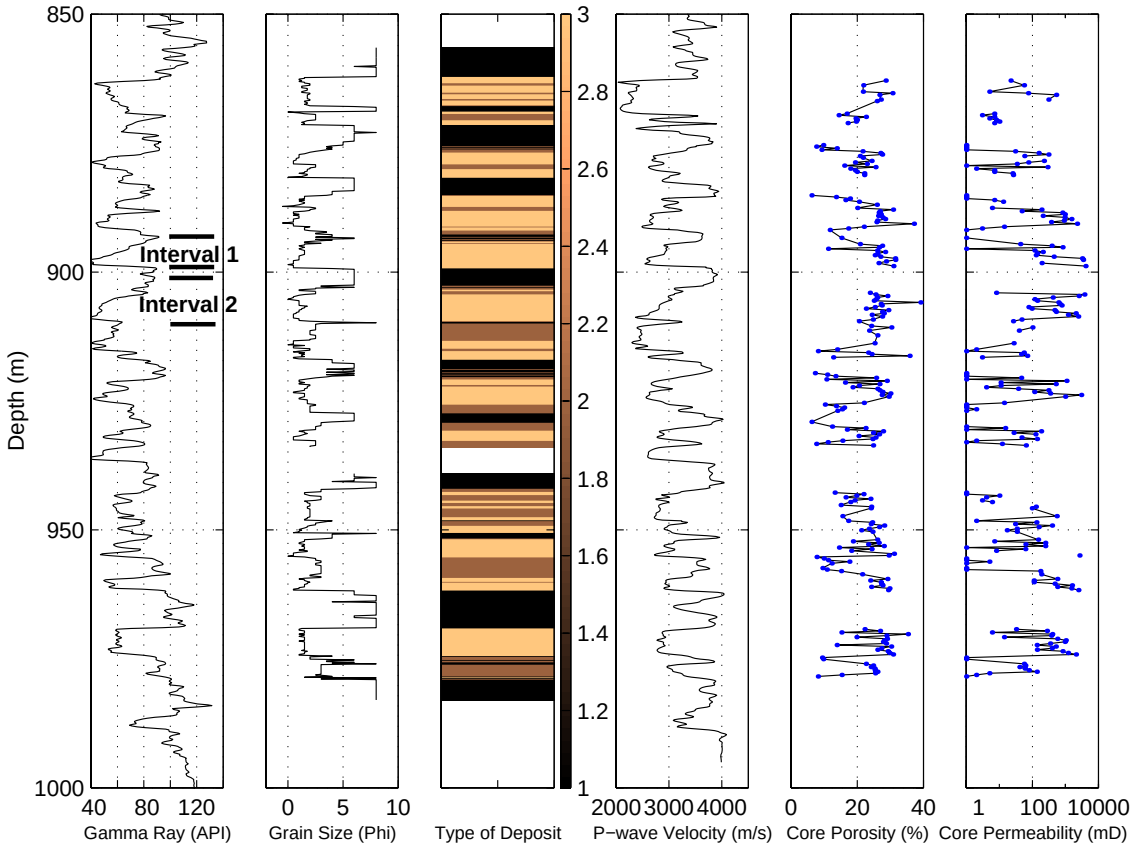

Figure 3.22: Well LC-1880, Zone C. Typical gamma-ray response, grain size distribution, type of deposit, P-wave velocity log, core porosity, and permeability. The classification of deposits (third frame from the left, with a color key) is based on the grain size: (1) suspended-load (mud/silt), (2) mixed-load (fine-sand), and (3) bed-load (gravel and sand) (Orton and Reading, 1993). Marked are the two fining-up cycles selected for modeling (Intervals 1 and 2).

Superimposed on the cross-plot are several model curves. The data points lie well below the "fast" Wyllie, Raymer, and critical porosity curves. This means that the rocks are unconsolidated and lack cementation, which is common for shallow early-Tertiary La Cira-Infantas sediments. Another feature apparent in Figure 3.23 is a large scatter of the data points around the general trend. The scatter reduces if basic sequence stratigraphy is used to guide the modeling (Figures 3.24 and 3.25).

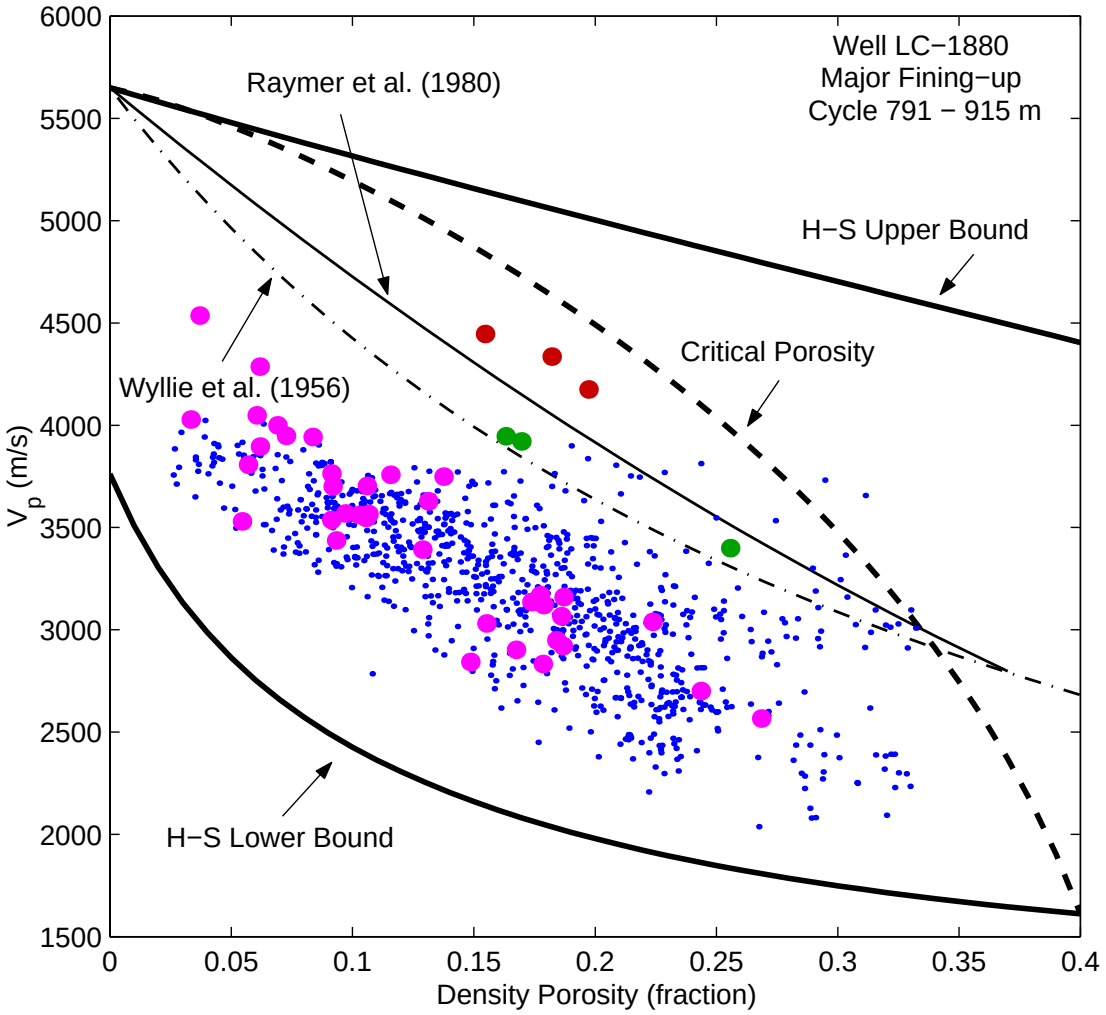

Figure 3.23: Velocity versus porosity in well LC-1880 and La Cira-Infantas core data (pink dots) with model curves superimposed. The models are: (a) the Hashin-Shtrikman upper and lower bounds, (b) critical porosity, (c) Wyllie's time average and (d) the Raymer et al. model. (See description of the models in Mavko et al., 1998). The solid-phase P-wave velocity and density used in the models are 5.65 km/s and 2.64 g/cc, respectively (for a mixture of 80% quartz and 20% feldspar typical for the arkosic sands of La Cira-Infantas). The fluid phase is brine whose bulk modulus and density are 2.5 GPa and 1 g/cc, respectively. The large symbols are for selected consolidated sandstones, clean (red) and with clay (green), based on Han's data (1986). The velocity in the cores was calculated by assuming that they are 100% water saturated and applying Gassmann's equation to the dry-rock lab data.

In Figure 3.25, velocity versus porosity is cross-plotted for consecutively smaller depositional cycles. Stratigraphy terminology for the selected cycles was adapted from Miall (1996). The first cross-plot (Figure 3.25a) corresponds to the large 850 m interval (basin-fill complex scale), shown in Figure 3.24a. The correlation coefficient here is very

small because the interval consists of many smaller cycles with complex geological and diagenetic history.

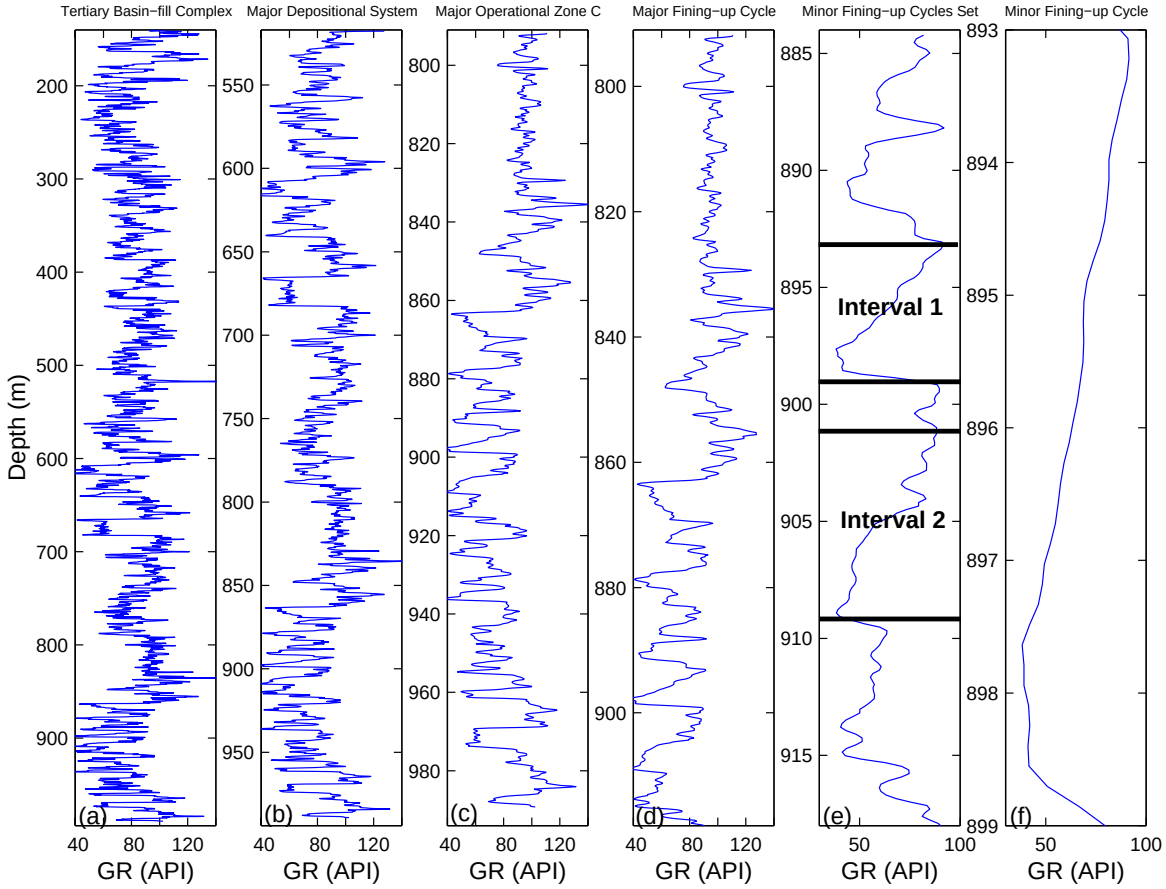

Figure 3.24: Gamma ray versus depth in well 1880 for increasing order of cyclicity. The order of the plots corresponds to that in Figure 4.5. Marked as Intervals 1 and 2 are the two fining-up cycles selected for modeling.

The correlation coefficient increases as I choose smaller cycles within which the sedimentary environment conditions and diagenetic nature of the sands are more uniform. The final cross-plot in Figure 3.25f shows a high-correlation trend for a single well-developed fining-up cycle between 893.21 m and 898.48 m of depth (see gamma ray versus depth in Figure 3.24f). This final subset of the data will be used for rock physics modeling.

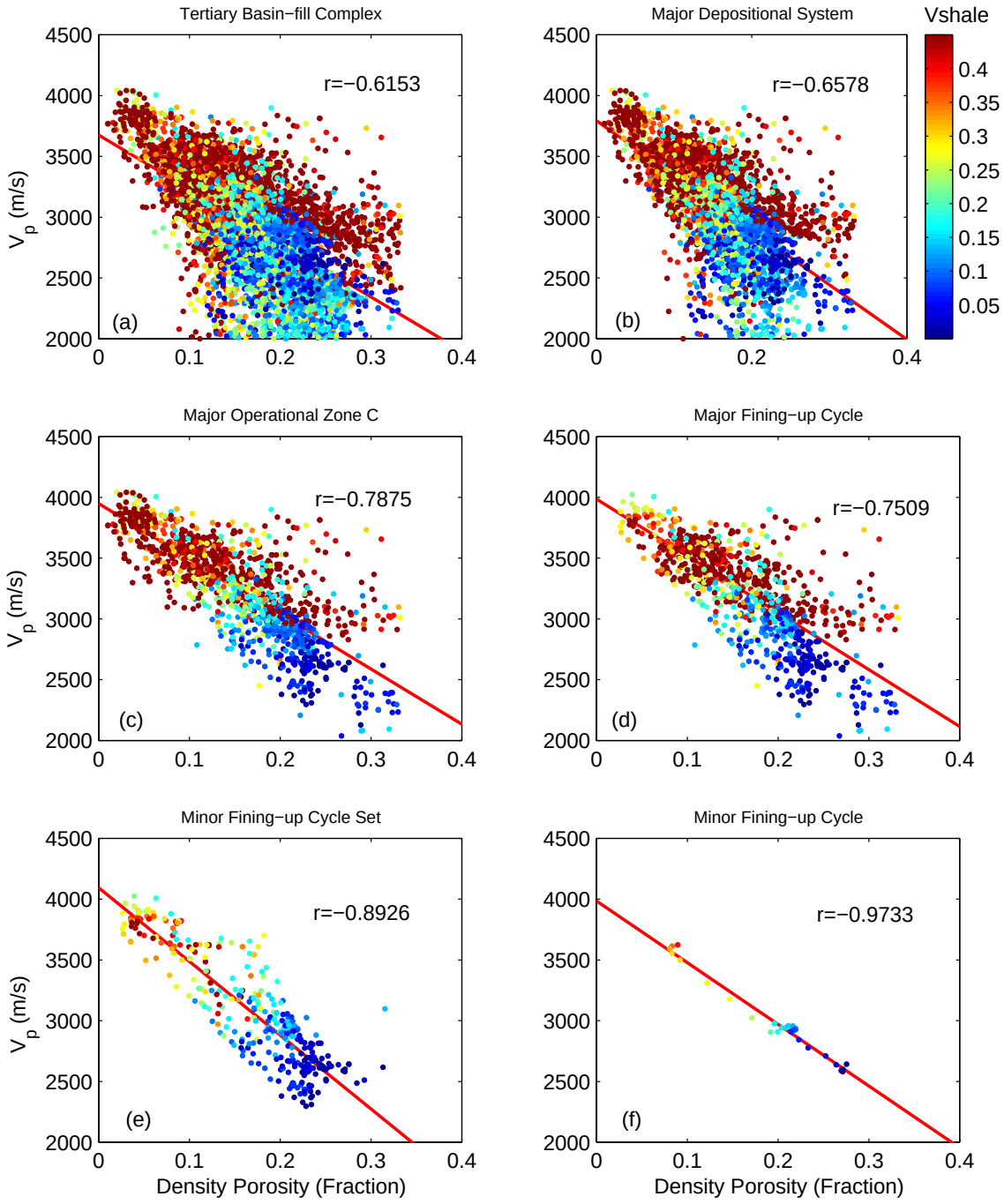

Figure 3.25: Velocity versus density-derived porosity in well 1880 for increasing order of cyclicity (increasing resolution). The data points are color-coded according to shale content, which was calculated from the gamma-ray data. The straight lines are a linear fit to the data with the correlation coefficient shown in the plots. The corresponding gamma-ray versus depth plots are shown in Figure 3.24.

To develop a rock physics model that links porosity, mineralogy, pressure, and pore fluid bulk modulus to the elastic rock properties, I use well log data from well LC-1880. Consider an interval between 885 m and 915 m (Figure 3.26) where two fining-up depositional cycles are highlighted in the GR track.

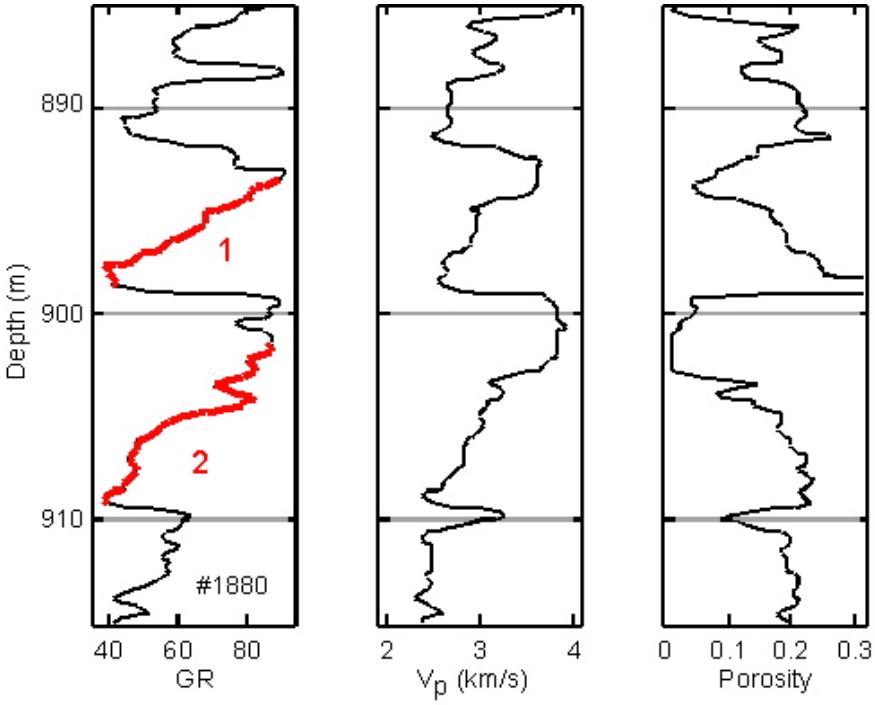

Figure 3.26: Well LC-1880, Zone C. Two minor fining-up cycles chosen for rock physics modeling. Cycle 1 on top and Cycle 2 below.

To match the elastic behavior of the selected depositional cycle, I again choose the uncemented sand model of Dvorkin and Nur (Mavko et al., 1998). This choice is based on the fact that the sand under examination appears to be uncemented and much softer than consolidated sandstone in the same porosity range (Figure 3.23).

Figure 3.27 gives the velocity- and impedance-porosity trends for the selected fining-up ward cycle with the model curves superimposed. The upper curve corresponds to the clean-sand (80% quartz and 20% feldspar) and the lower curve is for 55% quartz, 20% feldspar, and 25% clay. It is now apparent that the velocity-porosity trend observed in the data is not a simple linear trend. The data points move from the clean-sand model curve to the shaly-sand curve as porosity decreases and shale content increases.

Next, I use the theoretical model to understand the velocity behavior in another minor fining-up ward cycle between 900.53 m and 908.76 m (Figure 3.26). In this case, the selected clean-sand model also accurately matches the low-shale content data points (Figure 3.28). However, in order to match the high-shale content points in this interval, I must allow for only 20% quartz and 20% feldspar and increase the clay content from 25% (as in the first selected cycle) to 60%. This selection of mineralogy, although seemingly arbitrary, is consistent with the grain size and classification of deposits in the intervals selected (Figure 3.22). In the first cycle the lithology varies from clean sand to siltstone whereas in the second cycle the lithology changes from clean sand to claystone.

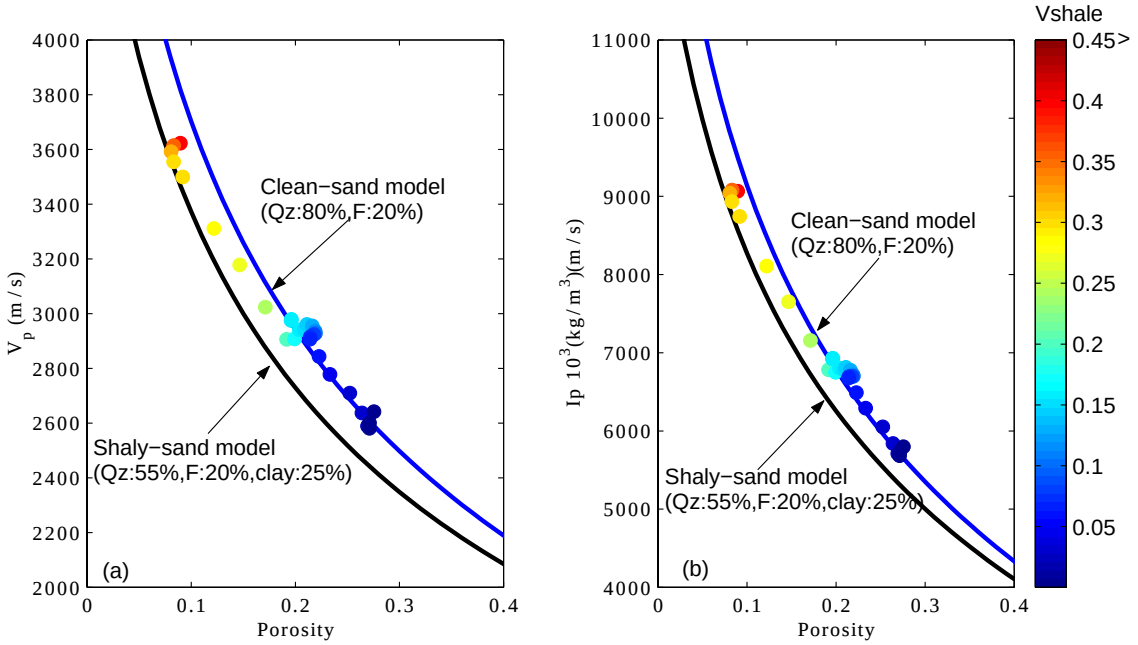

Figure 3.27: Velocity and impedance versus porosity for a fining-up ward cycle between 893.21 m and 898.48 m. The data points are color-coded according to the GR-derived shale content. The model curves are for 100% water saturated rock (I assume that the sonic tool samples the mud filtrate invasion zone). The effective pressure in the model is 12 MPa. The mineralogy used for modeling is given on the plots.

In effect, by applying the selected rock physics model to the data, I diagnose the rock, i.e., predict mineralogy from velocity and porosity (Asveth et al., 2000). This rock physics diagnostic is important because the clay content strongly affects the quality of the rock (or the permeability). Moreover, by diagnosing the rock I implicitly predict the rock

strength (friability) from velocity and porosity by showing that the data fall on the uncemented-sand model.

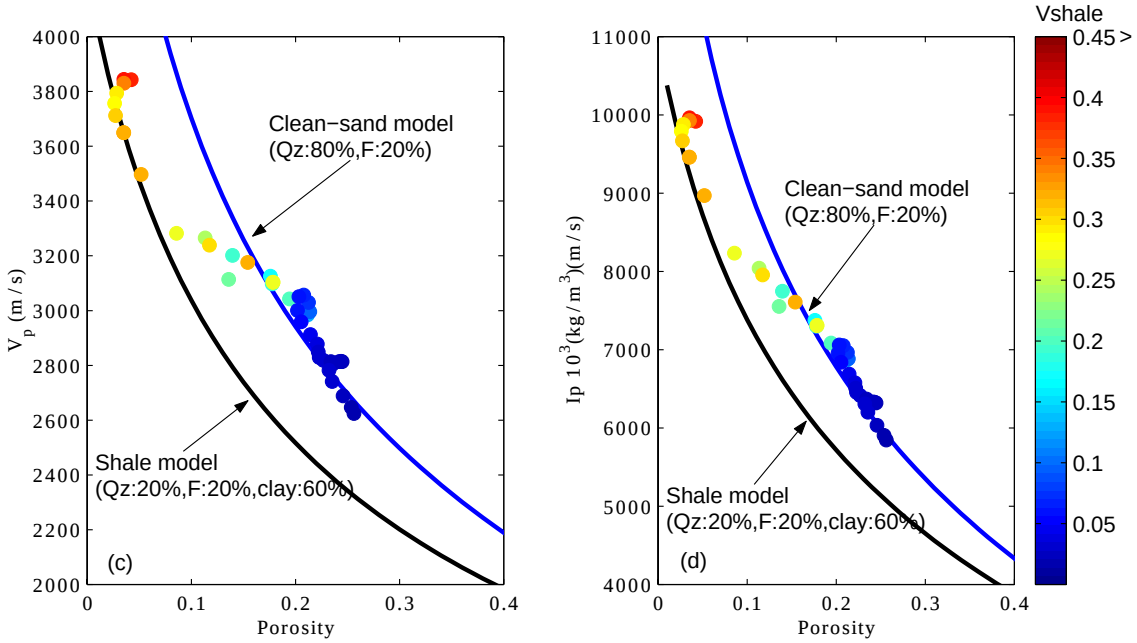

Figure 3.28: Same as Figure 3.27 but for a fining-up cycle between 900.53 m and 908.76 m.

It is apparent from Figures 3.25, 3.27, and 3.28 that the impedance of the high-shale content sand is higher than that of the low-shale content sands. This observation is in apparent contradiction to some of the existing velocity-porosity models (e.g., Han, 1987) where clay acts to decrease the rock's velocity. In fact, in the case under examination, the clay content in the intervals with 100% shale may be as low as 20%-30%.

As it turns out, "shale" in La Cira-Infantas actually contains a large fraction of silt that has mineralogy close to that of clean sand (Figures 3.2 and 3.9). Consequently, the main difference between shale and sand in La Cira-Infantas is grain sorting, which deteriorates in the shaly layers. This poor sorting in shales acts to reduce the total porosity (as compared to clean sands) and thus acts to increase the velocity.

The rock physics model established here will serve as the basis for interpreting seismic data for porosity and the presence of hydrocarbons in the high-resolution stratigraphic cycles. Once porosity values are established, it will be straightforward to

estimate permeability in LCI because a good correlation exists between the two parameters (Figure 3.29).

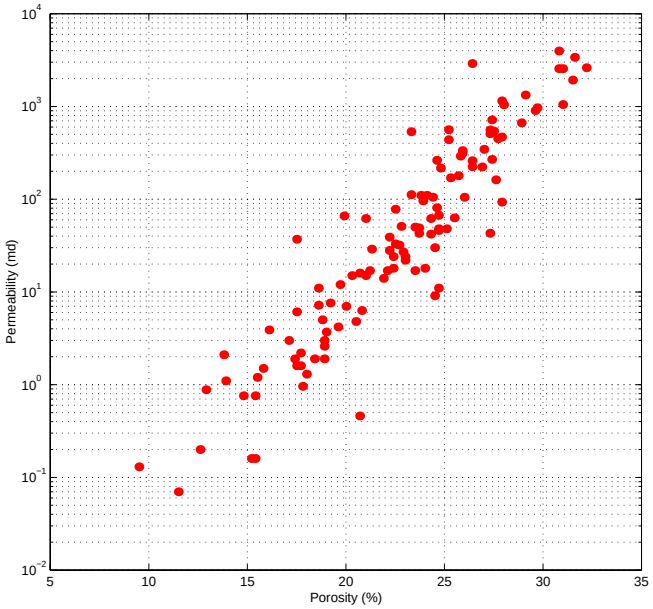

Figure 3.29. Permeability versus porosity in well 1882, Zone C sands.

3.4.3 Colorado Formation Reservoirs (Zone A)

The Colorado Formation is referred to as Zone A in the La Cira-Infantas field (Figure 3.30). The lower 150 m of Zone A consists of fine-grain sandstones interbedded with mottled shales. Above this is 210 m of gray, medium coarse sandstones with thin-bedded and blue to green shales. Overlying these beds are 170 m of gray and red mottled shales, with thin interbedded sandstones, followed by 180 m of brightly mottled shales and coarse grained sandstones, and finally overlain by 76 m of dark gray to black, well-bedded carbonaceous shales that contain brackish water fossils, the La Cira fossil horizon (Morales et al., 1958; Taborda, 1965; Dickey, 1992). Zone A totals approximately 786 m.

Gomez et al., (1999) suggest a deposition within fluvial meander belts and adjacent flooded areas for Zone A, with exception of the La Cira Shale interval, which ranges from 120 m to 200 m (Figure 4.30). They propose for this rich-organic black shale a sedimentary environment characterized by a wide flood basin, with slightly brackish lakes, swamps, and oxbow lakes.

In order to relate the elastic reservoir properties to porosity, mineralogy, pore fluid compressibility, and effective pressure in Zone A, modern high-quality well-log data from well La Cira 1879 are used, where core data are available as well. The log data span the depth interval from 120 m to 670 m with sands and shales represented in Figure 3.30.

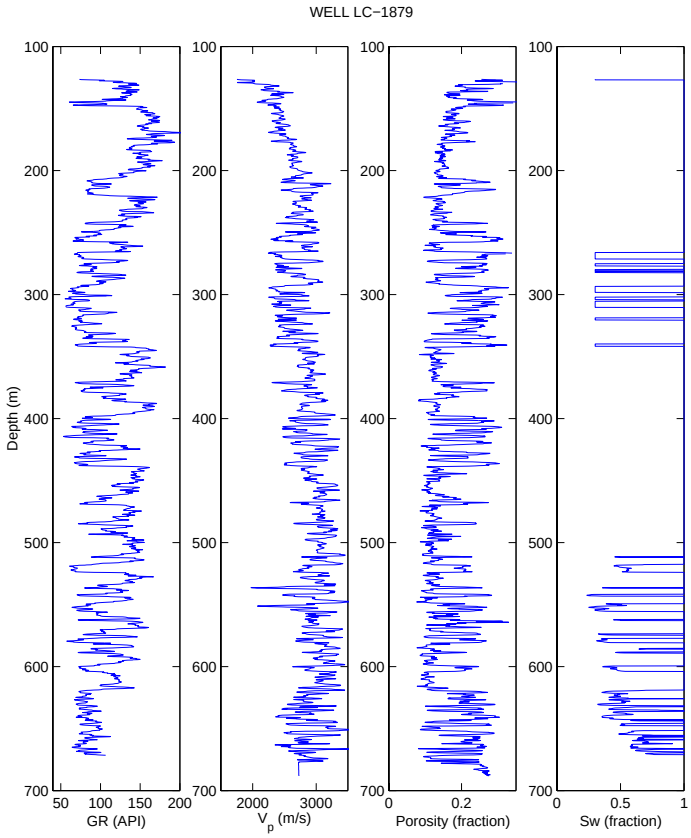

Figure 3.30: Well LC-1879, Zone A. Gamma-ray, P-wave velocity, density porosity, and water-saturation content curves.

First, the position of La Cira-Infantas sands in the rock physics space is identified by plotting velocity versus porosity for a major sedimentary cycle or sequence (Figure 3.31). This plot shows a pattern that resembles the "inverted V" pattern identified by Marion (1990) in uncemented mixtures of rigid (sand) and ductile (clay) granular materials (Yin et al., 1988). Marion identified two different trends in the porosity-velocity relationship; one for sandy shales, and one for shaly sands. The sandy shales trend is between the pure kaolinite mixture and the bimodal mixture of 60% Ottawa sand grains and 40% kaolinite. The shaly sands trend is between the 100% sands grain mixture and the bimodal mixture of sand grains and kaolinite (Section 3.3.3).

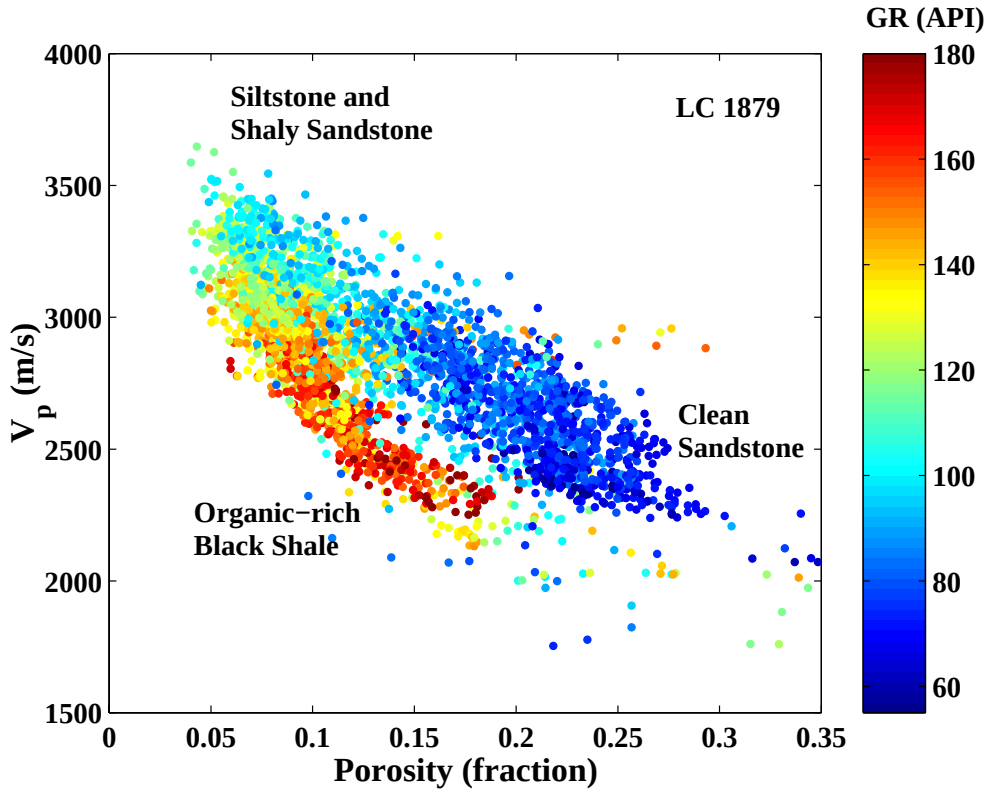

Figure 3.31: Well LC-1879, Zone A. Compressional velocity is plotted versus density-porosity. The colorbar indicates gamma ray values.

In Figure 3.31, the lower branch of the trend corresponds to the shallowest interval of Zone A, referred to as the La Cira Shale. This sedimentary unit is a rich-organic black shale with high GR values and, apparently, large clay content. The organic matter, important component of this black shale, is preserved in abundance in flood plain muds, lake bottoms and swampy areas (Blatt, et al., 1980). The upper branch of the trend corresponds to higher GR values and deeper intervals where sand starts to dominate. Lithology in this interval varies from clean high-quality, reservoir sandstones to low-quality reservoir siltstones and shaly sandstones. In contrast with the La Cira Shale, the lower sands and fine-grain units correspond to channels and overbank deposits. The mineralogical composition of these sandstones and siltstones is comparatively uniform, and the content of clay is relatively low in the fine-grain rocks (Section 3.3.2). The "inverted V" pattern presents a duality for the velocity-porosity relationship at the major sequence scale. Similar values of velocity correspond to very different values of porosity

and permeability. For example, 2500 m/s corresponds to low- and high-quality reservoir rocks.

Sedimentary rocks are not deposited randomly, but follow certain cyclic patterns in geological time and space (Section 3.4.1). If the geological position is taken in account, I can solve the velocity-porosity duality for Zone A. Figure 3.32 illustrates again the "inverted V" for Zone A, and the data points are colored by depth.

The lower branch corresponds to organic-rich black La Cira Shale and is located in the top of the sedimentary section. The upper branch is composed of the fluvial sands and shales underlying the transitional, probably estuarine La Cira Shale. This upper branch clearly is similar to the velocity-porosity trends in Zones B and C at the major cycle scale (Figure 3.25). In summary, to characterize the rocks in Zone A, every branch should be separated and study independently. After the separation of the La Cira Shale, the lower sands and shales can be analyzed following the same procedure applied to the underlying Zones B and C (Section 3.2.2).

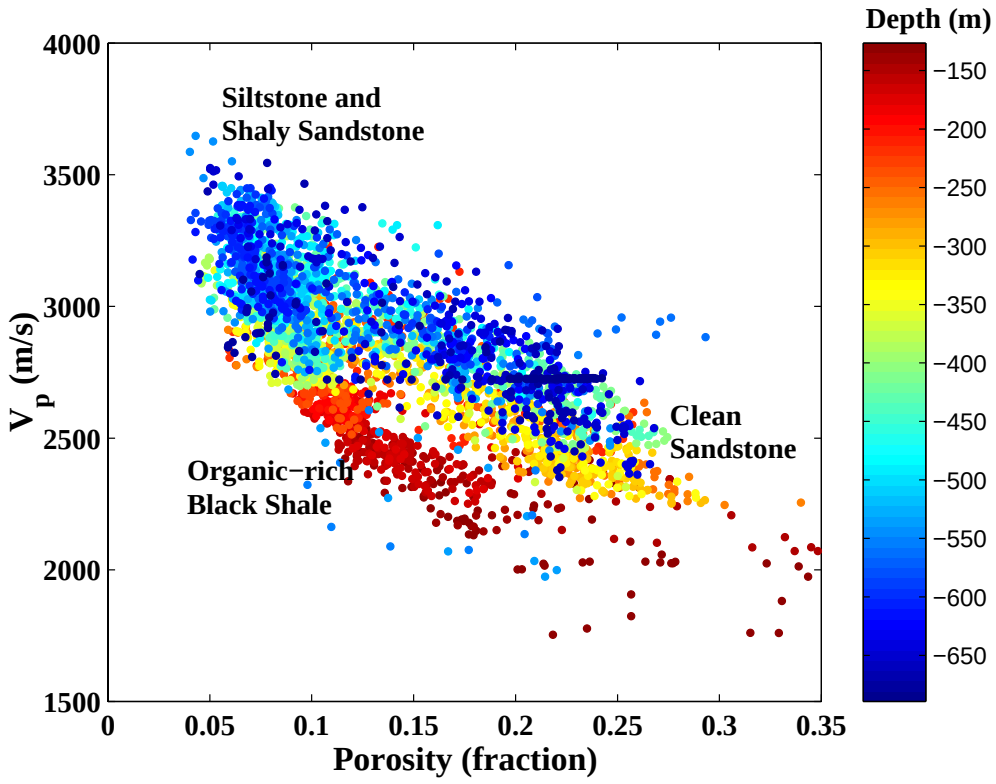

Figure 3.32: Well LC-1879, Zone A. Compressional velocity is plotted versus density-porosity. The colorbar indicates depth values.

Finally, I use the theory developed previously for the bimodal grain mixture in Section 3.3.3 to simulate the "inverted V" pattern founded in the well log data from well LC-1879 (Figure 3.33). The average bulk density is 2.36 g/cm^3. The pore fluid density is about 1 g/cm^3. Therefore, the differential pressure is about 1.7 MPa at the top and 9.4 MPa at the bottom of the interval, respectively. In order to model the effect of changing effective pressure, I used the model twice, with 2 MPa and 10 MPa differential pressure as input. Other inputs are:

$$\phi_{cl} = .3; \phi_{cs} = .2; n_l = 11; n_s = 14;$$
$$K_l = 37\ GPa; G_l = 45\ GPa; K_s = 21\ GPa; G_s = 8\ GPa; K_f = 2.5\ GPa.$$

As can be observed in Figure 3.33, the model results match very well the two trends in the velocity-porosity plot.

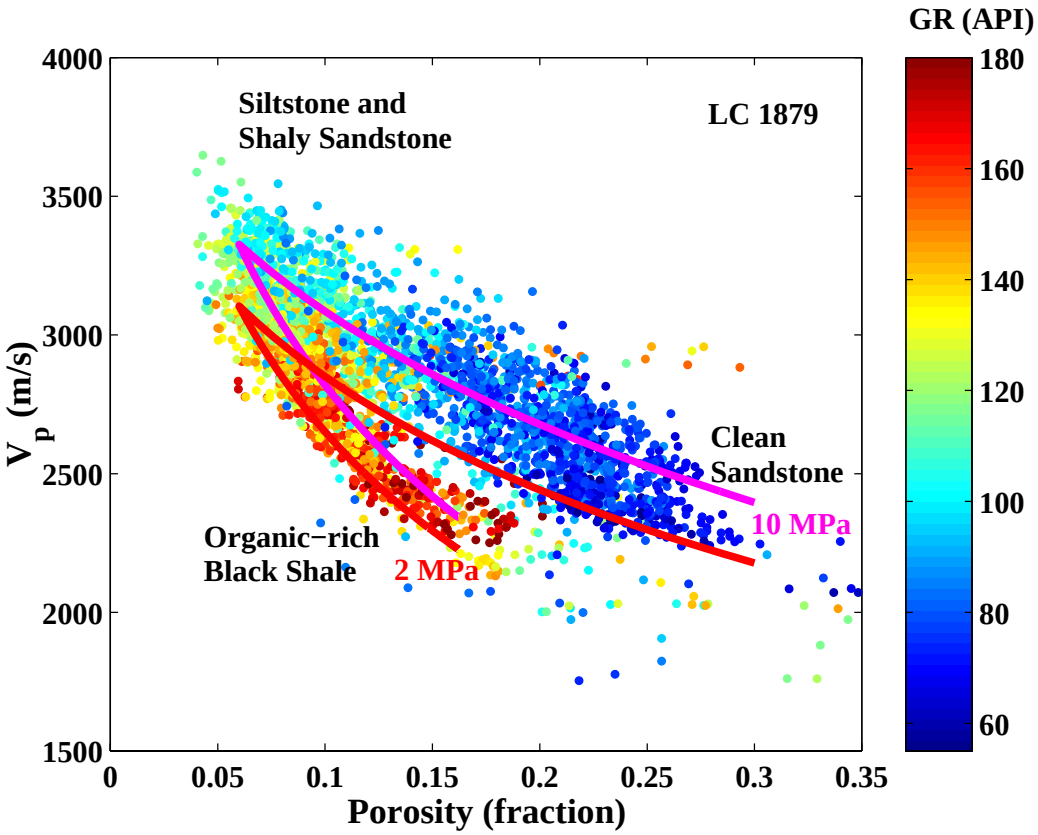

Figure 3.33: Well LC-1879, Zone A. Compressional velocity is plotted versus density-porosity. The colorbar indicates gamma ray values. Bimodal model curves are superimposed.

3.5 Seismic Imaging of Fluvial Reservoirs

This section presents a 3-D seismic analysis and mapping of fluvial heterogeneities and their flow units at interwell and fieldwide scale. Elements of interwell scale heterogeneity consist of lateral bedding geometries, styles, and continuity; and systematic lateral and vertical textural patterns. Constituents of fieldwide variability are reservoir thickness, facies geometries and continuity, and bulk reservoir properties (Slatt and Galloway, 1993). For this purpose, I have selected the northern part of La Cira-Infantas field, referred to as La Cira Norte (Chapter 2, Figure 2.18).

The development of 3-D seismology has given reservoir geologists and geophysicists a new tool to predict the geometry and quality of the reservoir away from well control and to choose in-field drilling targets in mature oil and gas fields with improved recovery efficiency. Although a few case histories of imaging fluvial deposits from 3-D surface seismic data have been published, the understanding of the relationship between the fluvial architectural elements and the seismic response is still deficient. Moreover, zonation in several flow units is a solid approach for modeling and predicting of reservoir performance.

Several field studies have used the flow unit concept, but most of these approaches are strictly qualitative, based on subjective predictions of lithofacies or depositional environments. However, this technique, although important, is only one-dimensional and therefore restricted to the wellbore domain. In addition, a 3-D quantitative mapping of the components of the reservoir sequence, including the flow units, is crucial to generate a realistic framework for reservoir simulation modeling.

Solving this problem is the core of this chapter. I determine the seismic response of the fluvial reservoirs and predict their reservoir quality. I will particularly focus on how the depositional facies and associated flow units at reservoir scale might be illustrated by 3-D surface-seismic data.

3.5.1 Fluvial Reservoirs

Fluvial deposits represent one of the most important non-marine environments in the stratigraphic record. Because ancient fluvial deposits are reservoirs for the accumulation

of hydrocarbons, they are of substantial economic significance. Much of the oil in the giant fields at Prudhoe Bay (Alaska), Statfjord (North Sea), Brent (North Sea), Daqing (China), and La Cira-Infantas (Colombia), is found in fluvial reservoirs (Miall, 1996; Dickey, 1992). These reservoirs are typically very heterogeneous, both vertically and laterally, which results in low recovery efficiency (Tyler and Finley, 1991).

Miall (1992) divided the fluvial deposits into four main levels of scale and complexity as follows: individual clastic facies, architectural elements, river systems, and basin scale deposits. Facies represent the primary mesoscopic heterogeneities in petroleum reservoirs. Architectural elements are assemblages of facies and represent the principal depositional features of fluvial systems. Architectural elements are the source of macroscopic heterogeneities.

At a somewhat larger scale, four river systems or fluvial channels are traditionally classified as meandering, braided, anastomosed, and straight (Miall, 1992; Emery and Myers, 1996). Variations at this scale generate macroscopic heterogeneities that directly affect the geometry of the reservoirs. Because fluvial channels are difficult to identify in the stratigraphic record, some investigators have suggested an alternative and practical system of classification based on grain size (Orton and Reading, 1993; Emery and Myers, 1996). River systems can accordingly be classified as follows: high-bedload (gravel), bedload (gravel and sand), mixed-load (fine-sand), and suspended-load.

Coarse and porous rocks that can be saturated with hydrocarbons are deposited within the channels and their related bar deposits. Therefore, an understanding of the architecture of the diverse classes of channel fill is crucial. For many years, petroleum geologists diagnosed the subsurface geometry of fluvial reservoirs using environmental interpretations.

Today, they accept that 3-D seismology is a powerful tool to image the geometry of the fluvial deposits, and even to accurately define reservoir heterogeneities (Miall, 1991, 1996; Selley, 1996). However, the traditional methodology for environmental and lithofacies prediction is invaluable and plays an important role during the process of integrating geophysical tools and geological criteria, especially in cases where the reservoir geometry is below the limits of resolution of the seismic method.

3.5.2 Seismic and Sequence Stratigraphy

Seismic stratigraphy is "basically a geologic approach to the stratigraphic interpretation of seismic data" (Vail et al., 1977). It relies on the identification of unconformity surfaces or sequence boundaries on seismic data, by genetically defining related packages or sequences of rocks (seismic sequence analysis). Within these sequences, variations of the seismic reflection characteristics can be interpreted in the context of depositional environment and lithofacies (seismic facies analysis). Every seismic facies can be examined in terms of the lateral variation of individual reflection events, or series of events, to locate and to determine the nature of changes in the stratigraphy or fluids in the pore space (reflection character analysis) (Bally, A. W., 1987; Sheriff and Geldart, 1995).

During the last two decades, seismic stratigraphy has developed into sequence stratigraphy as depositional characteristics that were first seen and understood in seismic data have been recognized in outcrops and in well-log data. The theory underlying sequence stratigraphy is that sediment deposition is governed by four elements: accommodation, sediment inflow, eustasy, and climate (Wilgus et al., 1988; Van Wagoner et al., 1990; Weimer and Posamentier, 1993). Sequence stratigraphy provides a detailed chronostratigraphic framework for exploration and reservoir management, including the evaluation of hydrocarbon potential and location of by passed oil in producing fields. Depositional facies are considered to have the primary control on sandstone reservoir architecture and porosity distribution unless diagenesis and erosion have occurred. For the loosely consolidated siliciclastic reservoirs in La Cira-Infantas, facies are also an important component in resolving hydrocarbon flow units due to the direct relationship between porosity and permeability. 3-D seismic techniques make it possible to predict the reservoir geometry and quality away from the well control.

Rock physics relationships between elastic properties and reservoir properties established previously in Section 3.4 suggest that the prediction of the lithology and the mapping of the reservoir quality in fluvial reservoirs using acoustic impedance and velocity inverted from P-wave seismic data is feasible. In order to describe the reservoir heterogeneities, I link the rock physics properties of the fluvial deposits and the seismic response of 3-D P-wave data available in La Cira-Infantas.

3.5.3 Seismic Inversion

For this part of the study, the northern part of the La Cira-Infantas field, referred to as La Cira Norte, was selected. The reasons for this selection were (a) the good quality of surface seismic, (b) simple geologic structure, and (c) the availability of well logs in numerous wells in La Cira Norte. The approach to delineating good quality reservoirs is based on linking the reservoir properties to a seismic observable—impedance or velocity (Section 3.4). Once this rock physics link or transform is established, three-dimensional impedance and/or velocity volumes of the subsurface are needed to which this transform can be applied. In order to create an impedance/velocity volume from surface seismic, a model-based inversion technique is used (Figure 3.34). The method operates by generating a forward model that best mimics the seismic surface data when converted to synthetic form. The method involves starting with a straightforward estimate of this model and changing this estimate until the error between the model and the observed seismic data is minimized (Russell, 1988).

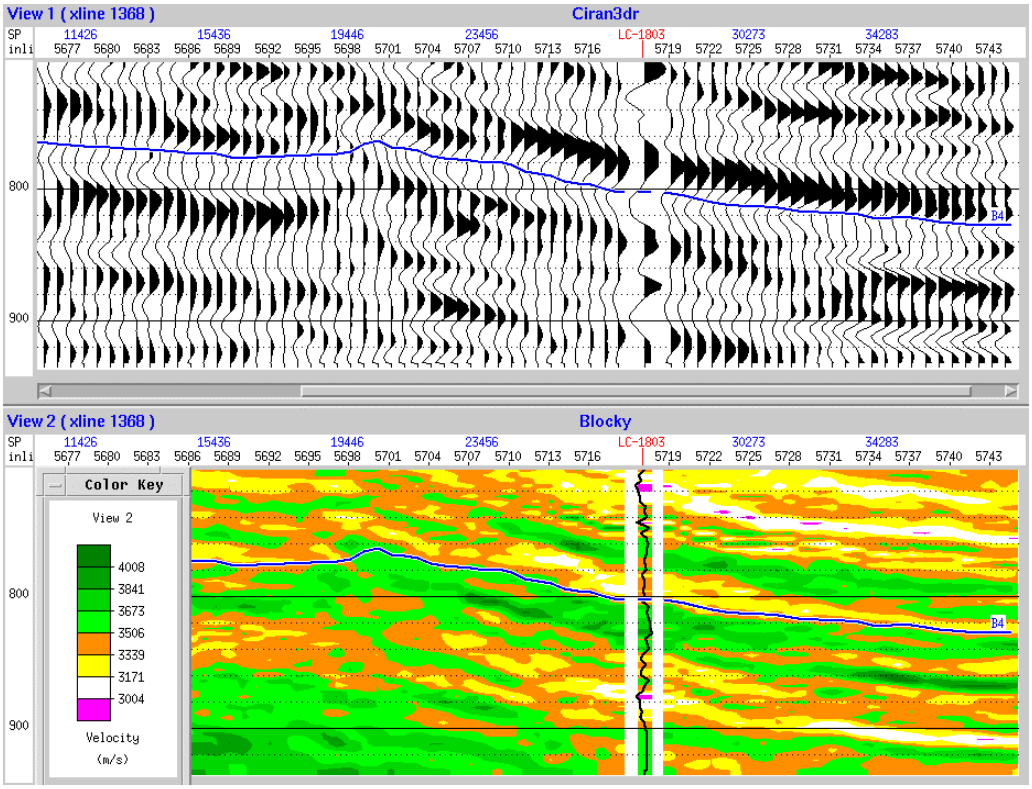

Figure 3.34: Original seismic trace display (top) and velocity profile (bottom) obtained from the seismic inversion. Color key shows compressional velocity.

Seismic Impedance Volume–Practical Implications

In order to build an impedance volume, the algorithm requires an initial velocity model; in this case, sonic logs available for several wells were used, since no other sources for velocity models exist. This approach immediately results in a limitation in the extent of velocity/impedance volumes to be obtained: most of the wells with sonic logs in La Cira Norte are logged in their bottom part within the lower portion of Zone B and the upper part of Zone C. Therefore, the interpretation is focused only on the parts of the reservoir where sonic logs are available. Another limiting factor is the fact that sonic logs must be matched with the adjacent seismic traces. Sometimes this match is impossible to achieve. Therefore, it is necessary to decide which information is more reliable: seismic or sonic data. Seismic data was selected as most reliable. As a result, the wells where it is impossible to achieve a good match with seismic traces were discarded. Four main assumptions were made when creating velocity/impedance volumes:

- A sonic tool is most likely to record velocities in a zone that has some mud filtrate invasion. On the other hand, a far-resistivity tool allows us to estimate saturation in the virgin formation. In the case, resistivity data are not available in the invaded zone. Therefore, the first assumption (which is partly incorrect) is that the sonic and resistivity tools give us information about the same volume of the rock.
- The wells in La Cira Norte were logged some time before the seismic survey was conducted. During this period of time changes in reservoir fluid distribution due to production were likely to occur. In general, seismic and sonic data sample, rocks with different fluids. Therefore, the second assumption, which is also partly incorrect, is that the sonic and seismic data describe rocks with the same pore fluid.
- In this inversion it is assumed that all traces are from normal incidence waves. By so doing the AVO effects related to fluid and lithology changes between layers are neglected.
- Finally, in the wells with sonic logs, density logs are not available, and the direct calculation of impedance in these wells is not possible. Therefore, the third assumption is that the bulk density can be calculated from sonic velocity using Gardner's equation:

$$\text{RHOB (g/cm}^3\text{)} = 1.741\ V_p^{0.25}\ \text{(km/s)}. \tag{3.33}$$

Stratigraphic Interpretation

The basic geological assumption made in the seismic interpretation is that seismic reflections follow chronostratigraphic depositional surfaces (Vail et al., 1977). This assumption means that if a continuous seismic reflector is picked over the entire La Cira Norte area, a permanent depositional time or depositional strata surface is defined.

One areally continuous seismic marker identified as B4 was selected. This marker is located in the top of a major fining-up cycle between the operational Zones B and C (Figure 3.34). Now, the structural component is removed from the sedimentary sequence, flattening the 3-D velocity volume relative to the B4 marker or reference strata surface. Consecutive strata slices starting below B4 (B4 plus 140 ms) and ending in the datum marker B4, show the evolution from a braided stream channels system at the base to a meandering fluvial channels system at the top. Straight channels are clearly delineated at the base of the sequence (Figure 3.35), whereas complex meander deposits are described at the upper level of the C sands (Figure 3.36). Yellow color here corresponds to low velocity (sands) and green color is for high velocity (shales). This seismic interpretation of the reservoir architecture agrees with local (Laverde, 1996) and regional stratigraphy studies (ICP-ECP, 1996).

These recent sequence stratigraphy analyses, based on the description of La Cira-Infantas cores and outcrop data, indicate that depositional facies of La Cira-Infantas Tertiary rocks are associated with fluvial channel systems. Zones A and B represent mixed load channels or meandering systems, in contrast with Zone C, which was deposited as bed load channels or braided stream systems.

3.6 Reservoir Quality from Seismic Data

Reservoir quality of a rock is defined by its porosity and permeability. The spatial distribution of the reservoir is one of the main uncertainties in hydrocarbon exploration and production. 3-D seismology is the most efficient tool to study reservoir heterogeneities and the reservoir quality at the interwell and field scale. In order to predict the reservoir quality from seismic data in La Cira-Infantas, initially a small volume of seismic surface data was converted into a volume of the reservoir's elastic properties in Section 3.5.3.

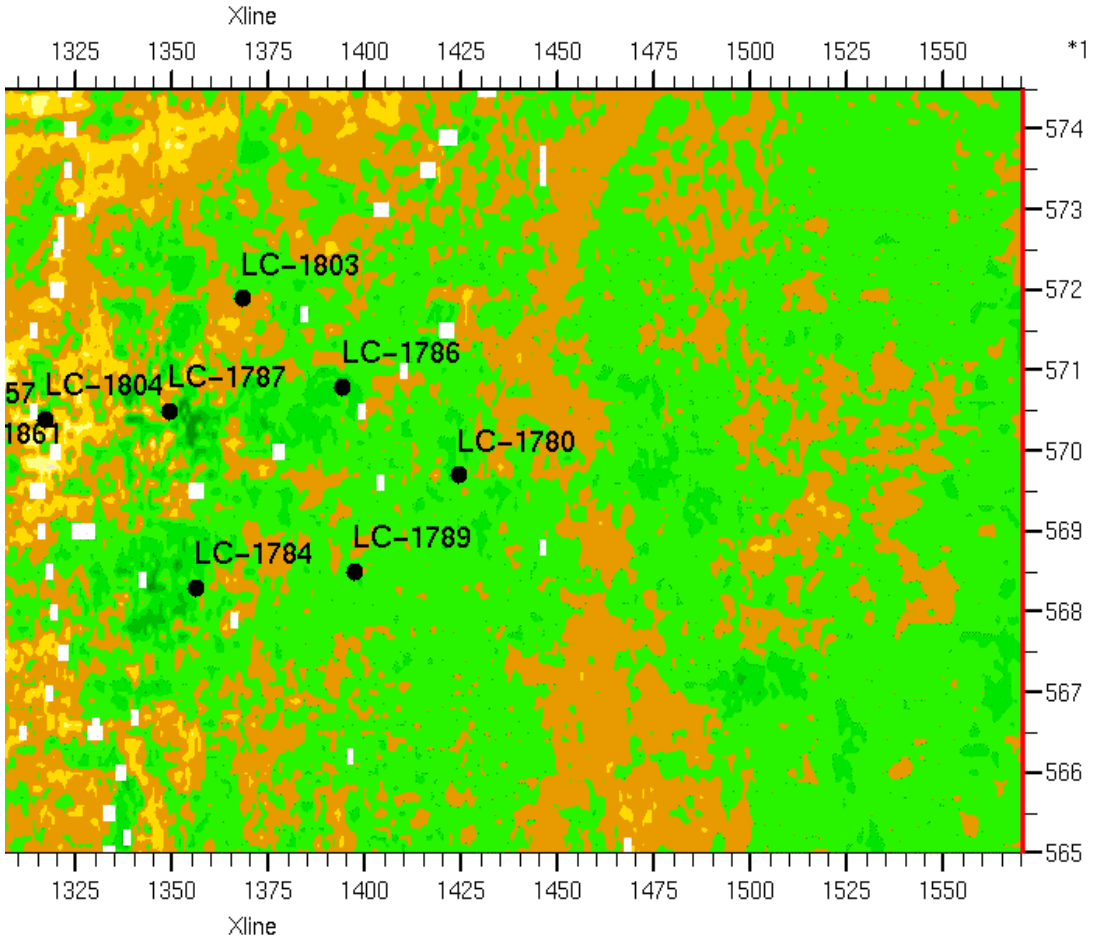

Figure 3.35: Inversion velocity on a strata slice in the vicinity of B4 plus 100 ms. A straight channel is clearly delineated east of well LC-1780.

The La Cira-Infantas rock physics model developed in Section 3.4 relates the elastic reservoir properties to porosity, mineralogy, pore fluid, and differential pressure, using the stratigraphic framework as a constraint. The model implies that velocity and acoustic impedance are reliable reservoir quality discriminators. Specifically, high velocity and impedance correspond to shales whereas low velocity and acoustic impedance indicate high-quality sands.

That section also shows that rock quality in the diagenetically simple reservoirs of La Cira-Infantas can be related to environmentally restricted depositional parameters, such as rock texture and framework composition. The rock physics model established in section 3.4 will serve as the basis for interpreting seismic data for reservoir quality and the presence of hydrocarbons in the high-resolution stratigraphic cycles (Chapter 4).

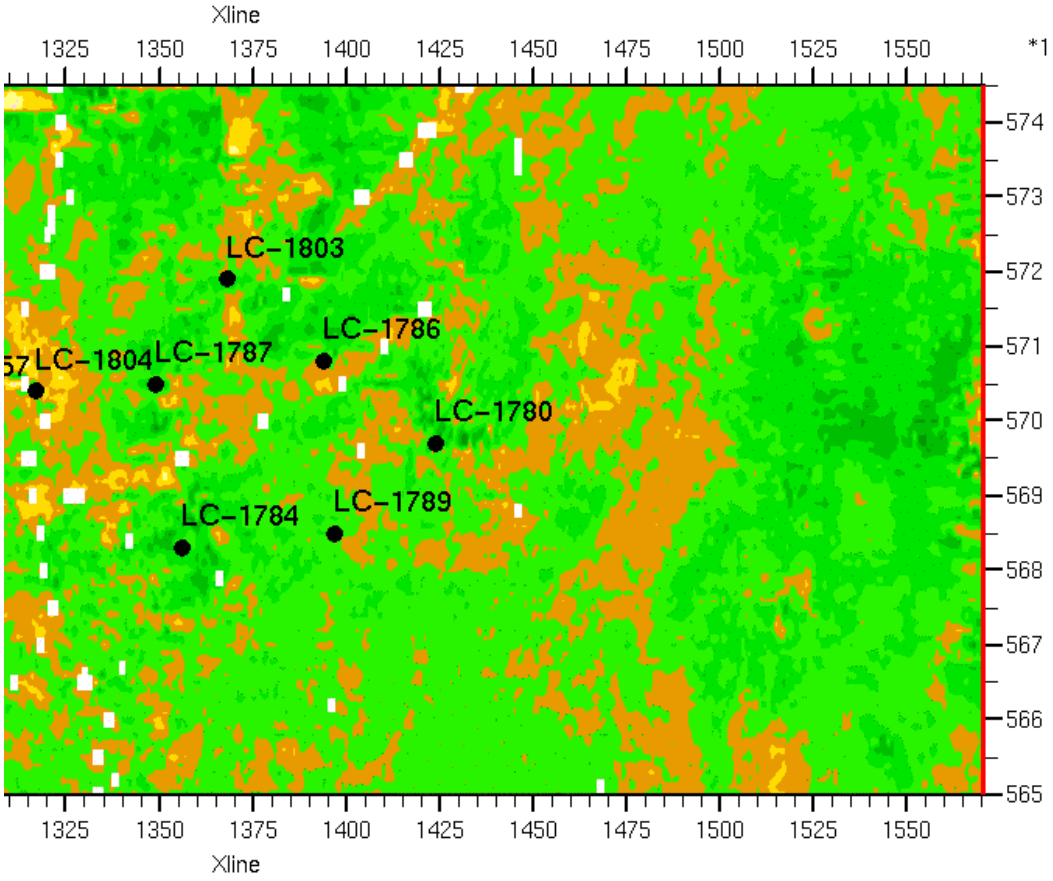

Figure 3.36: Inversion velocity on a strata slice in the vicinity of B4 plus 35 ms. A meandering fluvial channels system is visible.

3.6.1 Summary of Effects on Reservoir Quality and Elastic Properties

Section 3.3 illustrates the different physical and geological variables that influence both reservoir quality and elastic properties. Because a good correlation exists between porosity and permeability for the loosely consolidated sandstones in La Cira-Infantas (Figure 3.29), predicting reservoir quality is straightforward. Sandstones that exhibit high porosity exhibit high permeability. Once porosity values are established, it will be uncomplicated to estimate permeability in La Cira-Infantas. Using multiple and schematic cross-plots, where the rock elastic property is plotted versus reservoir quality, the effects of the main variables that affect reservoir quality and elastic properties in La Cira-Infantas rocks are summarized as follows.

The necessary relations between acoustic impedance and reservoir properties were determined from well log and core data where all rock attributes are measured at the same time on the same rock sample (Section 3.4). These relations were rationalized and explained by effective-medium models. The key to obtaining such models is consistency between the reservoir's sedimentological characteristics (e.g., texture and composition), well log data (e.g., GR), and core analysis (e.g., porosity and velocity).

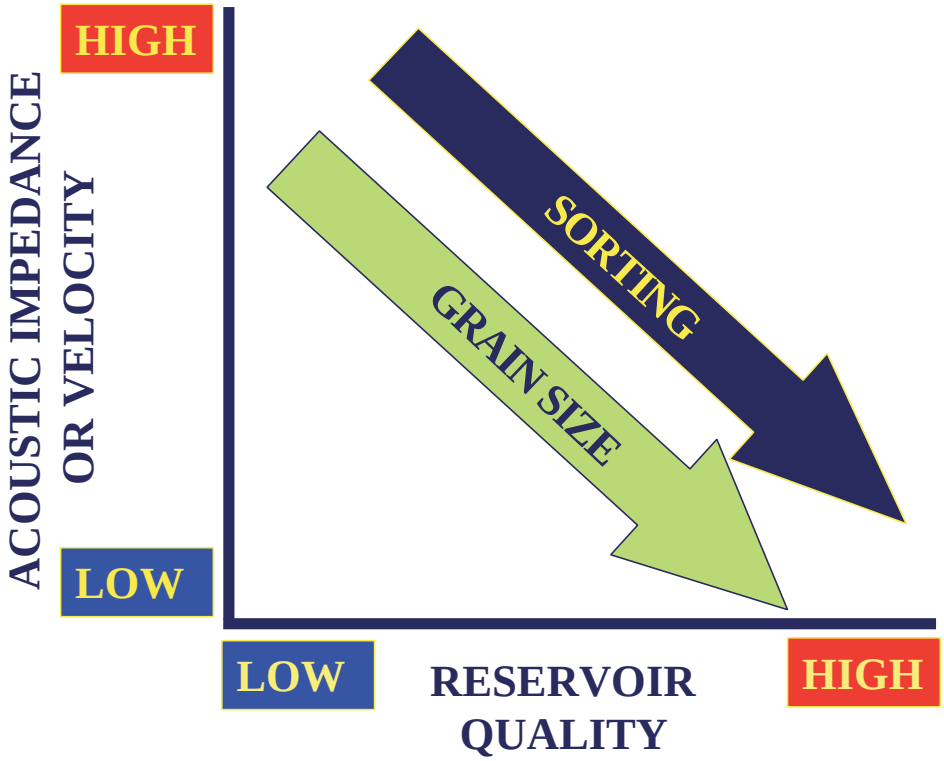

Figure 3.37: Effect of sorting and grain size on acoustic impedance and reservoir quality.

Figure 3.37 illustrates the effect of textural sorting and grain size. If the rock framework is mechanically stable, well-sorted clastic rocks with a simple diagenesis will exhibit better reservoir properties and lower elastic velocities than poorly-sorted clastic rocks. Similarly, very fine grain rocks will show low reservoir quality and high velocity and impedance. In contrast, fine and medium grain sands show high reservoir quality and low velocity and impedance (Section 3.3).

Laboratory experiments and field data also show a velocity increase that pairs with a reservoir quality reduction when rocks are poorly sorted. In this particular situation, the deterioration of grain sorting results in a more efficient packing thus causing the rock

matrix to stiffen, the velocity or acoustic impedance to increase, and the reservoir quality to decrease (Figure 3.38).

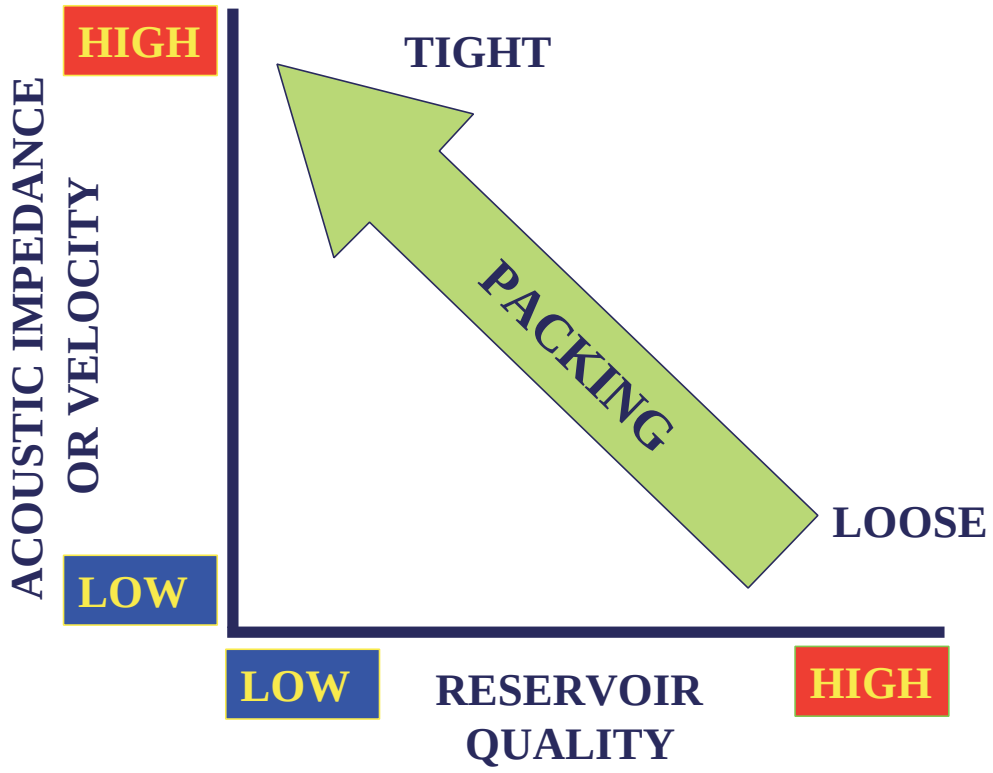

Figure 3.38: Effect of grain packing on acoustic impedance and reservoir quality.

Reservoir quality is not an exclusive function of rock texture. Composition and the relative content of detrital mineral components in clastic rocks also play an important role in the mechanisms of reservoir quality reduction, such as mechanical compaction. Figure 3.39 shows the effect of rigid grain content. Sandstones with a high content of mechanically-rigid grains are most likely to preserve high porosities and permeabilities after mechanical compaction, thus causing the rock matrix to soften, the velocity or acoustic impedance to decrease, and the reservoir quality to increase.

The combined effect of sorting and composition is illustrated in Figure 3.40. The plot shows schematically the typical trends under compaction of two clastic rocks at the low stage of textural maturity. As previously illustrated, the rigid framework is very stable and minorly reduces the reservoir quality (green arrow).

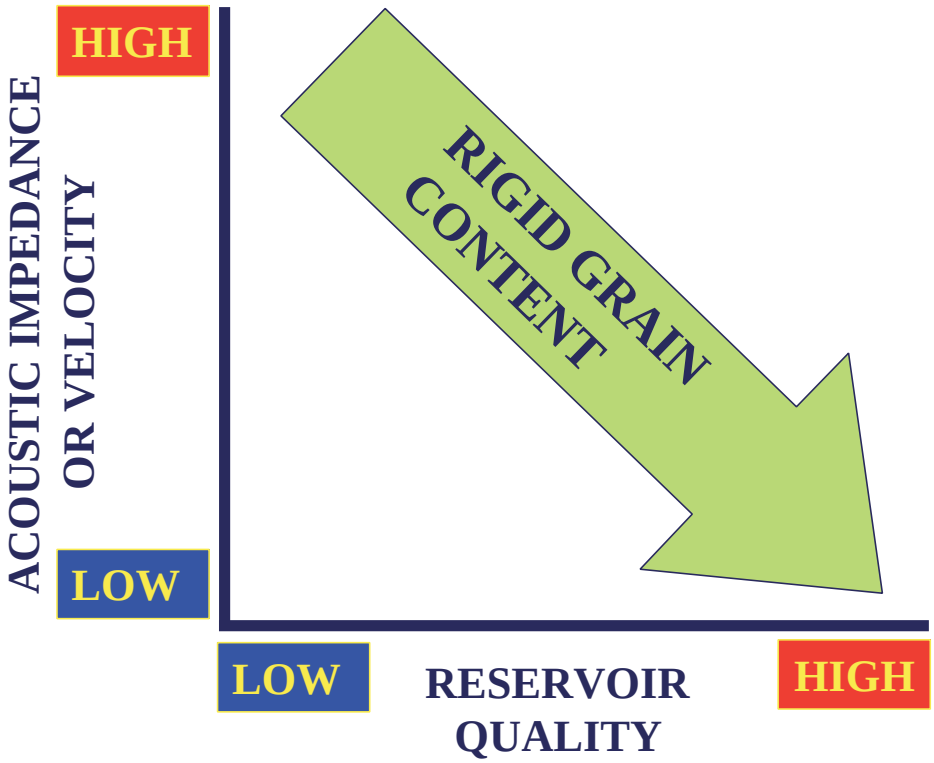

Figure 3.39: Effect of rigid grain content on acoustic impedance and reservoir quality.

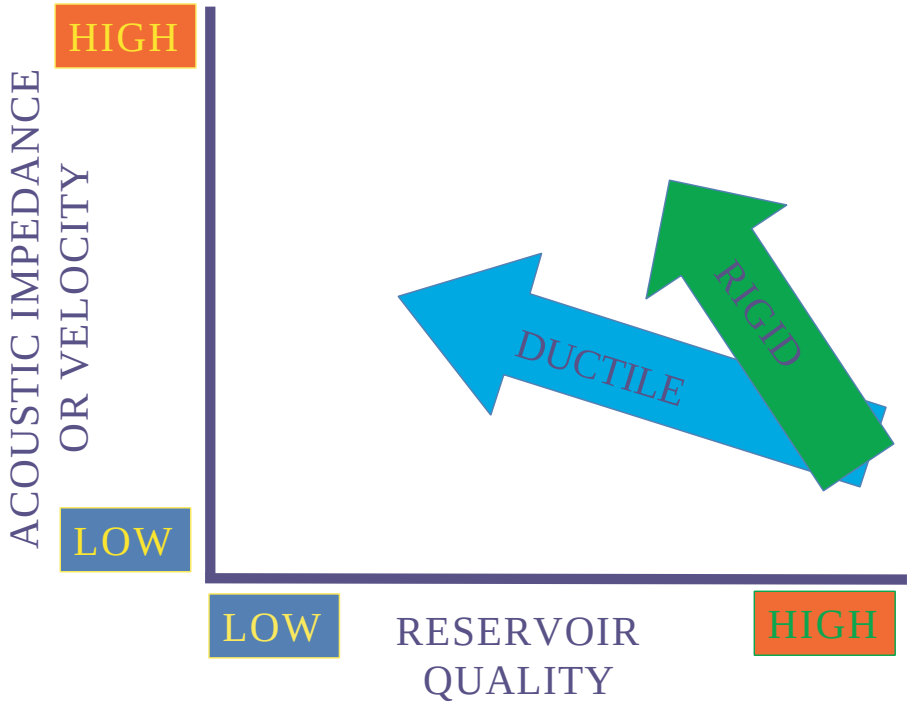

Figure 3.40: Combined effect of texture and composition on acoustic impedance and reservoir quality.

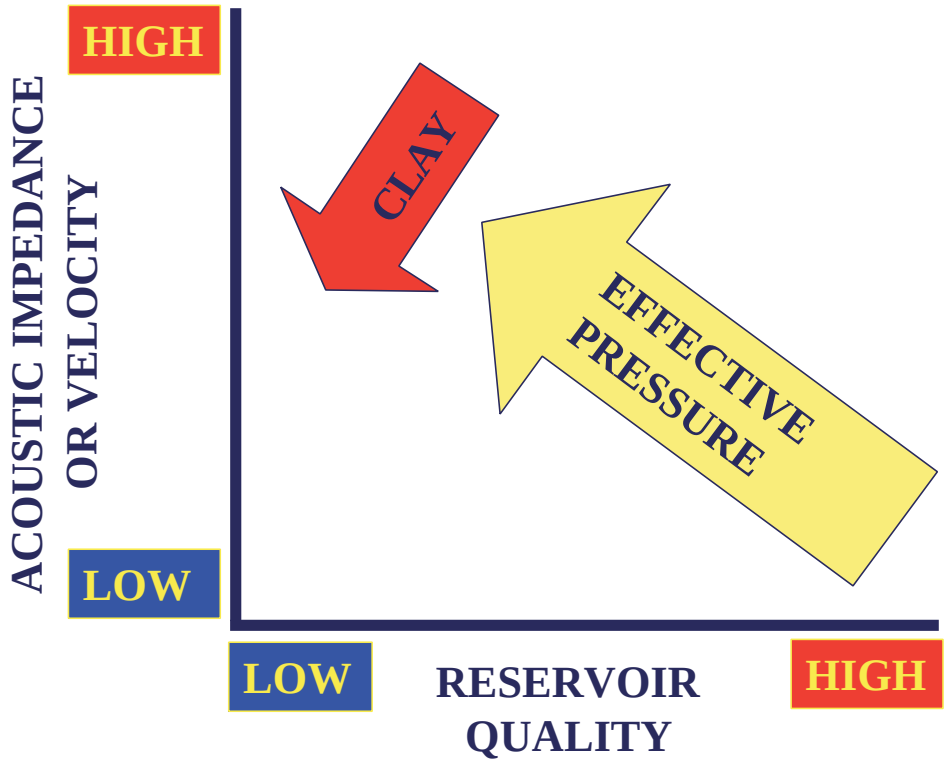

Figure 3.41: Clay mineral and effective pressure effects on acoustic impedance and reservoir quality.

In contrast, the presence of ductile grains reduces the stability of the framework, increases the compaction rate, and drastically reduces the reservoir quality (blue arrow). Existing velocity-porosity models, laboratory, and field data show that an increase in clay content decreases the sandstone's velocity, impedance, and its reservoir quality. Similarly, an increase in effective pressure reduces the reservoir quality and increases the sandstone's velocity and impedance (Figure 3.41).

Type of Deposit Mapping

River systems can be classified as high-bedload (gravel), bedload (gravel and sand), mixed-load (fine-sand), and suspended-load (Orton and Reading, 1993; Emery and Myers, 1996). These river systems can be mapped and directly related to the quality of the reservoirs, using the acoustic impedance volume and the rock physics relationships

developed in Section 3.3. Suspended load deposits, associated with very fine grain rocks, show very low reservoir quality and very high velocity and impedance. Mixed-load deposits, associated with fine sands, show moderate porosity and velocity and impedance. In contrast, bedload deposits, associated with medium and coarse sandstones indicate high reservoir quality and low velocity and impedance (Figure 3.42).

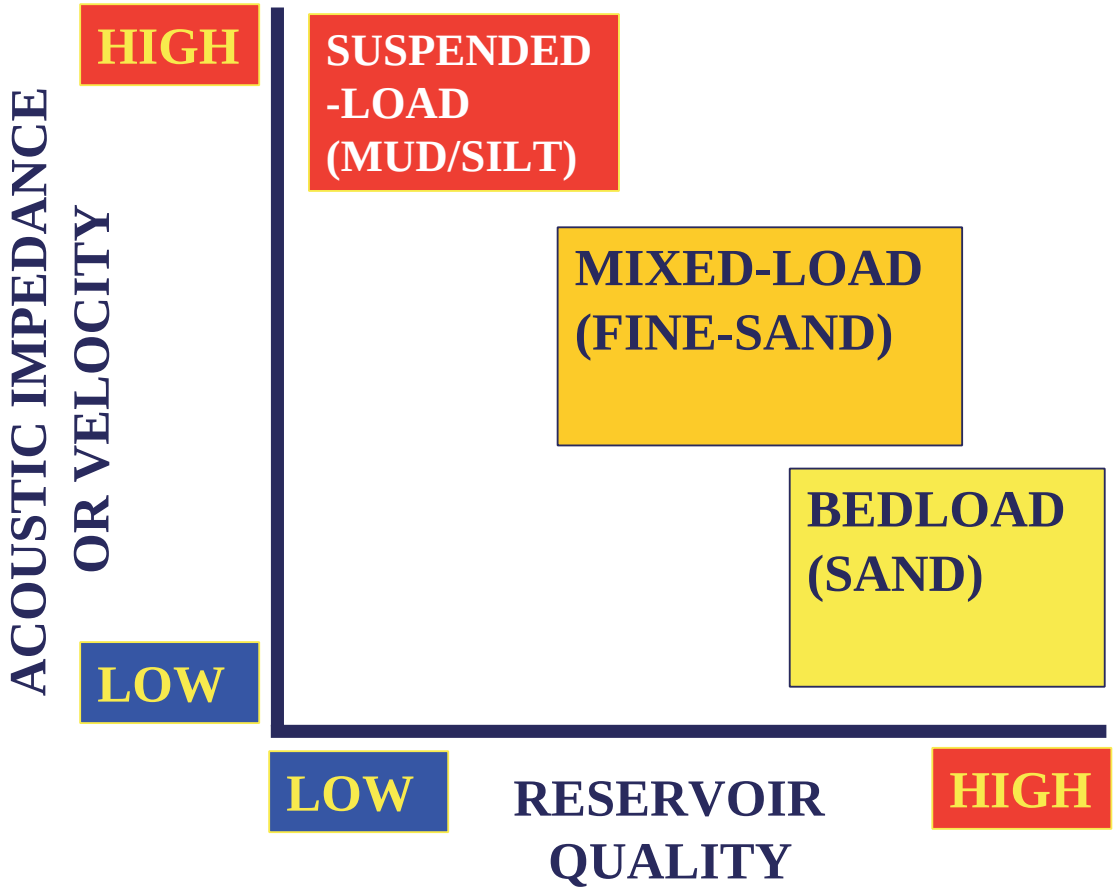

Figure 3.42: Relationship between the type of fluvial deposit, reservoir quality, and acoustic impedance.

Flow Unit Mapping

Reservoir geologists and hydrologists have recognized the necessity of characterizing geological and petrophysical units to formalize their descriptions of rock strata as storage containers and pathways for fluid flow. Maxey (1964) proposed the inclusion of the term *hydrostratigraphic unit* into the Code of Stratigraphic Nomenclature to satisfy this need. Other designations that have been introduced include *reservoir facies* (Lansgton and

Chin, 1968), *reservoir unit* (Pettijohn et al., 1973), *flow units* (Hearns et al., 1984; Ebanks, 1987), and *lithohydraulic unit* (Krause et al., 1987). Hearns et al., (1984) were the first to use the term *flow unit*, defined as "a reservoir zone that is continuous laterally and vertically, and has similar permeability, porosity and bedding characteristics."

A few years later, the flow unit concept was formalized and presented by Ebanks (1987) and was slightly modified again by Ebanks et al. (1993). They define the flow unit as "a mappable portion of the total reservoir within which geological and petrophysical properties that affect the flow of fluids are consistent and predictably different from the properties of other reservoir rock volume". Moreover, Ebanks et al. (1993) characterize the flow unit as a specific volume of a reservoir, which is composed of one or more reservoir-quality lithologies and any nonreservoir-quality rock types within that same volume, as well as the fluids they contain. A flow unit is recognizable on wireline logs, and correlative and mappable at the interwell scale. It may be in communication with other flow units.

Reservoir engineers usually have serious problems in their numerical models for simulating reservoir behavior, including geological heterogeneities. Zonation of a reservoir into several flow units is a solid approach for modeling and predicting performance. This permits more quantitative delineation and mapping of the components of the reservoir sequence that are most significant to reservoir behavior.

This approach generates a realistic framework for constructing reservoir simulation models, and is thus an objective reservoir zonation to be used in numerical simulation of reservoir performance (Weber et al., 1990; Hearns et al., 1984). A number of field studies have used the flow unit or a similar concept (Sneider et al., 1977; Hearns et al., 1984; Krause et al., 1987; Rodriguez, 1988; Slatt and Hopkins, 1990; Montgomery, 1991; Hamlin, et al., 1995). However, most of these approaches are strictly qualitative, based on subjective predictions of lithofacies or depositional environments.

The qualitative seismic mapping of the reservoir flow units is possible for fluvial loosely consolidated sandstones, based on the good relationships between acoustic impedance, reservoir quality, and flow unit discriminators (porosity and permeability). Seals, associated with very fine grain rocks, show very low reservoir quality and very

high velocity and impedance. Baffles, associated with fine sands, show moderate reservoir quality, velocity, and impedance.

In contrast, the flow units classified as speed zones, related to medium and coarse grained sandstones, show high reservoir quality, and low velocity and impedance (Figure 3.43). Moreover, a seismic physical attribute, in principle, can be converted into a volume of flow units, if the elastic properties are related and integrated with the borehole-restricted and quantitative approaches used by petrophysicists, such as Flow Zone Indicator (Amafule et al., 1993) and Winland's equation (Gunter et al., 1997).

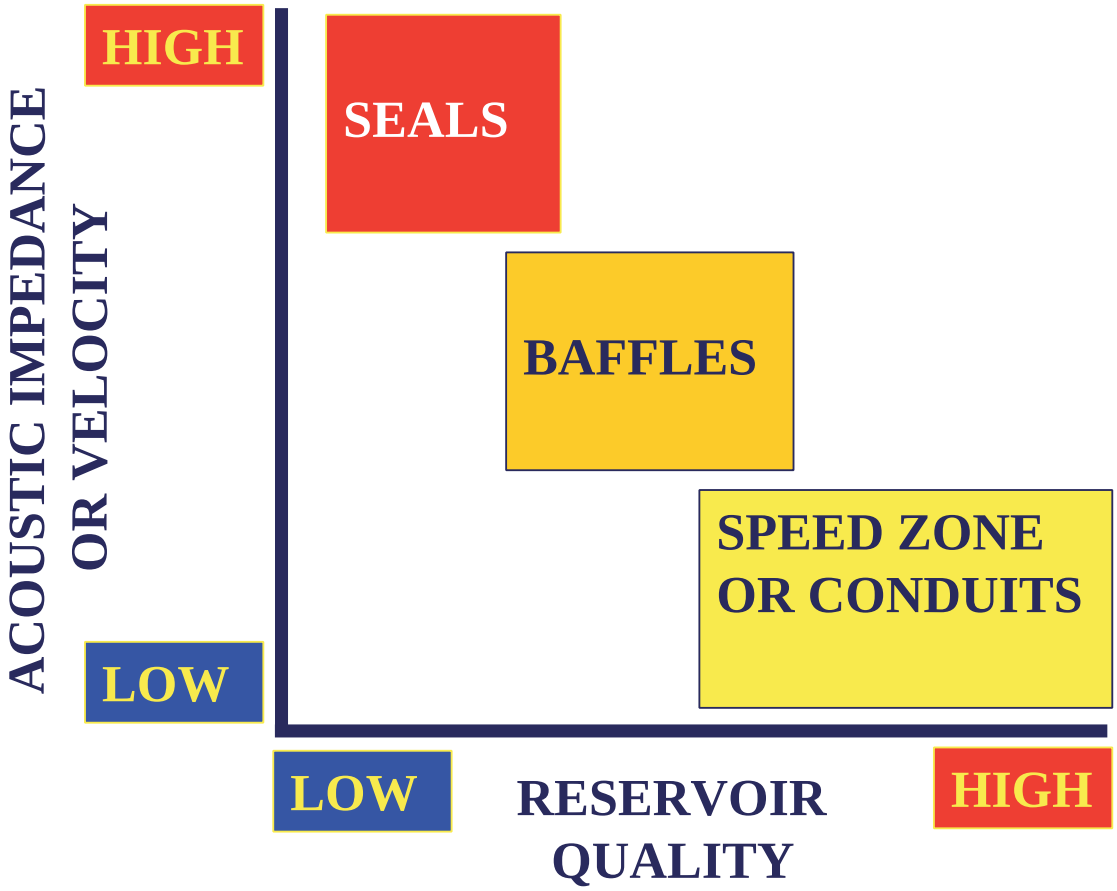

Figure 3.43: Relationship between the type of flow unit, reservoir quality, and acoustic impedance. Flow unit terminology from Gunter et al. (1997).

Reservoir Quality Prediction

Figure 3.44 shows strata slices of (a) reflection amplitude and (b) P-wave impedance. The images are based on the high-quality 3-D surface seismic data obtained at the northern part of La Cira-Infantas, or La Cira Norte. The impedance are from seismic inversion (Figure 3.36). The two-color impedance display clearly shows low-impedance channel sands (yellow) encased in high-impedance shaly flood plain (green).

P-wave impedance can confidently relate to the reservoir quality because my rock-physics analysis of the Tertiary fluvial deposits in La Cira-Infantas show that high velocity and acoustic impedance correspond to shaly intervals and low velocity and acoustic impedance correspond to clean sands.

The model developed here can be used to quantitatively relate the impedance to porosity. The seismically generated porosity volume will have a vertical resolution of tens of meters. The reliability of identifying hydrocarbons in situ will increase if the shear-wave data (offset reflectivity or elastic impedance) are available (Chapter 4).

In summary, using impedance (both acoustic and elastic) inversion results appears to be crucial for reservoir characterization because the rock physics transformations between velocity, porosity, and mineralogy cannot be immediately applied to the reflection data. At the same time, they can be directly applied to impedance inversion data for interpreting these data in terms of reservoir quality, i.e., porosity and clay content. Moreover, the porosity-permeability transformation shown in Figure 3.29 allows one to estimate permeability from impedance inversion.

There are several assumptions embed in the seismic interpretation process that introduces uncertainty to the estimates of reservoir quality. Because the integrated approach proposed in this study is based on solid geological and physical concepts there is some reduction in the degree of this uncertainty. However, there are important assumptions associated with the manipulation (acquisition, processing, and inversion) of the seismic data, and the integration of diverse datasets from different scales and origins, that remain in the interpretation process and add uncertainty to the final predictions.

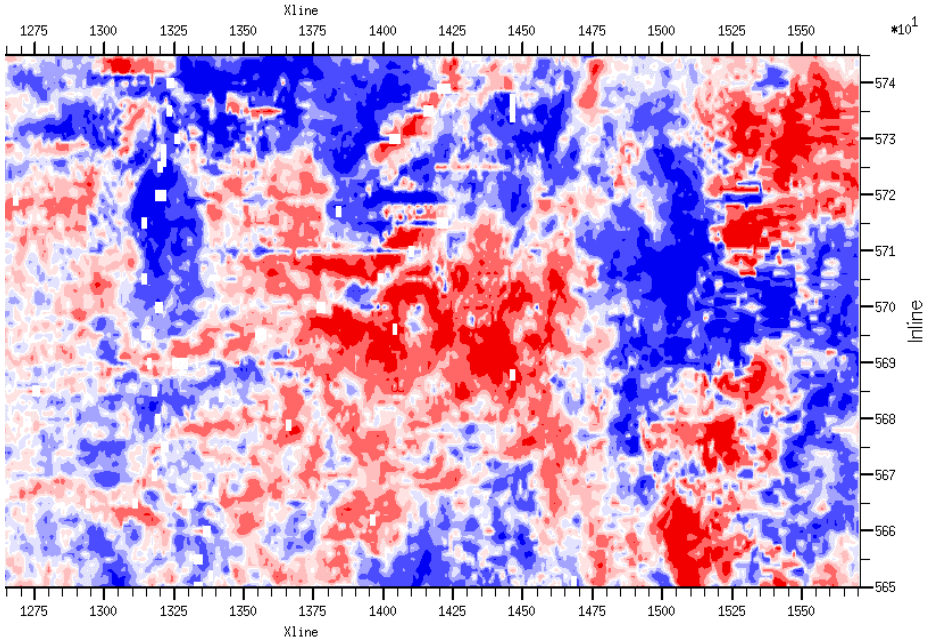

Figure 3.44 (a): Conventional amplitude display on a strata slice in the vicinity of marker B4 plus 35 ms.

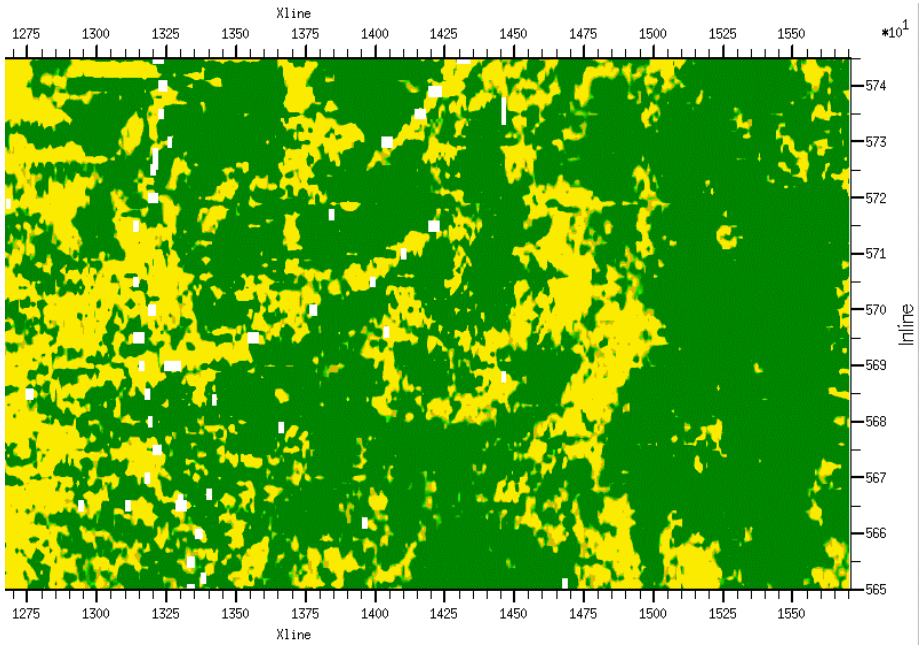

Figure 3.44 (b): P-wave impedance display on a strata slice in the vicinity of marker B4 plus 35 ms. Yellow color corresponds to low-impedance velocity sands and green color is for high-impedance shales. A meandering fluvial channel system is visible. The 2-color display is used to enhance the visibility of the depositional features.

The general procedure to seismically predict the reservoir quality is summarized in Figure 3.45. If the target area is under exploratory and appraisal activities, where the principal reservoir information comes from a few wells and a seismic volume, the application of the geology-constrained rock physics approach proposed in this chapter can provide important diagnostic estimates of the reservoir quality. These estimates include sedimentary trends, rock types, flow units, and rock properties at relatively low vertical resolution (seismic scale). On the other hand, if the target area is under development, the relevant reservoir information comes from seismic data and several wells, and estimates of the reservoir quality at high-vertical resolution can be obtain with the inclusion of geostatistics in the proposed approach.

Geostatistics is a useful tool to quantify and model spatial variability, including scales of heterogeneities and direction within the datasets (Chambers et al., 2000). The principal role of geostatistical techniques to improve the reservoir quality prediction rest in data integration, mix diverse information accounting for uncertainty, and reassign such uncertainty into the final forecast (Journel, 1994). Geostatistical techniques such as stochastic simulation constrained by seismic data can provide detailed reservoir models at the required scale for reservoir simulation studies (Helgesen et al., 2000).

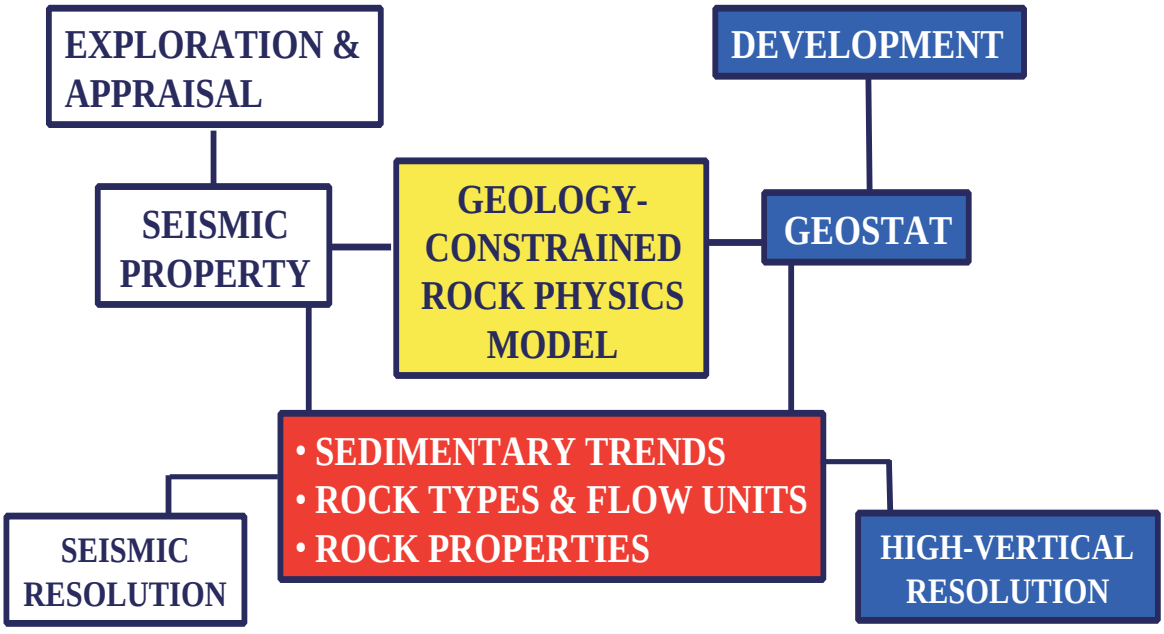

Figure 3.45: General procedure for seismic reservoir quality prediction.

3.7 Conclusions

Meaningful rock physics relations can be determined if subsets of log and core data are constrained by a sequence stratigraphy framework. These relations can be rationalized and explained by effective-medium models. The key to obtaining such models is consistency between reservoir sedimentological characteristics, well log data, and core analysis.

By analyzing well logs and core data, a governing effective-medium-based rock physics model was determined. Rock physics analysis and modeling in Tertiary fluvial deposit shows that velocity and acoustic impedance are reliable reservoir quality discriminators. High velocity and acoustic impedance correspond to shales while low velocity and acoustic impedance indicate high-quality sandstone reservoirs.

The principal distinction between shaly zones and sandy zones in La Cira-Infantas is porosity rather than clay content. Shaly zones are made out of silt and therefore have low porosity and very low permeability. By analyzing the inversion-velocity strata slices obtained from 3-D surface seismic data in the La Cira-Infantas oil field, it is possible to describe the geometry of productive sandy intervals and water-saturated shaly zones.

The general importance of the rock physics modeling is that it goes beyond pure statistical correlation, and therefore allows for generalizing the observed trends and applying them with confidence to the entire field. The new set of relationships for fluvial rocks in La Cira-Infantas is the essential rock physics framework to create pseudo-logs, and to predict and to map rock properties, such as lithology, porosity, and porosity-related properties (permeability, pore fluids, etc.) using seismic data.

Rock physics and stratigraphy-based interpretation of P-wave seismic data is a promising methodology for the detection of depleted, bypassed, and untapped reservoirs and deeper pools in mature fields such as La Cira-Infantas. This approach can be applied to other fields of a similar geological setting.

3.8 Acknowledgments

I thank ECOPETROL (National Oil Company of Colombia) and Stanford Rock Physics Project for providing data and financial support for this study. I am grateful with Dr. Jack Dvorkin for sharing his understanding of poroelasticity and time to generate the

bimodal mixture model. Thanks to Professor Gary Mavko for providing the Estes' experimental data and useful comments. This study was also supported by the Department of Energy (Grants # DE-FG03-98ER14904 and DE-FG03-86ER13601).

3.9 References

Amaefule, J. O., M. Altunbay, D. Tiab, D. Kersey, and D. K. Keelan, 1993, Enhanced reservoir description, using core and log data to identify hydraulic (flow) units and predict permeability in uncore intervals/wells: 68rd annual technical conference and exhibition of the Society of Petroleum Engineers, Houston, TX, Oct. 3-6, SPE 26436, 16 p.

Avseth P., J. Dvorkin, and G. Mavko, 2000, Rock physics diagnostic of North Sea sands: Link between microstructure and seismic properties: Geophysical Research Letters, **27,** p. 2761-2764.

Bally, A. W., ed., 1987, Atlas of seismic stratigraphy, Volume I: AAPG Studies in geology 27, 125 p.

Beard, D. C. and P. K. Weyl, 1973, Influence of texture on porosity and permeability of unconsolidated sands: American Association of Petroleum Geologists Bulletin, **57,** no. 2, p. 349-369.

Blatt, H., G. Middleton, and R. Murray, 1980, Origin of sedimentary rocks: Englewood Cliffs, New Jersey, Prentice-Hall, Inc., 782 p.

Bloch, S., 1994a, Importance of reservoir quality prediction in exploration, in M. D. Wilson, Ed., Reservoir quality assessment and prediction in clastic rocks: SEPM (Society for Sedimentary Geology) short course 30, p. 5-8.

Bloch, S., 1994b, Effect of detrital mineral composition on reservoir quality, in M. D. Wilson, Ed., Reservoir quality assessment and prediction in clastic rocks: SEPM (Society for Sedimentary Geology) short course 30, p. 161-182.

Bloch, S. and J. H. McGowen, 1994, Influence of depositional environment on reservoir quality prediction, in M. D. Wilson, Ed., Reservoir quality assessment and prediction in clastic rocks: SEPM (Society for Sedimentary Geology) short course 30, p. 42-58.

Boggs, S., 1995, Principles of sedimentology and stratigraphy: Englewood Cliffs, New Jersey, Prentice-Hall, Inc., 774 p.

Brown, A. R., 1999, Interpretation of three-dimensional seismic data: American Association of Petroleum Geologist, Memoir 42, SEG Investigations in geophysics, No. 9, Fifth edition, 514 p.

Chambers R., J. M. Yarus, and K. Hird, 2000, Petroleum geostatistics for nongeostaticians, part 2: The Leading Edge, **19,** June, No. 6, p. 592-599

Clarke, R. H., 1979, Reservoir properties of conglomerates and conglomeratic sandstones: American Association of Petroleum Geologists Bulletin, **63,** no. 5, p. 799-809.

Cumberland, D. J. and R. J. Crawford, 1987, The packing of particles, Handbook of powder technology: Elsevier.

Dickey, P., 1992, La Cira-Infantas Field, Middle Magdalena Basin, in E. A. Beaumont and N. H. Foster, Eds., Structural Traps VII, AAPG Treatise of Petroleum Geology, Atlas for Oil and Gas Field, p. 323-347.

Dickinson, W. R., 1985, Interpreting provenance relations from detrital modes of sandstones, in Zuffa, G. G. ed., Provenance of arenites, Reidel, p.333-361.

Dvorkin, J., G. Mavko, and A. Nur, 1991, The effect of cementation on the elastic properties of granular material: Mechanics of Materials, **12,** p. 207-217.

Dvorkin, J., A. Nur, and H. Yin, 1994, Effective properties of cemented granular material: Mechanics of Materials, **18,** p. 351-366.

Dvorkin, J., A. Nur, 1996, Elasticity of high-porosity sandstones: theory for two North Sea datasets: Geophysics, **61,** no. 5, p. 1363-1370.

Doyen P., 1988, Porosity from seismic data—a geostatistical approach: Geophysics, **53,** no. 10, p. 1263-1276.

Ebanks, W. J. Jr., 1987, Flow unit concept-integrated approach to reservoir descriptions for engineering projects, abst.: AAPG Bulletin, **71,** n. 5, p. 551-552.

Ebanks, W. J. Jr., M. H. Scheihing, and C. D. Atkinson, 1993, Flow units for reservoir characterization, in D. Morton-Thompson and A. M. Woods, Eds., Development Geology Reference Manual, AAPG Methods in Exploration Series, no. 10, p. 282-285.

Einsele, G., W. Ricken, and A. Seilacher, 1991, Eds., Cycles and events in stratigraphy: Berlin Heidelber, Springer-Verlag, 955 p.

Emery, D. and K. Myers, 1996, Sequence stratigraphy: Blackwell Science, 297 p.

Estes, C. A., G. Mavko, H. Yin, and T. Cadoret, 1994, Measurements of velocity, porosity, and permeability on unconsolidated granular materials: Stanford rockphysics and borehole geophysics project, annual report, **55,** p G1-1 – G1-9.

Folk, R. L., 1951, Stages of textural maturity in sedimentary rocks: Journal of Sedimentary Petrology, **21,** no. 3, p. 127-130.

Gómez, E., T. Jordan, S. Kelley, and M. Heizler, 1999, Late Cretaceous and Cenozoic basin architecture of the southernmost Middle Magdalena Valley, Colombia, multiple constraints on syndeformational sedimentation: AAPG/SEPM 1999 Annual Meeting, Abstracts with Programs, April 11-14, San Antonio, Texas.

Gunter G. W., J. M. Finneran, and D. J. Hartmann, 1997, Early determination of reservoir flow units using an integrated petrophysical method: SPE Annual Technical Conference and Exhibition, San Antonio, Texas, 5-6 October, SPE 38679.

Han, D., 1986, Effects of porosity and clay content on acoustic properties of sandstones and unconsolidates sediments: Ph. D. Thesis, Stanford University.

Hamlin, H. S., S. P. Dutton, R. J. Seggie, N. Tyler, and J. S. Yeh, 1995. Flow-unit characterization and recovery optimization of a braid-delta sandstone reservoir, Tirrawarra oil field, South Australia: Bureau of Economic Geology, Report of Investigations no. 231, 44 p.

Hardage, B., R. Levey, V. Pendleton, J. Simmons, and R. Edson, 1994, A 3-D seismic case history evaluating fluvially deposited thin-bed reservoirs in a gas-producing property: Geophysics, **59**, no. 11, p. 1650-1665.

Hashin, Z. and S. Shtrikman, 1963, A variational approach to the elastic behavior of multiphase materials: Journal of the Mechanical Physics of Solids, **11**, p. 127-140.

Hearns, C. L., W. J. Ebanks, Jr., R. S. Tye, and V. Ranganathan, 1984, Geological factors influencing reservoir performance of the Hartzog Draw field: Journal of Petroleum Technology, **36,** p. 1335-1344.

Helgensen, J., I. Magnus, S. Prosser, G. Saigal, G. Asmodt, D. Dolberg, and S. Busman, 2000, Comparison of constrained sparse spike and stochastic inversion for porosity prediction at Kristin Field: The Leading Edge, 19, no. 4, p. 400-407

Hirsche, K., J. Porter-Hirsche, L. Mewhort, and R. Davis, 1997, The use and abuse of geostatistics: The Leading Edge, **16,** no. 3, p. 253-260.

ICP-ECP, 1996, Estratigrafia del Terciario del Valle Medio del Magdalena, caracterizacion estratigrafica y prospectividad: Ecopetrol, Technical report, 45 p.

Journel, A., 1994, Geostatistics and reservoir geology, in Yarus and Chambers, Eds., Stochastic Modeling and Geostatistics, AAPG Computer Applications in Geology, no. 3, p. 19-20.

Krause, F. F., H. N. Collins, D. A. Nelson, S. D. Mochemer, and P. R. French, 1987, Multiscale anatomy of a reservoir, geological characterization of Pembina- Cardium pool, west-central Alberta, Canada: AAPG Bulletin, **71,** p. 1233-2260.

Kupecz, J. A., J. G. Gluyas, and S. Bloch, 1997, Eds., Reservoir quality prediction in sandstones and carbonates: American Association of Petroleum Geologist, Memoir 69, 311 p.

Langston, J. R. and G. E. Chin, 1968, Rainbow Member facies and related reservoir properties, Rainbow Lake, Alberta: AAPG Bulletin, **52,** n. 10, p. 1925-1955.

Laverde, F., 1996, Estratigrafia de alta resolucion de la seccion corazonada en el campo La Cira: Ecopetrol, Technical report, 37 p.

Marion, D., 1990, Acoustical, mechanical, and transport properties of sediments and granular materials: Ph. D. Thesis, Stanford University.

Mavko G. and A. Nur, 1996, Rock-Physics, the link between rock properties and seismic interpretation: Abstracts NPF seminar—Geophysics for lithology prediction, Kristiansand, Norway, March 11-13, 1996.

Mavko G., T. Mukerji, and J. Dvorkin, 1998, The rock physics handbook, tools for seismic analysis in porous media: Cambrige, Cambrige University Press, 329 p.

Maxey, G. B., 1964. Hydrostratigraphic units: Journal of Hydrology, **2,** p. 124-129.

Mesa, A., 1995, Diagenesis y calidad del reservorio del campo La Cira: Ecopetrol, Technical report, 44 p.

Miall, A. D., 1991, Hierarchies of architectural units in terrigenous clastic rocks, and their relationship to sedimentation rate, in A. D. Miall and N. Tyler, Eds., The three-dimensional facies architecture of terrigenous clastic sediments and its implications

for hydrocarbon discovery and recovery: SEPM, Concepts in sedimentology and paleontology, **3,** p. 6-12.

Miall, A. D., 1992, Alluvial deposits, in R. G. Walker and N. P. James, Eds., Facies models-response to sea level change: Geological Association of Canada, p. 119-141.

Miall, A. D., 1996, The geology of fluvial deposits: Sedimentary facies, basin analysis and petroleum geology: Berlin Heidelber New York, Springer-Verlag, 582 p.

Miall, A. D., 1997, The geology of stratigraphic sequences: Berlin Heidelber New York, Springer-Verlag, 337 p.

Montgomery, S., 1991, Reservoir (re)characterization in older fields: Benefits for secondary recovery--a case history in the Tensleep Sandstone, South Casper Creek Field, Wyoming: Petroleum frontiers, Littleton, Co., Petroleum Information Corp., **8,** no. 3, 61 p.

Morales, L. G., D. J. Podesta, W. C. Hatfield, H. Tanner, S. H. Jones, M. H. Barker, D. J. O'Donoghue, C. E. Mohler, E. P. Dubois, C. Jacobs, and C. R. Goss, 1958, General geology and oil occurrences of the Middle Magdalena Valley, Colombia: Habitat of Oil Symposium, American Association of Petroleum Geologists, p. 641-695.

Nur, A., G. Mavko, J. Dvorkin, D. Galmudi, 1998, Critical porosity: A key to relating physical properties to porosity in rocks: The Leading Edge, **17,** 357-362.

Orton, G. J., and H. G. Reading, 1993, Variability of deltaic processes in terms of sediment supply, with particular emphasis on grain size: Sedimentology, 40, p. 475-512.

Pettijohn, F. J., P. E. Potter, and R. Siever, 1973, Sand and sandstone: New York, Springer-Verlag, 618 p.

Raymer, L. L., E. R. Hunt, and J. S. Gardner, 1980, An improved sonic transit time-to-porosity transform: SPWLA, 21 st Annual Logging Symposium, July.

Rodriguez, A., 1988, Facies modeling and flow unit concepts as a sedimentary tool in reservoir description, a case study: 63rd Annual technical conference and exhibition of the Society of Petroleum Engineers, Houston, TX, Oct. 2-5, SPE 18154, 8 p.

Russell, B. H., 1988, Introduction to seismic inversion methods: SEG Courses Notes Series, No. 2.

Schon, J. H., 1996, Physical properties of rocks: Fundamentals and principles of petrophysics: 1st edition, Oxford, OX, UK, Tarrytown, N.Y., U.S.A., Pergamon, 583 p.

Selley, R. C., 1996, Ancient sedimentary environments and their sub-surface diagnosis: London, Chapman & Hall, 300 p.

Sheriff, N. E., 1992, Ed., Reservoir geophysics: SEG Investigations in Geophysics, no. 7, 408 p.

Sheriff, R. E. and L. P. Geldart, 1995, Exploration seismology, New York, Cambridge University Press, 592 p.

Slatt, R. M., and G. L. Hopkins, 1990, Scaling of geological reservoir description to engineering needs: Journal of Petroleum Technology, Feb., p. 202-210.

Slatt, R. M., and W. E. Galloway, 1993, Geological heterogeneities, in D. Morton-Thompson and A. M. Woods, Eds., Development Geology Reference Manual, AAPG Methods in Exploration Series, no. 10, p. 278-280.

Sneider, R. M., F. H. Richardson, D. D. Paynter, R. R. Eddy, and I. A. Wyant, 1977, Predicting reservoir rock geometry and continuity in Pennsylvanian reservoirs, Elk City field, Oklahoma: Journal of Petroleum Technology, July, p. 851-866.

Taborda, B., 1965, The Geology of the De Mares Concession: Geological field trips, Colombia, 1958-1978: Colombian Society of Petroleum Geologists and Geophysicists, p. 119-159.

Tyler, N. and R. J. Finley, 1991, Architectural controls on the recovery of hydrocarbons from sandstone reservoirs, in A. D. Miall and N. Tyler, Eds., The three-dimensional facies architecture of terrigenous clastic sediments and its implications for hydrocarbon discovery and recovery: SEPM, Concepts in sedimentology and paleontology, **3,** p. 1-5.

Vail, R., R. Mitchum, R. Todd, J. Widmier, S. Thompson, J. Sangree, J. Bubb, and W. Hatledid, 1977, Seismic stratigraphy and global changes in sea level, in C. E. Payton, Eds., Seismic stratigraphy, application to hydrocarbon exploration, AAPG, Mem. 26, p. 49-212.

Van Wagoner, J. C., R. M. Mitchum, K. M. Campion, and V. D. Rahmanian, 1990, Siliciclastic sequence stratigraphy in well logs, cores and outcrops: AAPG methods in exploration series, no. 7, 55 p.

Villamil, T., 1999, Campanian-Miocene tectonostratography, depocenter evolution and basin development of Colombia and Western Venezuela: Palaeogeography, Palaeoclimatology, Palaeoecology, No. 153, p. 239-275.

Weber, J. K. and L. C. Van Geuns, 1990, Framework for constructing clastic reservoir simulation models: Journal of Petroleum Technology, October, p. 1248-1297.

Weimer, P. and H. W. Posamentier, eds., 1993, Silisiclastic sequence stratigraphy: Recent developments and applications: AAPG memoir 58, 492 p.

Weimer, P. and T. L. Davis, 1996, Eds., Applications of 3-D seismic data to exploration and production: American Association of Petroleum Geologist, Studies in Geology 42, SEG Geophysical Developments Series, no. 5, 270 p.

Wilgus, C. K., B. S. Hastings, H. Posamentier, J. Van Wagoner, C. A. Ross, C. G. Kendall, Eds., 1988, Sea level change, an integrated approach: SEPM Special Publication 42, 407 p.

Wyllie, N. R. J., A. R. Gregory, and L. W. Gardner, 1956, Elastic wave velocities in heterogeneous and porous media: Geophysics, **21,** p. 41-70.

Yin, H., D. H. Han, and A. Nur, 1988, Study of velocity and compaction on sand-clay mixture: Stanford Rockphysics and Borehole Geophysics Project, annual report, **33.**

Yin, H., 1992, Acoustic velocity and attenuation of rock: Isotropy, intrinsic anisotropy, and stress induced anisotropy: Ph. D. Thesis, Stanford University.

Appendix 1 Effective Medium Models for Granular Composites

Contact Cement Model. The Dvorkin and Nur (1996) model assumes that the composite is built from the original pack of identical spherical grains at critical porosity (36-40%). Porosity then decreases due to the uniform deposition of cement on the surface of every grain (Figure A1).

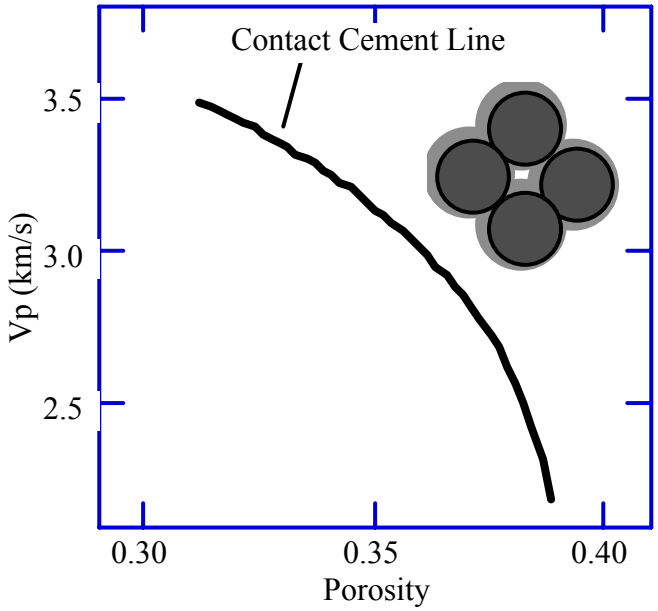

Figure A1: Contact cement model. Porosity decreases from the critical porosity value due to cement deposition around grains. This diagenetic process results in a strong velocity increase.

The effective bulk (K_{dry}) and shear (G_{dry}) moduli of dry rock are:

$$K_{dry} = \frac{n}{6}(1-\phi_c)M_c S_n,\ G_{dry} = \frac{3}{5}K_{dry} + \frac{3}{20}n(1-\phi_c)G_c S_\tau, \qquad \text{(A.1)}$$

where n is the coordination number which is the average number of contacts per grain (n = 6 – 9); ϕ_c is the critical porosity; G_c is the shear modulus of the cement; K_c is the bulk modulus; and $M_c = K_c + 4G_c / 3$ is the M-modulus of the cement. S_n and S_τ are:

$$
\begin{aligned}
&S_n = A_n(\Lambda_n)\alpha^2 + B_n(\Lambda_n)\alpha + C_n(\Lambda_n),\ A_n(\Lambda_n) = -0.024153 \cdot \Lambda_n^{-1.3646},\\
&B_n(\Lambda_n) = 0.20405 \cdot \Lambda_n^{-0.89008},\ C_n(\Lambda_n) = 0.00024649 \cdot \Lambda_n^{-1.9864};\\
&S_\tau = A_\tau(\Lambda_\tau, \nu_s)\alpha^2 + B_\tau(\Lambda_\tau, \nu_s)\alpha + C_\tau(\Lambda_\tau, \nu_s),\\
&A_\tau(\Lambda_\tau, \nu_s) = -10^{-2} \cdot (2.26\,\nu_s^2 + 2.07\,\nu_s + 2.3) \cdot \Lambda_\tau^{0.079\nu_s^2 + 0.1754\nu_s - 1.342},\\
&B_\tau(\Lambda_\tau, \nu_s) = (0.0573\,\nu_s^2 + 0.0937\,\nu_s + 0.202) \cdot \Lambda_\tau^{0.0274\nu_s^2 + 0.0529\nu_s - 0.8765},\\
&C_\tau(\Lambda_\tau, \nu_s) = 10^{-4} \cdot (9.654\,\nu_s^2 + 4.945\,\nu_s + 3.1) \cdot \Lambda_\tau^{0.01867\nu_s^2 + 0.4011\nu_s - 1.8186};\\
&\Lambda_n = 2G_c(1-\nu_s)(1-\nu_c)/\,[\pi G_s(1-2\nu_c)],\ \Lambda_\tau = G_c\,/\,(\pi G_s);\\
&\alpha = [(2/3)(\phi_c - \phi)/\,(1-\phi_c)]^{0.5};\\
&\nu_c = 0.5(K_c/\,G_c - 2/3)/\,(K_c/\,G_c + 1/3);\\
&\nu_s = 0.5(K_s/\,G_s - 2/3)/\,(K_s/\,G_s + 1/3);
\end{aligned}
\qquad \text{(A.2)}
$$

where K_s and G_s are the bulk and shear moduli of the grain material, respectively.

This model can accurately predict velocity in many cemented sands (Figure A2).

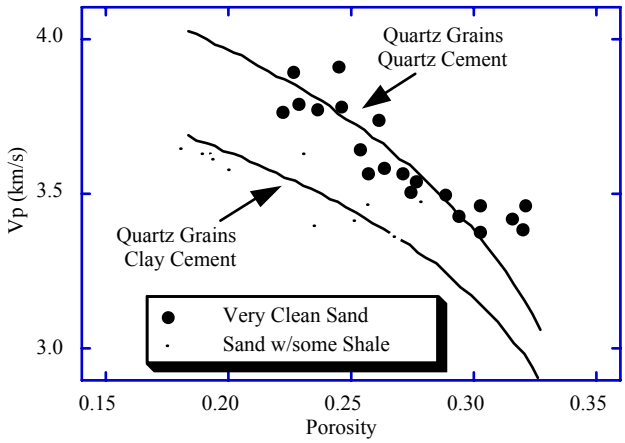

Figure A2: Example of adjusting cementation model to a lab data set. By changing the properties of cement, we can match the very clean sandstone data and the data from sandstones with more shale.

Constant Cement Model. In this model (Asveth et al., 2000), the composite is based on the pack of identical spherical grains at critical porosity. Porosity then decreases to some "cemented porosity" due to the uniform deposition of cement on the surface of every grain. Finally, porosity decreases due to the deposition of cement away from grain contacts.

At the cemented porosity, the dry-rock moduli are calculated from the contact-cement theory. For smaller porosities, the cemented porosity point is connected with the solid-phase modulus at zero porosity. This solid-phase modulus is that of the mixture of $1-\phi_c$ (one minus critical porosity) fraction of grains and ϕ_c (critical porosity) fraction of cement. These two points are connected in the lower Hashin-Shtrikman fashion (Figure A3).

The effective bulk (K_{dry}) and shear (G_{dry}) moduli of dry rock are:

$$
\begin{aligned}
K_{dry} &= \left(\frac{\phi / \phi_b}{K_b + 4G_b/3} + \frac{1-\phi/\phi_b}{K_{fs} + 4G_b/3}\right)^{-1} - 4G_b/3, \\
G_{dry} &= \left(\frac{\phi / \phi_b}{G_b + z} + \frac{1-\phi/\phi_b}{G_{fs} + z}\right)^{-1} - z, \; z = \frac{G_b}{6}\frac{9K_b + 8G_b}{K_b + 2G_b}; \\
K_{fs} &= \frac{1}{2}\left[(1-\phi_c)K_s + \phi_c K_c + \left(\frac{1-\phi_c}{K_s} + \frac{\phi_c}{K_c}\right)^{-1}\right], \\
G_{fs} &= \frac{1}{2}\left[(1-\phi_c)G_s + \phi_c G_c + \left(\frac{1-\phi_c}{G_s} + \frac{\phi_c}{G_c}\right)^{-1}\right],
\end{aligned}
\tag{A.3}
$$

where K_b and G_b are the dry-rock bulk and shear moduli, respectively, calculated from the contact cement model at $\phi = \phi_b$ (see Contact Cement Model in previous section).

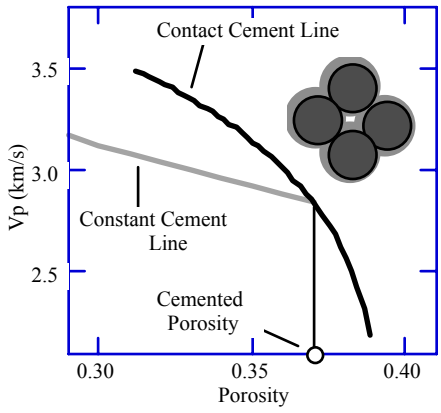

Figure A3: Constant cement model.

This model accurately predicts velocity in many reservoirs (Figure A4).

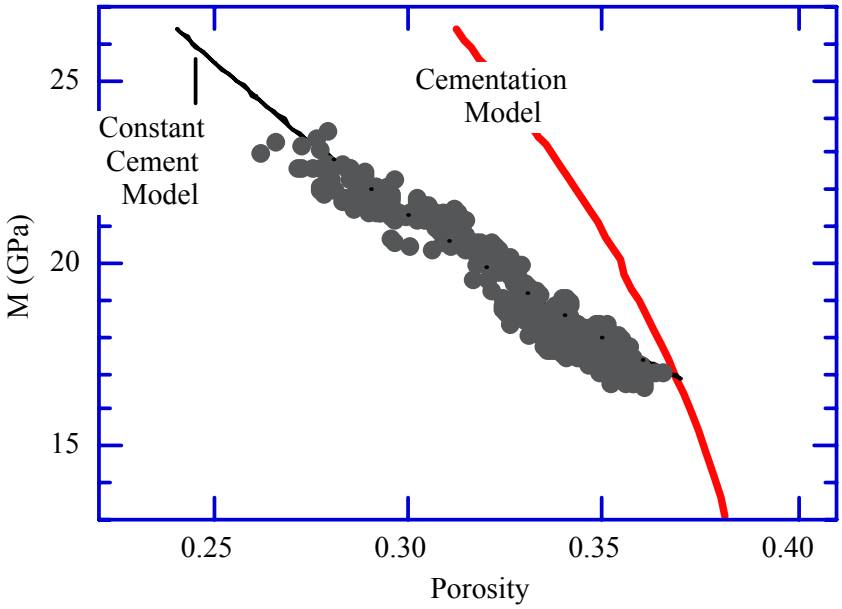

Figure A4: Constant cement model applied to North Sea well log data.

Unconsolidated Sand Model. In this model, Dvorkin and Nur (1996) assume that the composite is based on the pack of identical spherical grains at critical porosity, then porosity decreases due to the deposition of cement away from grain contacts. At critical porosity, the elastic moduli of the dry frame are calculated versus effective pressure from the Hertz-Mindlin equations. For smaller porosities, the critical porosity point is connected with the solid-phase modulus at 0% porosity in the lower Hashin-Shtrikman fashion (Figure A5).

The effective bulk (K_{dry}) and shear (G_{dry}) moduli of dry rock are:

$$K_{dry} = \left[\frac{\phi / \phi_c}{K_{HM} + \frac{4}{3} G_{HM}} + \frac{1 - \phi / \phi_c}{K_{fs} + \frac{4}{3} G_{HM}}\right]^{-1} - \frac{4}{3} G_{HM},$$
$$G_{dry} = \left[\frac{\phi / \phi_c}{G_{HM} + z} + \frac{1 - \phi / \phi_c}{G_{fs} + z}\right]^{-1} - z, \quad z = \frac{G_{HM}}{6}\left(\frac{9K_{HM} + 8G_{HM}}{K_{HM} + 2G_{HM}}\right); \tag{A.4}$$

where

$$K_{HM} = [\frac{n^2(1-\phi_c)^2 G_s^2}{18\pi^2(1-\nu_s)^2} P]^{\frac{1}{3}},$$
$$G_{HM} = \frac{5-4\nu_s}{5(2-\nu_s)} [\frac{3n^2(1-\phi_c)^2 G_s^2}{2\pi^2(1-\nu_s)^2} P]^{\frac{1}{3}}; \quad \text{(A.5)}$$
$$\nu_s = \frac{1}{2}(\frac{K_s}{G_s} - \frac{2}{3}) / (\frac{K_s}{G_s} + \frac{1}{3}),$$

and K_{fs} and G_{fs} are the bulk and shear moduli of the solid phase, respectively, given in Equation A.3. This model successfully mimics many in-situ data (Figure A6).

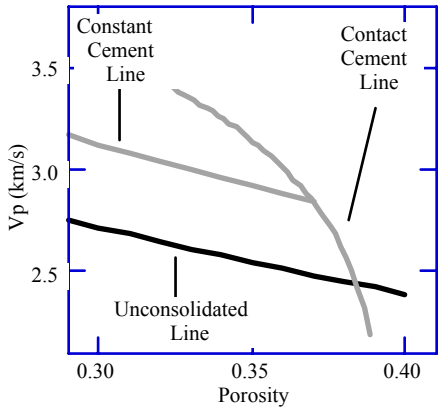

Figure A5: Unconsolidated sand model.

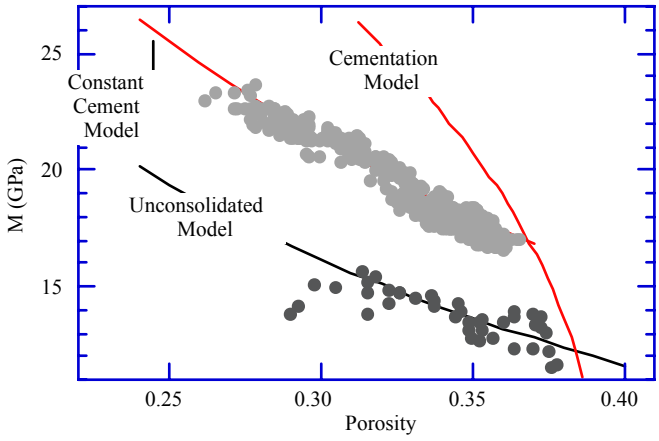

Figure A6: Unconsolidated sand model applied to North Sea well log data.

Chapter 4

Bypassed Oil Identification and Reservoir Monitoring Using Open- and Cased-hole Sonic Logging, La Cira-Infantas Oil Field

4.1 Abstract

This chapter presents a rock physics model for identifying the quality of rock and pore fluid in a cased hole from dipole sonic data, as well as for monitoring temporal changes in the reservoir from repeated compressional wave data in the well. I use a theoretical rock physics model that links porosity, lithology, pressure, and pore fluid to the elastic rock properties in fluvial reservoirs in La Cira-Infantas oil field (Colombia) to interpret compressional- and shear-wave log data in a cased hole. By analyzing the Vp/Vs ratio from multi-pole velocity logs, it is possible to differentiate between nonhydrocarbon- and hydrocarbon-bearing sands.

These theoretical results are consistent with Vp/Vs empirical relations. Theoretical modeling has an advantage over empirical relations because it is based on sound physical principles and as such can be generalized and fine-tuned to a site-specific geological situation. It is straightforward to forward model porosity, lithology, pressure, and pore-fluid effect on Vp/Vs using a theoretical model as opposed to empirical models.

The model predictions are also consistent with time-lapse sonic log data where the P-wave velocity shows a drop in the intervals open for production. This effect is most likely associated with free gas coming out of solution. The Vp/Vs ratio, as calculated from multi-pole sonic logs, is a promising indicator for delineating bypassed oil behind the casing and pay intervals. It can also be used for reservoir depletion monitoring.

4.2 Introduction

4.2.1 Research motivation

La Cira-Infantas oil field (LCI) is located in the Middle Magdalena Valley Basin, Colombia. The estimated oil originally in place was 3700 million barrels (MMBO). After the drilling of more than 1703 wells, the cumulative production is only 724 MMBO. About 55% of total number of wells drilled in the giant LCI have no electric logs since they were drilled before the development of borehole logging (Taborda, 1965). Dickey (1992), who was the chief geologist in LCI during the 1930's, wrote the following about the effect of the lack of logging tools: "*Before electric logging it was impossible to see where the individual pay sands were by examination of the cuttings. Consequently, many sands were shut off behind pipe".* In mature oil fields like LCI, the possible reserve increment from the re-evaluation of existing wells to detect bypassed oil intervals can be economically and technically feasible. Well recompletions guided by new cased-hole logging are economically attractive due to the high probability of adding new oil with a moderate capital investment.

Modern nuclear logs are the main tools in detecting bypassed oil behind the casing and reservoir monitoring, however their effectiveness is limited drastically by borehole and reservoir conditions. Cased-hole acoustic techniques have been developed during the last few years and serve as reliable alternatives to nuclear tools. New rock physics models are needed to accurately interpret these modern acoustic data. This chapter presents a rock physics model and its application for identifying the quality of rock and pore fluid in a cased hole from dipole sonic data, as well as for monitoring temporal changes in the LCI reservoirs from repeated compressional wave data in the well.

4.2.2 Cased-hole logging for detecting bypassed oil

Diverse cased-hole logging technologies have been used for evaluating reservoir properties behind the casing (Smolen, 1987, 1996). Several applications based on cased-hole logging have been reported, including the evaluation of porosity, lithology, and hydrocarbon saturation. Cased-hole logs play a particularly important role in detecting and evaluating bypassed hydrocarbon intervals. Logging techniques varying from

borehole gravimeter (Rasmussen, 1975; Gournay, 1982) and conventional gamma-ray logs (King and Bradley, 1977) to advanced nuclear tools have been applied successfully to identified bypassed reserves.

Modern nuclear tools, such as pulsed neutron capture (PNC), pulsed neutron spectral (PNS), and the high-resolution gamma ray spectroscopy, are the primary logs in detecting bypassed oil behind the casing (Felder, 1988; Westaway et al., 1981). The applicable results of these tools are only trustworthy in particular borehole and reservoir conditions. Their cased-hole log responses are strongly affected by several borehole environmental factors, their limited depth of investigation, and reservoir characteristics such as shaliness, radioactive zones, low porosity, brine salinity, and complex lithology (Felder, 1988). During the last decade a cased-hole acoustic technique has been developed and serves as a reliable alternative to the nuclear tools for detecting oil behind the pipe: full-waveform sonic logging.

4.2.3 Full-waveform sonic logging

Since the 1950's, the original applications of acoustic logging were based on the idea of measuring formation compressional velocity using monopole-based technology. In the early 1990's, a modern generation of commercial multi-pole sonic tools became available (Harrison et al., 1990; Chen and Eriksen, 1991; Nieto and Cowper, 1991), and full-waveform logs can now be obtained by recording the complete pressure signal at each receiver downhole for every source pulse (Paillet and Cheng, 1991).

The processing of these recorded acoustic waveforms provides formation velocities, such as compressional, shear, and Stoneley propagation velocities. These velocities can be applied to estimate geomechanical properties in situ (Paillet et al., 1992) and formation properties, such as lithology, porosity, fluid content, and permeability (Hornby, et al., 1992). In addition, they can be use for fracture detection and AVO calibration (Schlumberger, 1995).

Improved acquisition and processing methods have made the recording of formation acoustic data feasible in open and cased holes (Tubman et al., 1984; Bettis et al., 1987). These tools usually use long source-receiver separation, multiple receivers, and lower frequency sources. Compressional wave velocities are usually determined from monopole

waveforms and shear wave velocities are determined from dipole or quadrupole waveforms (Schlumberger, 1990; Chen and Eriksen, 1991).

During the last decade several workers have published case histories illustrating the successful use of different full-waveform acoustic commercial tools for detecting hydrocarbons behind the casing (Kessler and Sanders, 1989; Georgi et al., 1991; Sanders, 1993; Brie et al., 1995; Yan et al., 1995; Moos et al., 1995a; Moos et al., 1995b; Moos and Dvorkin, 1996; Moos, 1997; Moos and Walker, 1997; Schiuma et al., 1997). However, the successful application of this acoustic tool is not always guaranteed, for cased-hole shear wave logging is very troublesome in some areas because borehole conditions and the similarity of the dipole mode and the Stoneley wave (Walker, 1997).

4.2.4 Data and methodology

The siliciclastic reservoirs in LCI are rocks from the Colorado Formation (Zone A) and Mugrosa Formation (Zone B and C). The production of hydrocarbons comes from loosely consolidated Tertiary sands. The reservoir rocks are fine to medium grained, subarkosic, and sometimes shaly sandstones (Figure 4.1).

The average porosity is 21% in Zone A, 20% in Zone B, and 23% in Zone C. Permeability may be as high as 1500 mD (Mesa, 1995; Dickey, 1992). High-resolution sequence stratigraphic analyses (Laverde, 1996) indicate that the depositional facies of La Cira-Infantas Tertiary rocks are associated with fluvial channel systems. Zones A and B represent mixed load channels or meandering systems, in contrast with Zone C, which was deposited as bed load channels or braided stream systems (Figure 4.1).

In this study is analyzed the relationship between the acoustic properties and oil saturation in Zone C and the La Cira Sands interval, the latter being a secondary member of Zone B. A set of data from well LC-1882 was selected to carry out this task (Figure 4.2). LC-1882 was completed in Zone C and a set of open-hole well logs, including a monopole sonic log, was collected in 1988. Seven years later, Zone C was closed, new cased-hole monopole and dipole sonic logs were recorded, and a new upper interval (La Cira Sands) was open for production.

This chapter presents a comparison between the open (1988) and cased-hole (1995) monopole sonic measurements, and the results of the application of the monopole and

dipole sonic logs to detecting hydrocarbons behind casing in LCI fluvial reservoirs. The commercial sonic tool used by the oil field operator in 1995 was a Dipole Shear Sonic Imager (DSI) from Schlumberger. The DSI tool integrates dipole- and monopole-based technology into one assemblage, providing compressional, shear, and Stoneley velocities (Schlumberger, 1990; Harrison et al., 1990). Figure 4.3 shows the DSI tool, which is a multi-receiver instrument with a linear array of eight receiver stations, two dipole transmitters, and a monopole transmitter (Schlumberger, 1990).

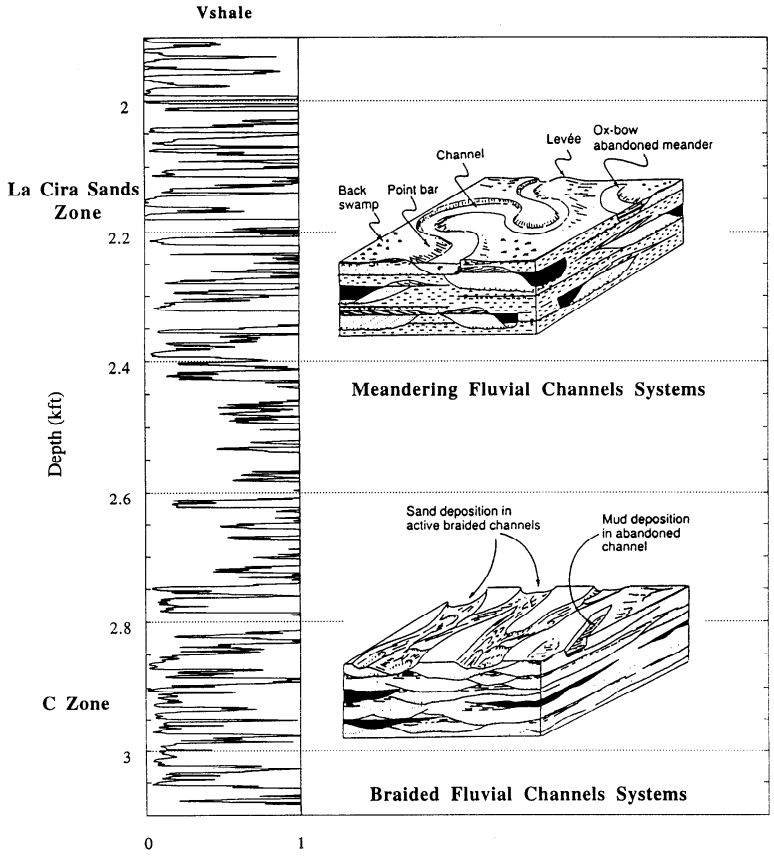

Figure 4.1: Well LC-1882. Productive Zone B (La Cira Sands Zone) represents a meandering system, in contrast with Zone C, which was deposited as a braided stream system (Block diagrams adapted from Selley, 1996).

4.3 Pore Fluid Effect

The detection of bypassed oil and the reservoir monitoring using cased- and open-hole sonic logs is based on the strong influence of oil or water on the bulk modulus and

compressional wave velocity (Vp) and the negligible influence on the shear modulus and transverse wave velocity (Vs). Vp/Vs ratio values for oil and water-saturated porous rocks are usually much higher than for gas-saturated rocks. In addition, oil-bearing rocks generally exhibit a lower bulk modulus and density than water-bearing rocks. Therefore, when Vp and Vs are know from field measurements, as in the LCI case where sonic log measurements are available, the Vp/Vs ratio value can be use as a detector of the oil saturation in the reservoir rocks (Nur and Wang, 1988).

This effect is the basis of applying empirical Vp/Vs relations of Castagna et al. (1985 and 1993), Han (1986), and Williams (1990) to separating water-saturated from hydrocarbon-saturated rocks in the acoustic velocity domain. These empirical relations are statistical fits to well log and lab data for water-saturated shales and sands. The approach presented here is based on effective-medium modeling, which allows one to directly predict the effect of different pore fluids as well as porosity and mineralogy on the elastic rock properties.

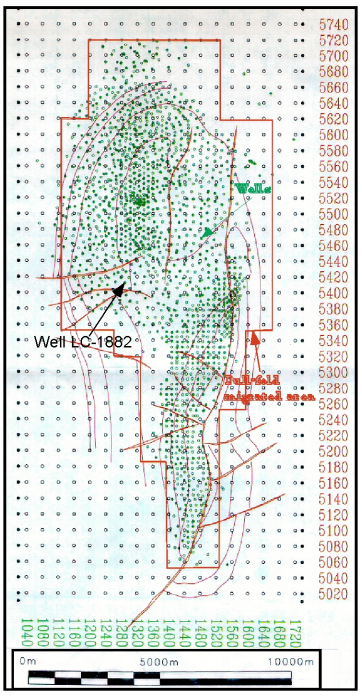

Figure 4.2: Base map of the La Cira-Infantas oil field showing the location of oil wells, surface geology, and the full-fold migrated area of the seismic survey. Note the location of well LC-1882.

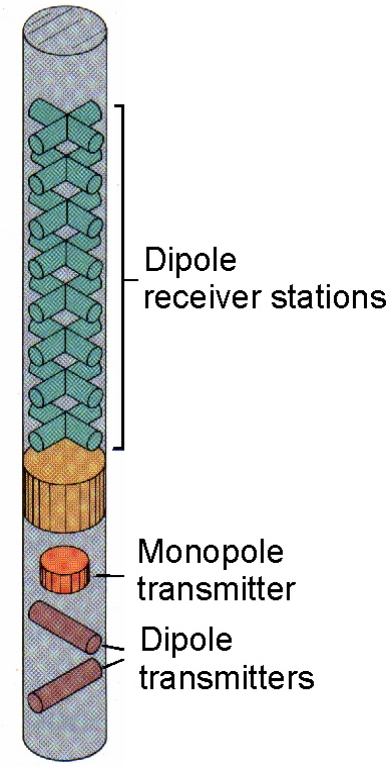

Figure 4.3: Schematic of the Dipole Shear Sonic Imager (DSI) tool (Schlumberger, 1990).

The uncemented sand model of Dvorkin and Nur (Appendix A, Chapter 3; Mavko et al., 1998) was selected for studying the pore-fluid effect in LCI reservoir rocks, based on the fact that the sands under examination are loosely consolidated. The model correlates the elastic reservoir properties to porosity, mineralogy, pore fluid, and differential pressure.

This model is an effective medium approach that connects two end-points in the elastic-moduli-porosity plane. One end-point is at zero porosity where the elastic moduli of the rock are those of the solid phase. The other is at the critical porosity (about 40%) where the sand is modeled as a pack of elastic spheres. The model assumes that porosity reduces from the initial grain-pack value due to the deposition of solid particles away from grain contacts. These non-contact solid particles softly affects the compressibility of the rock. The pressure dependence is introduced through the elastic moduli of the dry frame at the critical porosity, according to the Hertz-Mindlin elastic sphere contact model.

The LCI rock physics model can be used to identify hydrocarbons in situ when both P- and S-wave data are available. Figure 4.4 indicates a cross-plot of Vp versus Vs for dipole sonic data for the rock interval between 787.75 m and 799 m of depth in well LC-1882. The solid-phase moduli and density values used in the model correspond to a mixture of 80% quartz and 20% feldspar, typical for the arkosic sands of LCI (Mesa, 1995). The fluid phase varies between water with an average salinity of 19000 ppm and oil with an average A.P.I. gravity of 24.1 (Morales et al., 1958). The effective fluid bulk modulus and density were calculated using the relations of Batzle and Wang (1992). The effective pressure used in the model is 11 MPa.

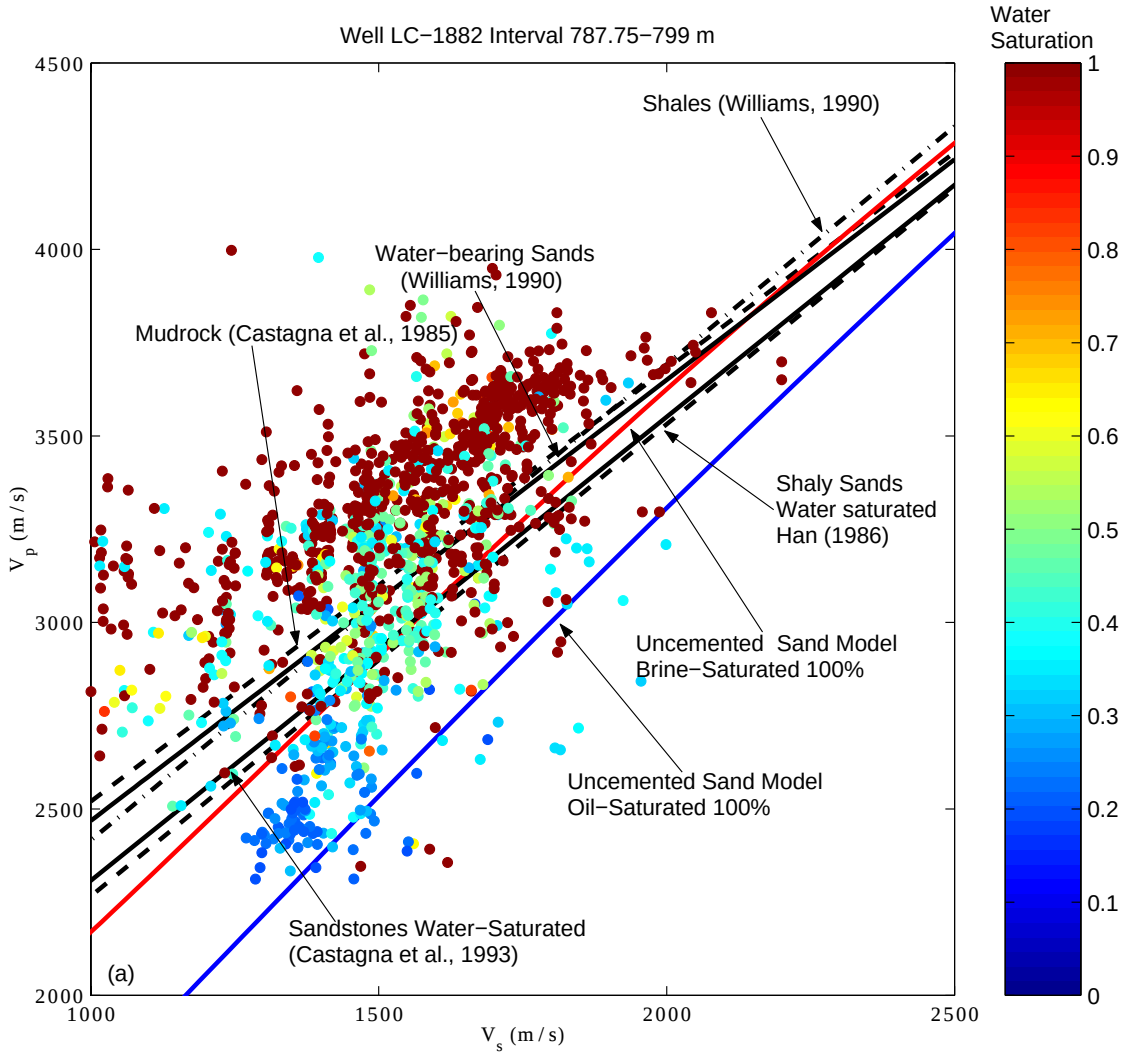

Figure 4.4: Vp versus Vs for log data. The theoretical and empirical model lines are superimposed on the plots.

The dipole tool sampled the rock beyond the invaded zone. The model line drawn at 100% brine saturation clearly separates the water-saturated rocks from those with hydrocarbons. The LCI model line is close to the empirical relations by Castagna et al. (1985) and Williams (1990) that are based on well log data. These curves are slightly different from those drawn from Han's (1986) and Castagna et al. (1993) relations that are based on ultrasonic laboratory velocity data. The advantage of the theoretical treatment of the fluid detection problem is that the reservoir conditions and pore-fluid properties can explicitly be specified that is not straightforward in empirical relations.

As previously mentioned, for a given reservoir rock the pore-filling fluid affects the wave velocities. Gassmann theory describes the effects of uniform saturation on velocity at low seismic frequencies (Mavko et al., 1996). Gassmann's equations are as follows:

$$\frac{K_{dry}}{K_O - K_{dry}} = \frac{K_{sat}}{K_O - K_{sat}} - \frac{K_{fl}}{\phi(K_O - K_{fl})}, \text{ and} \tag{5.1}$$

$$\mu_{dry} = \mu_{sat}, \tag{5.2}$$

where K_{dry} represents the dry rock bulk modulus, and μ_{dry} represents the dry rock shear modulus. K_O stands for the mineral modulus, K_{sat} is the water-saturated rock bulk modulus, and μ_{sat} is the water-saturated rock shear modulus. K_{fl} is the bulk modulus of the pore fluid and ϕ is the porosity. Figure 4.5 shows a cross-plot of Vp versus Vs for core data from LCI at the in-situ effective pressure. The measurements were conducted on room-dry samples and Gassmann's equation was used to calculate the velocities for brine-, oil-, and gas-saturated rocks. Again, the model line separates the rocks with brine from those with hydrocarbons.

4.4 Hydrocarbon Identification and Reservoir Monitoring

La Cira well 1882 was completed in Zone C with open-hole well log measurements, including monopole sonic, collected in 1988. Seven years later, Zone C in this well was

closed, and new cased-hole monopole and dipole sonic logs were recorded (Figure 4.6). A new interval (La Cira Sands) above Zone C was open for production.

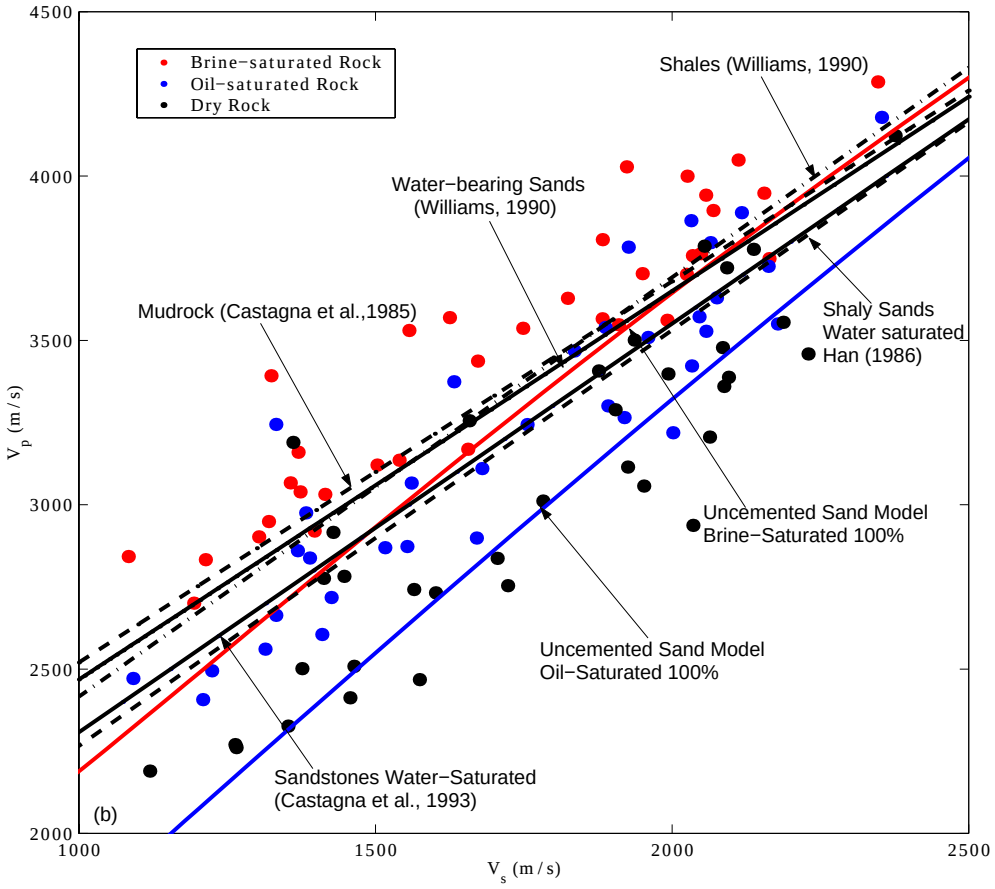

Figure 4.5: Vp versus Vs for core data. The theoretical and empirical model lines are superimposed on the plots.

Figure 4.7 is a plot of the shale content, the Vp/Vs ratio, and Vp versus depth for Zone C sands from the early (1988) and recent (1995) measurements. Superimposed on the Vp/Vs track are two model curves, one for 100% water and the other for 100% oil saturation. The intervals where the data Vp/Vs curve falls between the two model curves correspond to the completed hydrocarbon-bearing intervals from which oil was produced between 1988 and 1995. In this context, the model can be used for hydrocarbon identification.

In the Vp track, a drop in the velocity is observed between the years 1988 and 1995. The observed difference, and, in general, small velocity values, also tie in well with the

intervals open for production. The observed large Vp decrease in some intervals is most likely due to the addition of free gas to the original fluid system as the reservoir pressure falls below the bubble point. Notice that the intervals with free gas correspond to those where the 1995 Vp/Vs data fall below the 100% oil saturation curve.

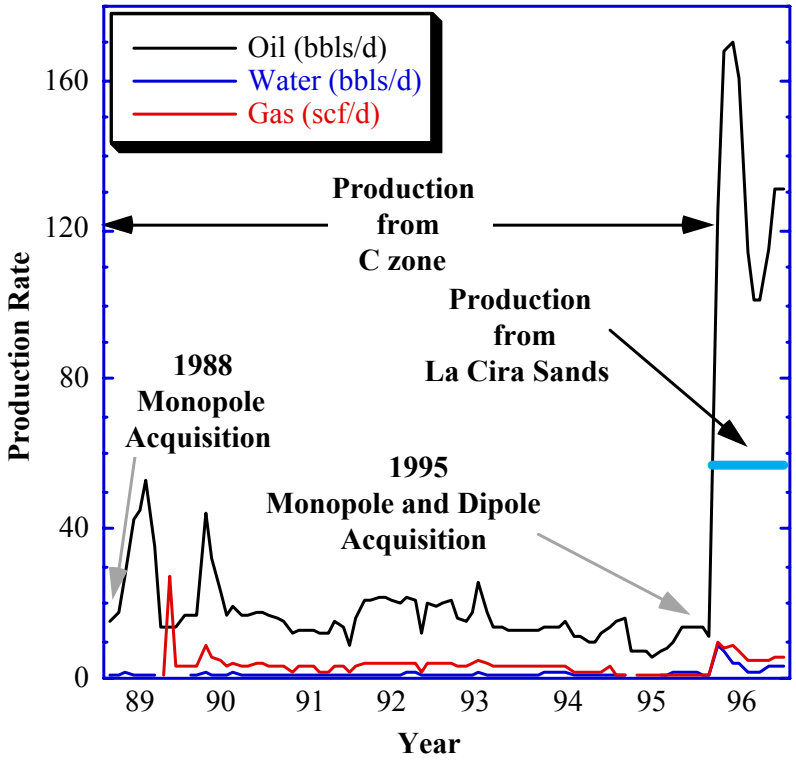

Figure 4.6: Production rate versus time for well LC-1882. Large increase in production in 1995 is due to the opening of the La Cira Sands interval.

The same hydrocarbon indicator technique is applied to the La Cira Sands interval that was *closed to production* (Figure 4.8). As expected, the repeated Vp data show no temporal changes. At the same time, the Vp/Vs ratio clearly delineates (by falling between the two model lines) the intervals that were chosen for completion independently, based on the open-hole resistivity data (see water saturation in the first frame of Figure 4.8). The large production rate increase shown in Figure 4.6 after 1995 is due to production from these intervals.

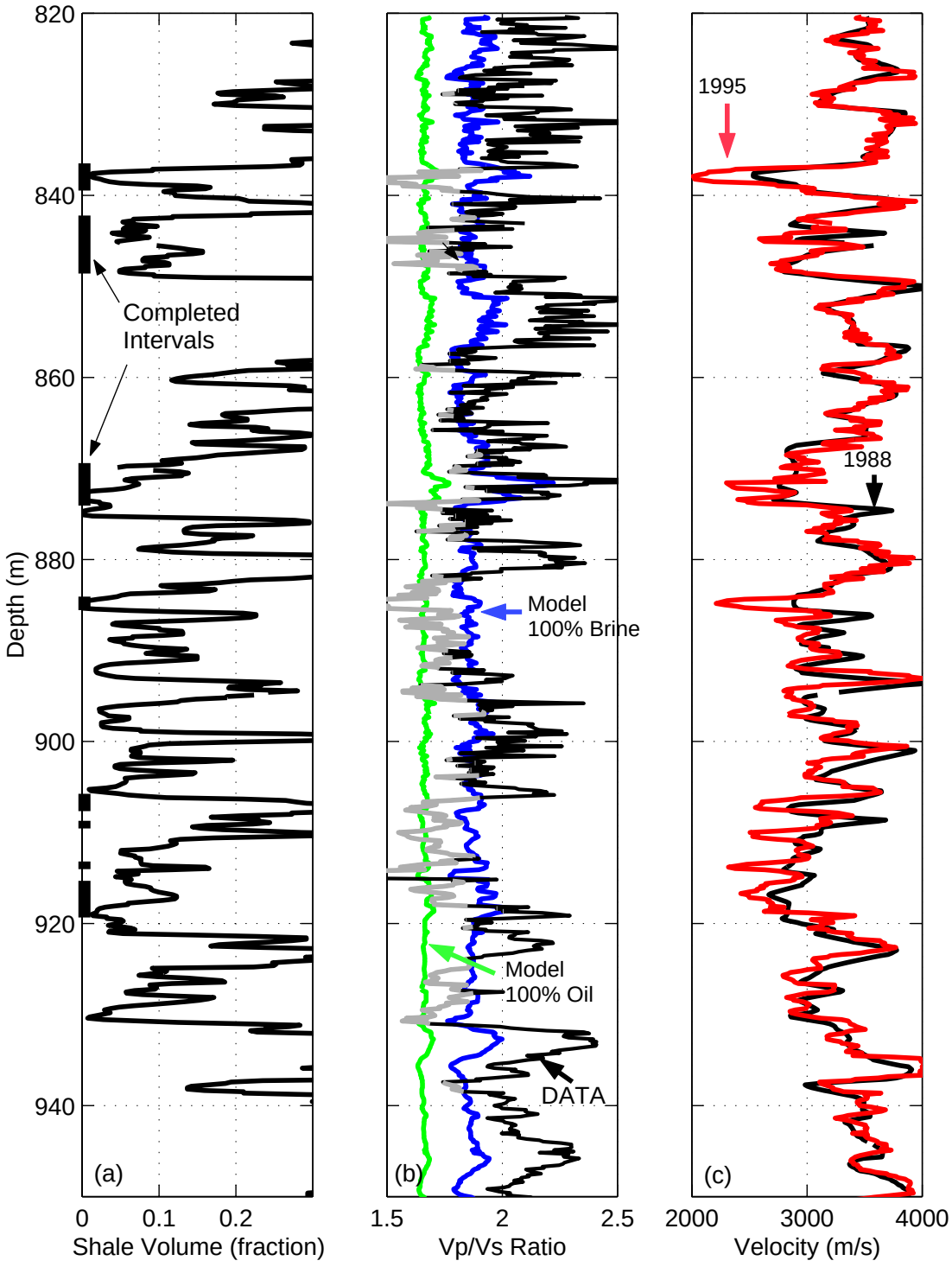

Figure 4.7: Well LC-1882, Zone C. Interval opens to production. (a) Shale volume versus depth with bars indicating open intervals. (b) Vp/Vs ratio versus depth. The green and blue curves are model curves for 100% oil and 100% brine saturation, respectively. The black curve is from 1995 data. The part of the data curve that falls below the 100% water saturation curve is shown in gray. (c) Vp versus depth. The black and the red curves are for the 1988 and 1995 data, respectively.

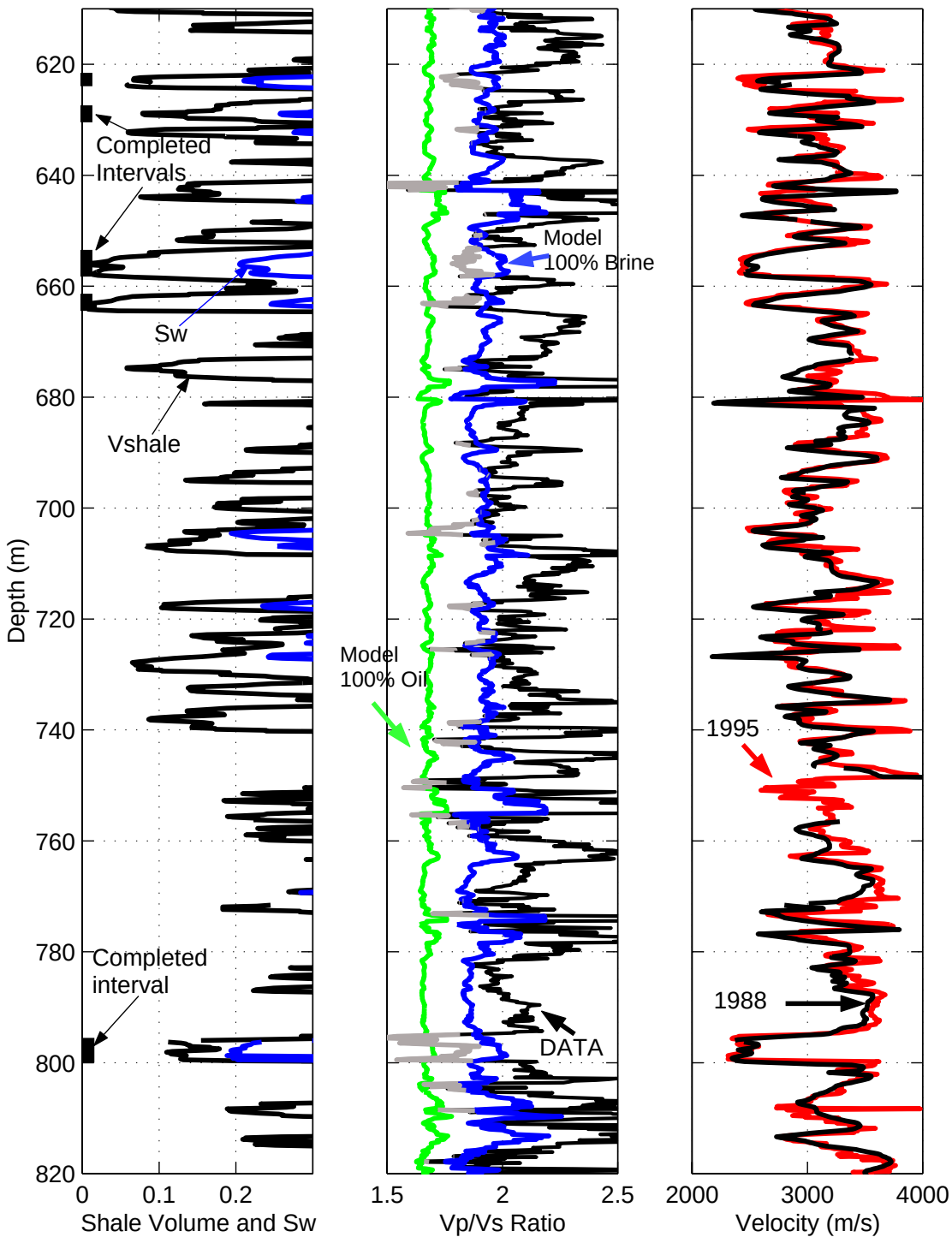

Figure 4.8: Well LC-1882, La Cira Sands. Interval closed to production. Same as Figure 4.7 with water saturation curve added to the shale content track.

4.5 Conclusions

The results show that first-principle-based theoretical rock physics modeling can be used to interpret P- and S-wave well log data for hydrocarbon detection behind the casing in fluvial Tertiary sands. The same rock physics approach should be valid for identifying hydrocarbons in LCI and other fields with similar geologic setting from surface seismic if pre-stack or offset-stack data are available. The rock physics interpretation of dipole sonic logs appears to be a promising methodology for the detection of bypassed and untapped oil, and pay intervals behind the casing in mature fields such as LCI.

Well log data also show that a noticeable change in Vp can be expected in produced intervals. Such changes, combined with rock physics interpretation can be a basis for seismic reservoir monitoring.

4.6 Acknowledgments

I thank ECOPETROL and Stanford Rock Physics Project for providing data and financial support for this study. Additional thanks go to Professor Amos Nur and Dr. Jack Dvorkin for useful discussions. I would like to thanks Dr. Dan Moos for his comments about the application of the Williams' method. This study has been also supported by the Department of Energy (Grants # DE-FG03-98ER14904 and DE-FG03-86ER13601).

4.7 References

Batzle, M. L., and Z. Wang, 1992, Seismic properties of pore fluids: Geophysics, **57,** no. 11, p. 1396-1408.

Bettis, F., C. Borden, W. Rowe, B. Schawanitz, 1987, Sonic logging in cased wells: Opportunities for enhancing oil fields: Schulumberger Technical Review, December, p. 14-18.

Brie, A., F. Pampuri, A. Marsala, and O. Meazza, 1995, Shear sonic interpretation in gas-bearing sands: Annual technical conference and exhibition proceedings, Formation evaluation and reservoir geology, Society of Petroleum Engineers, SPE 30595, p. 701-710.

Cigni, M., and M. Magrassi, 1990, Radioactive and sonic measures recorded in a cased hole; how to use them to quantitatively evaluate the remaining hydrocarbon saturation: The Log Analyst, **31,** no. 5, p. 319-320.

Castagna, J. P., M. L. Batzle, and T. K. Kan, 1993, Rock physics, The link between rock properties and AVO response, in J. P. Castagna and M. Backus, Eds, Offset dependent reflectivity, Theory and practice of AVO analysis, Society of Exploration Geophysicists, Investigations in Geophysics, no. 8, Tulsa, Oklahoma, 3-36.

Castagna, J. P., M. L. Batzle, and R. L. Eastwood, 1985, Relationships between compressional-wave and shear wave velocities in clastic silicate rocks: Geophysics, **50,** p. 571-581.

Chen, S., and E. Eriksen, 1991, Compressional and shear-wave logging in open and cased holes using a multipole tool: Geophysics, **56,** p. 550-557

Dickey, P. 1992, La Cira-Infantas Field, Middle Magdalena Basin, in E. A. Beaumont and N. H. Foster, Eds. Structural Traps VII, AAPG Treatise of Petroleum Geology, Atlas for Oil and Gas Field, p. 323-347.

Eastwood, R., and J. Castagna, 1987, Interpretation of V (p) /V (s) ratios from sonic logs, in Danbom, S. H., ed., Shear-wave exploration, Tulsa, OK, Society of Exploration Geophysicists, Geophysical Developments, **1,** p. 139-153.

Felder R., 1988, Cased-hole logging for evaluating bypassed reserves: Journal of Petroleum Technology, August, p. 969-973.

Georgi, D., R. Heavysege, S. Chen, and E. Eriksen, 1991, Application of shear and compressional transit-time data to cased-hole carbonate reservoir evaluation: The Log Analyst, **32**, p. 129-143.

Gournay, L., 1982, Detection of bypassed gas using borehole gravimeter and pulsed neutron capture logs: The Log Analyst, **23**, no. 3, p. 27-32.

Han, D., 1986, Effects of porosity and clay content on acoustic properties of sandstones and unconsolidated sediments, Ph. D. thesis, Stanford University.

Harrison, A., C. Randall, J. Aron, C. Morris, A. Wignall, R. Dworak, L. Rutledge, and J. Perkins, 1990, Acquisition and analysis of sonic waveforms from a borehole monolope and dipole source for the determination of compressional and shear speeds and their relation to rock mechanical properties and surface seismic data: 65th Annual

technical conference and exhibition of the Society of Petroleum Engineers, New Orleans, LA, September 23-26, SPE 20557, 16 p.

Hornby, B., W. Murphy III, H. Liu, and K. Hsu, 1992, A North Sea case study: Geophysics, **57,** no. 1, p. 146-160.

Kessler, C., and L. Sanders, 1989, Cased-hole hydrocarbon detection in the Permian Basin using the full- wave sonic tool, 64rd Annual technical conference and exhibition of the Society of Petroleum Engineers, San Antonio, TX, Oct. 8-11, SPE 19610, 13 p.

King, R. L. and R. Bradley, 1977, Gamma-ray log finds bypassed oil zones in six Texas Fields: Oil and Gas Journal, **75,** no. 14; p. 92-99.

Krief, M., J. Garat, J. Stellingwerff, and J. Ventre, 1990, A petrophysical interpretation using the velocities of P and S waves (full-waveform sonic): The Log Analyst, **31**, no. 5, p. 355-369.

Laverde, F., 1996, Estratigrafia de alta resolucion de la seccion corazonada en el campo La Cira, Ecopetrol, Technical report, 37 p.

Mavko G., T. Mukerji and J. Dvorkin, 1998, The rock physics handbook, tools for seismic analysis in porous media: Cambrige, Cambrige University Press, 329 p.

Mesa, A., 1995, Diagenesis y calidad del reservorio del campo La Cira, Ecopetrol, technical report, 44 p.

Moos, D., C. Phillips, A. Hooks, K. Tagbor, and D. Clarke, 1995a, Direct detection of hydrocarbons by acoustic logging in the Wilmington Field, CA.: AAPG Pacific section meeting, abstracts, AAPG Bulletin; **79,** no. 4, p. 594.

Moos, D., S. Hara, C. Phillips, A. Hooks, and K. Tagbor, 1995b, Field test of acoustic logs for measuring porosity and oil saturation in a mature waterflood in the Wilmington field, CA: SPE Western regional meeting, Bakerfield, CA, March 8-10, SPE 29655, 14 p.

Moos, D., and J. Dvorkin, 1996, Sonic logging through casing for porosity and fluid characterization in the Wilmington Field, CA: SEG Annual Meeting Expanded Technical Program Abstracts with Biographies, **66,** p. 134-137.

Moos, D., 1997, Fluid detection and porosity determination using acoustic logs in the Wilmington Field, CA: Annual Meeting Abstracts - American Association of

Petroleum Geologists and Society of Economic Paleontologists and Mineralogists, Vol. **6,** p. 84-85.

Moos, D., and S. Walker, 1997, Hydrocarbon detection behind casing in the Wilmington Field, CA: AAPG Pacific Section meeting, abstracts, Tulsa, OK, American Association of Petroleum Geologists, April 1997, AAPG Bulletin, **81,** no. 4, p. 690.

Morales, L. G., D. J. Podesta, W. C. Hatfield, H.Tanner, S. H. Jones, M. H. Barker, D. J. O'Donoghue, C. E. Mohler, E. P. Dubois, C. Jacobs, and C. R. Goss, 1958, General geology and oil occurrences of the Middle Magdalena Valley, Colombia: Habitat of Oil Symposium, American Association of Petroleum Geologists, p. 641-695.

Nieto, J., and D. Cowper, 1991, Shear-wave acoustic logging–Applications and examples: The Log Analyst, **32,** no. 4, p. 158.

Nur, A., and Z. Wang, 1988, Seismic and acoustic velocities in reservoir rocks, volume 1, experimental studies: Society of Exploration Geophysicists, geophysics reprint series no. 10, 405 p.

Paillet, F., and C. Cheng, 1991, Acoustic waves in boreholes: CRC press, Boca Raton, Fl., 264 p.

Paillet, F., C. Cheng, and W. Pennington, 1992, Acoustic waveform logging: advances in theory and application: Log Analyst, **33**, no. 3, p. 239-258.

Rasmussen, N. F., 1975, Borehole gravimeter finds bypassed oil: Oil and Gas Journal, Vol. **73**, No. 39, p. 100-104.

Sanders, L., 1993, Hydrocarbon detection using the shear wave travel time and neutron porosity in sandstone reservoirs: Society of Professional Well Log Analysts, 34th Annual Logging Symposium, Paper S.

Schiuma, M., M. Claverie, and A. Brie, 1997, Hydrocarbon identification from shear sonic logs in the Neuquen Basin, Argentina: Society of Professional Well Log Analysts, transactions of the SPWLA Annual Logging Symposium, Houston, Texas, June 1997, **38.**

Schlumberger, 1990, Shear wave logging with dipoles: Oilfield Review, no. 10, p. 9-12.

Schlumberger, 1992, Taking advantage of shear waves: Oilfield Review, no. 3, p. 52-54.

Schlumberger, 1995, DSI, Dipole Shear Sonic Imager: Schlumberger Wireline and Testing, Sugar Land, Texas, Document SMP-9200, 36 p.

Selley, R. C., 1996, Ancient sedimentary environments and their sub-surface diagnosis: London, Chapman & Hall, 300 p.

Smolen, J. J. 1987, Cased-hole logging: A perspective: The Log Analyst, **28**, no. 2; p. 165-174.

Smolen, J. J., 1996, Cased hole and production log evaluation, Pennwell Books, Tulsa, OK, p. 125-139.

Taborda, B., 1965, The geology of the De Mares Concession: Geological field trips, Colombia, 1958-1978, Colombian Society of Petroleum Geologists and Geophysicists, p. 119-159.

Tubman, K., C. Chang, and N. Toksoz, 1984, Determination of formation properties in cased boreholes using full waveform acoustic logs: Society of Professional Well Log Analysts, transactions of the SPWLA Twenty-fifth Annual Logging Symposium, June 10-13.

Walker, S., 1997, Locating and producing bypassed oil: A D.O.E. project updated, SPE regional meeting, Long Beach, California, June 25-27, SPE 38283, 13 p.

Westaway, P., M. Wittmann, and P. Rochette, 1981, Application of nuclear techniques to reservoir monitoring: Journal of Petroleum Technology, January, p. 46-54.

Williams, D. M., 1990, the acoustic log hydrocarbon indicator: Society of Professional Well Log Analysts, 31 Annual Logging Symposium, Paper W.

Yan, S., G. Chang, Y. Zhang, W. Qiao, and G. Du, 1995, The application of acoustic full waveform logging in petroleum engineering: International Meeting On Petroleum Engineering, Beijing, PR China, November 14-17, SPE 29984, 11 p.